UNIVERSITÀ DEGLI STUDI DI MILANO
FACOLTÀ DI SCIENZE MATEMATICHE, FISICHE E NATURALI
DOTTORATO DI RICERCA IN
FISICA, ASTROFISICA E FISICA APPLICATA

MEASUREMENT OF TOP QUARK PAIR PRODUCTION CROSS SECTION AND CHARGE ASYMMETRY AT THE LHC WITH THE ATLAS EXPERIMENT

Settore Scientifico Disciplinare FIS/01

Coordinatore: Prof. Marco Bersanelli
Tutore: Prof. Francesco Ragusa

Tesi di Dottorato di:
Maria Ilaria Besana
Ciclo XXIV

Anno Accademico 2010-2011

Contents

Introduction

In March 2010 the Large Hadron Collider (LHC) at CERN started its operation at a centre of mass energy of 7 TeV. Since then, the ATLAS experiment has been collecting a large number of proton-proton collision events, resulting in an integrated luminosity of about 5.2 fb^{-1} up to now.

My PhD research has been focused on top quark physics, which is one of the milestones of the ATLAS experiment physics program. The production of top quarks is the dominant high-p_{T} process in p-p collisions at multi-TeV energies, after QCD jets, W and Z bosons. Furthermore, top quark physics is a rich subject, in fact top quark events are used for detector commissioning and to provide a consistency test of the Standard Model. Finally the top quark sector is considered a good channel for new physics discovery. In some Beyond the Standard Model theories top quark pairs can be produced by the exchange of undiscovered heavy particles. There are also several models that predict the existence of heavy coloured resonances decaying into top quarks in the TeV energy range.

In particular I have performed consistency tests of Standard Model theory using two top quark physics measurements. With first data I have focused on the measurement of top quark pair cross section and then I have moved to more stringent tests using the measurement of top quark charge asymmetry.

The first part of my PhD activity has been dedicated to the top quark pair production cross section determination with a counting method. The aim of this analysis has been to provide the first measurement of top quark pair production cross section in p-p collisions at $\sqrt{s} = 7$ TeV in order to compare it with theoretical Standard Model predictions. This result has been published in Autumn 2010, as the best world measurement at that time in $\sqrt{s} = 7$ TeV proton-proton collisions.

This analysis has been performed in the so called "semileptonic channel". This decay channel, with one W boson decaying leptonically and the other one decaying hadronically, is characterized by the presence of one energetic electron or muon (events with a τ-lepton have not been considered, since they need a dedicated analysis), one neutrino and at least four energetic jets. Two of these jets come from a b-quark and they can be identified using b-tagging techniques. The neutrino doesn't interact in the detector, but its energy can be measured in the transverse plane as missing transverse energy. The most important background processes are QCD multijet events and W+jets events, in which W boson is produced in association with hadronic jets. As a first step, top quark pair candidate events have been selected:

an optimization of selection cuts has been done in order to select a signal sample as pure as possible. Another crucial point has been the evaluation of the background contamination. Since LHC collisions energy is $\simeq 4$ times higher than the one of previous existing colliders, Monte Carlo predictions are characterized by large uncertainties. For what concerns the two main backgrounds, data driven techniques have been therefore designed in order to obtain an estimate directly from data, as independent as possible from Monte Carlo predictions. The systematic uncertainty coming from the selection and the background estimate has been evaluated. The cross section measured with 35 pb^{-1} in the electron and muon channels combined is $\sigma_{t\bar{t}} = 154^{+49}_{-45}$ pb for a selection which does not make use of b-tagging information, and 156^{+36}_{-30} pb after requiring at least one b-tagged jet. Within their uncertainty, the two results are well compatible between each other and with Standard Model prediction.

With the increase of available statistics and a better knowledge of the detector performance, the measurement of top quark pair cross section with a counting method became less competitive with respect to fit techniques. In addition the collection of higher statistics permitted to obtain competitive results on the measurement of other top quark properties, which were suffering for higher statistical uncertainty. In the second part of my PhD activity I have therefore performed studies for top quark charge asymmetry measurement. This analysis has been performed in the same channel of cross section measurement. This choice has permitted to take advantage of all the previous studies on signal selection, on background estimates and on systematic uncertainty evaluation.

Top quark charge asymmetry can only occur in asymmetric initial states in top quark pair production, so the main contribution comes from $q\bar{q}$ production mechanism. It consists in the fact that the top quark is preferably emitted in the direction of the incoming quark and not in the one of the incoming antiquark. This feature originates a difference in top and antitop quark rapidity distributions. The asymmetry foreseen at the LHC according to the Standard Model is small, as will be shown in the following. Some Beyond the Standard Model theories predict, at the opposite, a sizable asymmetry. As a consequence, this measurement can provide a window on new physics. Furthermore the CDF Collaboration measurement, performed at the Tevatron collider at Fermilab, has shown a deviation larger than 3 σ from the Standard Model prediction in the large $t\bar{t}$ invariant mass region.

This analysis has been performed with 0.70 fb^{-1}. With respect to previous cross section analysis, additional investigations have been done on background contamination, since this measurement is sensible not only to the normalisation, but also to the shape of background processes. Furthermore dedicated studies have been done in order to design algorithms to reconstruct top and antitop quarks from their decay products. Finally some work has been done to identify which observables are more sensitive to new physics and their dependence with respect to top quark pair kinematic variables, since different Beyond the Standard Model theories predict different dependencies and different relations between variables.

For the first ATLAS measurement, the observable considered is:

$$A_C(\Delta|y|) = \frac{N(\Delta|y| > 0) - N(\Delta|y| < 0)}{N(\Delta|y| > 0) + N(\Delta|y| < 0)} \tag{1}$$

where $\Delta|y|$ is the difference between the absolute values of top and antitop rapidities ($|y_t| - |y_{\bar{t}}|$), $N(\Delta|y| > 0)$ is the number of selected events in which $\Delta|y|$ is positive, while $N(\Delta|y| < 0)$ is the number of selected events in which $\Delta|y|$ is negative.

The measured asymmetry is $A_C = -0.024 \pm 0.016\,(\text{stat.}) \pm 0.023\,(\text{syst.})$, combining electron and muon channel. Within present uncertainty the result is in agreement with the Standard Model prediction (from the MC@NLO Monte Carlo generator) of $A_C = 0.006$.

Work is ongoing in order to reduce the systematic uncertainty. With higher integrated luminosity, differential asymmetries will also be considered increasing the sensitivity to new physics.

The first chapter of this thesis is dedicated to a review of top quark physics. After a brief introduction on the Standard Model theory, important measurements performed both at the Tevatron and at the LHC are described. Then the prospects for top quark physics at the LHC are discussed. The second chapter describes the LHC and the ATLAS detector. In particular the reconstruction algorithms for the objects involved in top quark pair events are presented. In the third chapter top quark pair cross section measurement with first 35 pb^{-1} is documented, while the last chapter is dedicated to top quark charge asymmetry analysis performed with 0.70 fb^{-1}.

Chapter 1

Introduction on Top quark physics

The aim of this chapter is to give an introduction to top quark physics.

Top quark physics is presently and will be widely explored at the LHC: after QCD jets, W and Z bosons, the production of top quarks is the dominant high-p_{T} process in p-p collisions at multi-TeV energies. The LHC can be considered a top quark factory: the top quark pair production cross section is indeed enhanced by a factor 20 with respect to the Tevatron even at 7 TeV centre-of-mass energy.

Top quark physics is a rich subject. Top quark events are very useful for detector commissioning and, moreover, they can provide a consistency test of the actual particle physics theory, the Standard Model (SM), as it has been done in the measurements presented in this thesis. Furthermore, the precise measurement of some quantities, such as top quark charge asymmetry, can be a window on new physics as explained in Section 1.4.2. Top quark events are finally an important background for many processes predicted by new physics models.

This chapter is organized as follows. First of all a brief description of the SM is given. After that, the top quark is introduced in more detail in Section 1.2. Top quark production and decay modes at the Tevatron and at the LHC are then discussed in Section 1.3. Finally the measurements of top quark pair production cross section and charge asymmetry are discussed (see Section 1.4).

1.1 Brief introduction to the Standard Model

The SM is a successful theory incorporating the present understanding of fundamental particles and their interactions. In the SM, two classes of fundamental particles are distinguished according to their spin: fermions with spin 1/2 and vector gauge bosons with spin 1. A scalar boson, the Higgs boson, is also predicted by the theory, but it has not been observed yet.

Two gauge theories describe the interactions: the Electroweak Theory (EW) and the Quantum Chromodynamics (QCD). QCD describes strong interactions and is based on the non-abelian $SU(3)$ group. The EW theory, which includes Quantum Elecrodynamics (QED), describes weak and electromagnetic interactions and is

based on the $SU(2)_L \times U(1)$ group. These forces are mediated by the gauge bosons.

- The electromagnetic interaction affects all particles of non-zero electric charge. Its associated gauge boson is the photon (γ), while the associated charge is the electric charge. The coupling constant is the fine structure constant, given by

$$\alpha_{em}(m_e) = \frac{e^2}{4\pi\epsilon_0\hbar c} = 7.2973525376(50) \times 10^{-3} \tag{1.1}$$

  where e is the absolute value of the electron charge, ϵ_0 is the dielectric constant of the vacuum, $\hbar$ is the Planck constant and c is the speed of light in vacuum.

- The weak interaction affects all fundamental fermions and has three associated vector bosons, W^+, W^-, and Z. The associated charge is the weak charge. The coupling constant, called Fermi coupling constant, is

$$\frac{G_F}{(\hbar c)^3} = 1.16637(1) \times 10^{-5} GeV^{-2} \tag{1.2}$$

  where $\hbar$ is the Planck constant and c is the speed of light in vacuum.

- The strong interaction is carried by eight gluons (g) and the associated charge is called colour. QCD is a non-abelian gauge theory, described by a three dimensional gauge symmetry in which the generators do not commute. This difference between QED and QCD manifests itself in the fact that photons don't carry electromagnetic charge, while gluons are coloured particles. Photons, as a consequence, don't interact with each other, whereas gluons do. At first order in perturbation theory the QCD coupling constant takes the form

$$\alpha_s(\mu^2) = \frac{12\pi}{(33 - 2n_f)\ln\left(\frac{\mu^2}{\Lambda^2_{QCD}}\right)} \tag{1.3}$$

  where n_f is the number of generations, μ is the scale of the interaction (usually the squared transferred four-momentum is taken), and Λ_{QCD} is an energy scale parameter, that is measured by experiments to be $\Lambda_{QCD} \sim 250$ MeV. This value corresponds roughly to the scale of the nucleon radius. The strong coupling increases with distances: $\alpha_s \to \infty$ for $Q^2 \to \Lambda^2_{QCD}$, while $\alpha_s \to 0$ for $Q^2 \to \infty$. In this limit the coupling constant becomes zero and the region of so-called "asymptotic freedom" is reached. The closer one comes to this region, the better one can use perturbative techniques, like for instance in the calculation of cross sections.

The properties of the vector bosons are summarised in Table 1.1.

The fermions have spin 1/2 and are the matter constituents. They are grouped further into isospin doublets of leptons and quarks, as shown in Table 1.2. While

Interactions	Bosons	Electric charge	Mass (GeV)
Electromagnetic	Photon (γ)	0	0
Weak	$W^{\pm}$	± 1	80.403 ± 0.029
	Z	0	91.1876 ± 0.0021
Strong	Gluons (g)	0	0

Table 1.1: Gauge bosons in SM.

leptons are subject only to weak and electromagnetic interactions, quarks have colour charge and so they interact also through the strong interaction.

Both lepton and quark doublets exist in three generations with increasing masses. In the lepton family, electron, muon and τ lepton have electric charge -1, while the neutrinos are neutral. The SM assumes that the neutrino masses are 0. In the quark family, the u (up), c (charm) and t (top) quarks have electric charge $+\frac{2}{3}$e, while the d (down), s (strange) and b (bottom) quarks have charge $-\frac{1}{3}$e.

Because the strong interaction coupling constant increases with distance between coloured particles (see Equation 1.3), quarks can not be found isolated, but only bounded in colourless states. Since the existence of states with more than three quarks is generally not considered to be proven, there are two possible combinations: either a quark is bound with an antiquark forming a meson or three (anti)quarks are forming a (anti)baryon. These two particle types are grouped under the name hadrons.

As mentioned above, the particles of the first generation are the lightest ones. Except for the neutrinos, the particles of the 2^{nd} and 3^{rd} generations are unstable, thus giving the first generation the privilege to form all ordinary matter.

Fermions	I generation	II generation	III generation	Charge	Interactions
Quarks	u	c	t	$+\frac{2}{3}$	Strong + Weak + EM
	d	s	b	$-\frac{1}{3}$	Strong + Weak + EM
Leptons	ν_e	ν_μ	ν_τ	0	Weak
	e	μ	τ	-1	Weak + EM

Table 1.2: Elementary fermionic particles in SM.

The SU(2) symmetry has to be broken, since $W^{\pm}$ and Z bosons have a mass different from zero. This is achieved in the SM theory through the Higgs mechanism. A complex scalar field ϕ, called Higgs field, is introduced. This is designed so that the minimum of the scalar potential $V(\phi)$ occurs at a non-zero field value at energy below a certain threshold. If a change of state occurs, causing a transition from high energy density to low energy density (such as in the early universe), the field will spontaneously fall into a minimum of the potential. The choice of

a particular minimum implies a symmetry breaking. The spontaneous symmetry breaking originates the presence of one massive boson, called Higgs boson, which is responsible of the masses of all other SM particles. Masses originate from the interaction with it.

Higgs boson has not been discovered yet and its search is one of the main goals of the LHC collider. Some indirect constraints on its mass have been obtained by the study of loop corrections, as will be explained in Section 1.2. Exclusion limits have been set from direct searches at the LHC and at previous experiments, as reported in Section 2.1.1.

The SM theory has been confirmed by many experimental results and it explains almost all observations in particle physics, but is not a completely satisfactory model. Some facts suggest that SM is only an effective theory at low energies and new physics should emerge at higher scales, requiring a more fundamental description. Some of them are listed in the following. First of all it predicts zero masses for neutrinos, but the measurement of their oscillation has provided a proof that their mass, even if very small, is not zero. Furthermore it has been proved that a large fraction of the Universe is made of an unknown matter, called "Dark Matter" and the SM doesn't provide any candidate for it. It is furthermore characterized by a large number of parameters (19) and some of its characteristics, as for example the number of families, can't be explained. Another critical issue is the hierarchical problem. In the calculation of the Higgs boson mass at NLO loop corrections, involving bosons, fermions and Higgs boson self-interaction, have to be included. If we assume that physics beyond the SM will appear for energies higher than a given threshold $\Lambda_{cut-off}$ (this is needed, because at a certain scale gravity will come into play), contributions $\sim \Lambda^2_{cut-off}$ will be added. The presence of these corrections would imply a huge Higgs boson mass, while indirect constraints prefer values of Higgs masses below 200 GeV. The relatively low mass can be obtained by assuming the presence of a "fine tuning". The different contributions are such as bosons and fermions terms almost cancel each other. This is possible, but quite unnatural and so disfavoured. Furthermore, a unification of EW and QCD theories is aspired by physicists to obtain a Grand Unified Theory (GUT), in which the $SU(3)$, $SU(2)_L$, and $U(1)$ groups have a common origin in a larger symmetry group G. It is expected that at a high energy scale these symmetries are unbroken and that their coupling constants become one. This is not realized in the SM, but only in some theories built as an extension of it. Finally the SM does not include gravity.

An extension of SM seems necessary and so searches of new physics Beyond the Standard Model (BSM) are ongoing at the LHC.

1.2 Top quark expectation before its discovery and observation at Tevatron

1.2.1 Indirect evidence

After the discovery of the b-quark in 1977 [1], several arguments suggested the existence of an isospin partner, the top quark. Some of them are discussed in the following.

First of all, the renormalizability of the SM requires the sum of the charges within a family to be 0 [2]. Given the b-quark and the τ lepton, another component with charge $q_t = 2/3$ was needed, as it is shown below:

$$q_\tau + 3 \cdot q_b + 3 \cdot q_t = -1 + 3 \cdot \left(-\frac{1}{3}\right) + 3 \cdot \left(\frac{2}{3}\right) = 0 \tag{1.4}$$

where q_τ, q_b and q_t are τ-lepton, b-quark and top quark charges respectively; q_b and q_t are multiplied by three, since they occur in three colours.

Another argument was the fact that interactions changing the flavour trough neutral currents (Flavour Changing Neutral Currents, FCNC) are strongly suppressed. The proposed mechanism to explain this observation (GIM mechanism) required that each family had the same isospin structure.

Finally, a proof originated from the measurements of $Z \to b\bar{b}$ rate at the Large Electron Positron collider (LEP) at CERN and at the Stanford Positron Electron Accelerating Ring (SPEAR) at the Stanford Linear Accelerator Center (SLAC) [3]. The measured decay rate of the Z boson into a b-quark pair was much higher than the one predicted for the case of an isospin singlet b-quark. These results were, at opposite, in very good agreement with the SM prediction, including an isospin partner.

1.2.2 Observation at the Tevatron collider

Since 1977, indirect measurements constrained the mass of the top quark. In addition, direct searches for the top quark were done by many experiments, increasing the lower limit on m_t.

In 1995 the top quark has been finally observed at the CDF [4] and D0 [5] experiments at the Tevatron in proton-antiproton collisions at 1.8 TeV centre-of-mass energy.

1.3 Top quark production and decay at Tevatron and at LHC

1.3.1 Top quark production

According to the SM theory, at hadron colliders the top quark can be produced in pairs (top quark pair, $t\bar{t}$) through strong interaction (EW production of $t\bar{t}$ events is negligible) or alone through weak interaction (single top, t).

The high p_{T} interaction between protons can be directly linked to the interaction between partons within them. In hadron-hadron collisions perturbative QCD calculations of the hard scattering process are possible by invoking the Factorization Theorem, that establishes that the physics at high and low energy scales can be separated. Therefore, the top quark production cross section (both single top t and top quark pair $t\bar{t}$ production) in pp collisions can be expressed as:

$$\sigma_{pp\to t\bar{t}(t)} = \sum_{i,j=q\bar{q},g} \int dx_i dx_j f_i(x_i,\mu_i) f_j(x_j,\mu_j)(\hat{\sigma}_{ij\to t\bar{t}(t)}) \tag{1.5}$$

where $f_i(x_i,\mu_i)$ ($f_j(x_j,\mu_j)$) is the Parton Density Function (PDF), that describes the probability density to find a parton i (j) inside the proton carrying the momentum fraction x_i (x_j) and $\hat{\sigma}_{ij\to t\bar{t}(t)}$ describes short distance interaction of the incoming partons. The last term represents the cross section for the hard-scatter process and is calculated in powers of the coupling constant. Both, the PDF and $\hat{\sigma}_{ij\to t\bar{t}(t)}$, depend on two energy scales: the factorization scale μ_f at which the factorization is done and the renormalization μ_r at which the coupling constant is calculated. Usually they are taken to be the same $\mu_f = \mu_r = \mu$.

In the following, some details on hard scattering processes for single top and top quark pair production are given.

Single top production

Single top production can occur in three different modes:

- *s-channel:*
  a W boson is produced by the fusion of a quark-antiquark pair (see Fig. 1.1 (a)) The theoretical prediction for the production cross section at the LHC (Tevatron) is $\sigma_{s-channel} = (4.6 \pm 0.3)$ pb [6] ($\sigma_{s-channel} = (1.04 \pm 0.04)$ pb [7]);

- *t-channel:*
  a virtual W boson converts a b-quark into a top quark (see Fig. 1.1 (b) and (c)). This is the dominant process at the Tevatron and the LHC. The theoretical prediction for the production cross section at the LHC (Tevatron) is $\sigma_{t-channel} = 64.6^{+3.3}_{-2.6}$ pb [8]($\sigma_{t-channel} = (2.26 \pm 0.12)$ pb [7]);

- *Wt-channel:*
  the top quark is produced in association with a real W boson (see Fig. 1.1 (d) and (e)). This process is negligible at the Tevatron. However, at the LHC this process exceeds the s-channel. The theoretical prediction for the production cross section at the LHC is $\sigma_{Wt-channel} = (15.7 \pm 1.4)$ pb [9].

An asymmetry in top quark and antitop quark production occurs in t and s channels at the LHC. Because colliding particles are two protons, valence quarks are mostly positively charged (uud for the proton) and so top quark to antitop quark production ratio is 1.6 for these two channels.

Top quark pair production

Top quark pairs can be produced through the annihilation of a quark and an antiquark ($q\bar{q}$ annihilation) or through the fusion of two gluons (gg fusion). Due to the different initial states and centre-of-mass energies, the production of $t\bar{t}$ at the LHC is mainly ($\sim 80\%$ at $\sqrt{s} = 7$ TeV) mediated via gg fusion, while at the Tevatron is dominated ($\sim 85\%$) by $q\bar{q}$ annihilation.

QCD predictions for top quark pair production cross section are $(7.46^{+0.48}_{-0.67})$ pb at the Tevatron (1.96 TeV) and $(164.6^{+11.4}_{-15.7})$ pb at the LHC [10].

The possible LO Feynman diagrams for the short distance production processes are shown in Figure 1.2 for both $q\bar{q}$ annihilation and gg fusion.

1.3.2 Top quark decay modes

The top quark decays via the weak interaction almost always into a b-quark and a W boson, since

$$\frac{BR(t \to Wb)}{BR(t \to Wq)} = \frac{|V_{tb}|^2}{(\sum_q |V_{tq}|^2)} = |V_{tb}|^2 \simeq 1 \tag{1.6}$$

with $q = b, s, d$. V_{ti} is the CKM matrix[1] element for the decay of t quark into a quark of type i. Due to this strong CKM-suppression only the dominant channel $t \to Wb$ is considered for further discussions.

The W boson can decay hadronically into quark pairs of the first two families or leptonically into a lepton and a neutrino:

$$W^+ \to q\bar{q'} \qquad \text{or} \qquad W^+ \to l^+\nu_l \quad \text{with } l = e, \mu, \tau. \tag{1.7}$$

The relative contribution of the hadronic decay is $\frac{2}{3}$. The leptonic branching ratio (BR) is $\frac{1}{3}$, with each of the three family contributing with $\frac{1}{9}$.

Three different decay channels of top quark pairs are distinguished depending on the W boson decay mode:

[1] The Cabibbo-Kobayashi-Maskawa (CKM) matrix is a unitary matrix that contains information on the strength of flavour changing weak decays. The elements of this matrix, V_{ij}, are free parameters of the SM and have to be determined experimentally.

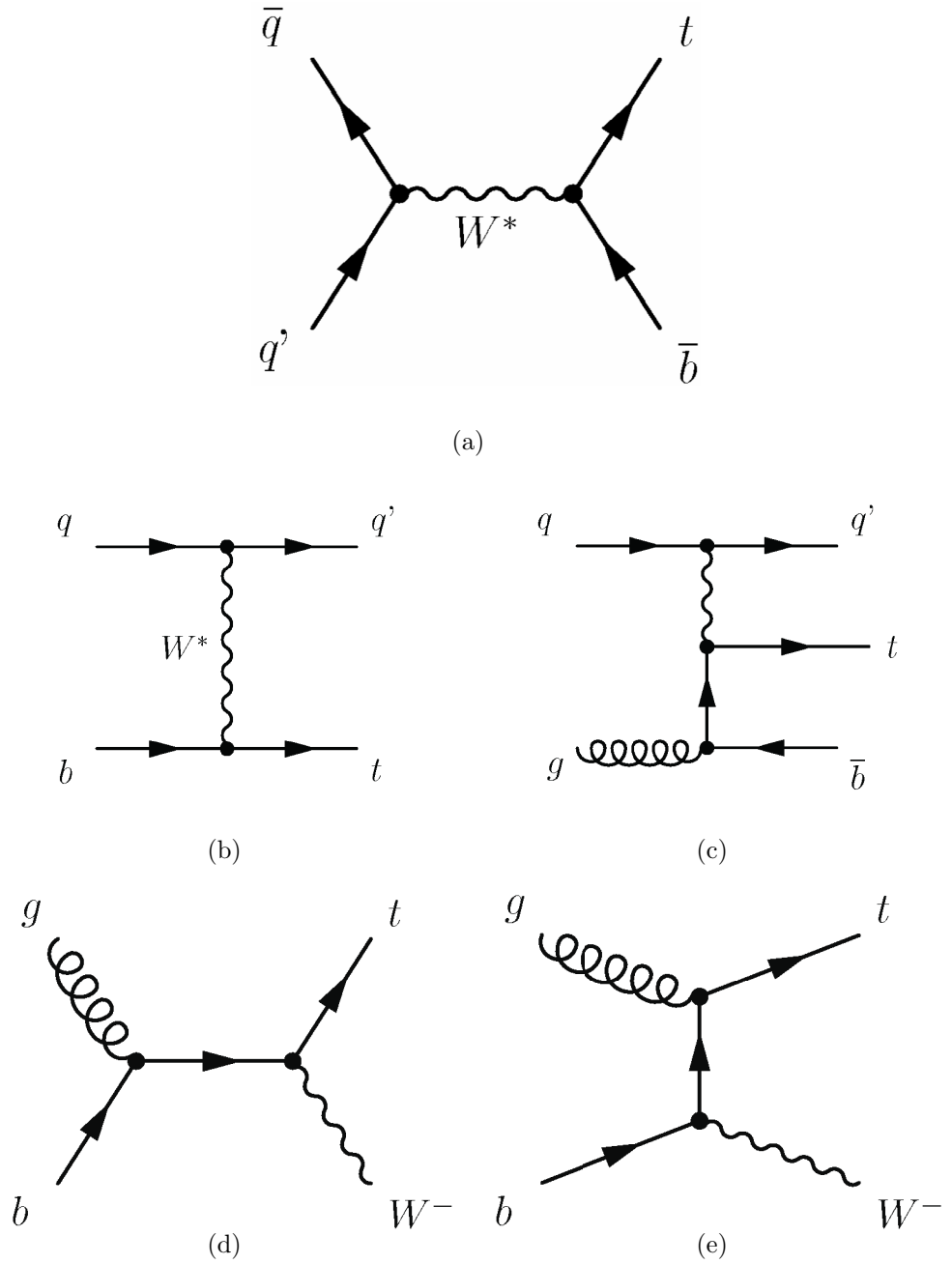

Figure 1.1: *Single top production diagrams at LO for s-channel (a), t-channel (b,c) and Wt channel (d,e).*

- *Di-leptonic channel*
  Both W bosons decay leptonically: $t\bar{t} \to \bar{l}\nu_l b l'\bar{\nu_{l'}}\bar{b}$. The relative contribution is $\sim 10\%$ [11].

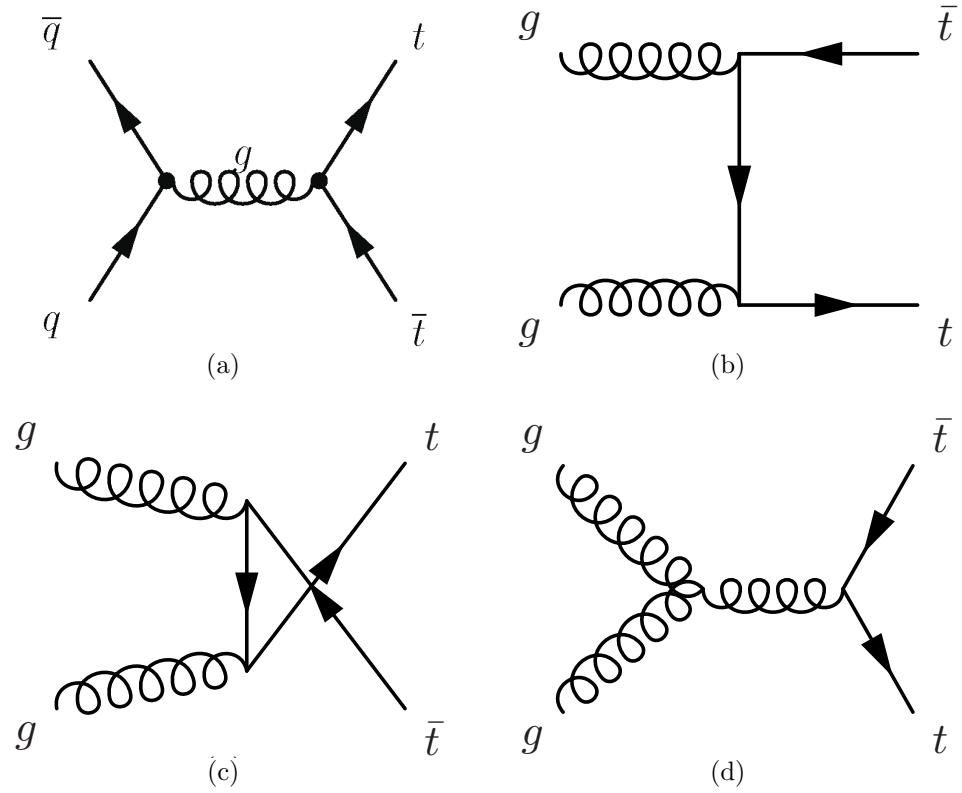

Figure 1.2: *$t\bar{t}$ production diagrams at LO: $q\bar{q}$ annihilation (a) and gg fusion (b,c,d).*

- *Semi-leptonic channel:*
  One W boson decays leptonically and the other one hadronically: $t\bar{t} \to \bar{l}\nu_l bq\bar{q'}\bar{b}$. The relative contribution is $\sim 45\%$ [11].

- *Fully hadronic channel:*
  Both W bosons decay hadronically: $t\bar{t} \to q\bar{q'}bq''\bar{q'''}\bar{b}$. The relative contribution is $\sim 45\%$ [11].

The relative contribution of the different decay modes is summarized in Figure 1.3, while Figure 1.4 shows a complete LO Feynman diagram for top quark pair production via gg fusion and its further decay into the semileptonic channel.

Within semileptonic final states two categories can be identified. The first one is characterized by the presence of an electron or a muon, that can come directly from W boson or, less frequently, from the leptonic decay of a τ lepton, coming from the W boson. The second one is includes events in which the W boson decays into a τ lepton decaying into hadrons. Events with an hadronic decaying τ lepton need very different selection cuts and so a dedicated analysis is required for this channel. Usually the notation semileptonic channel or lepton+jets channel refers to the first category only. The corresponding BR is 34.3%. The same separation

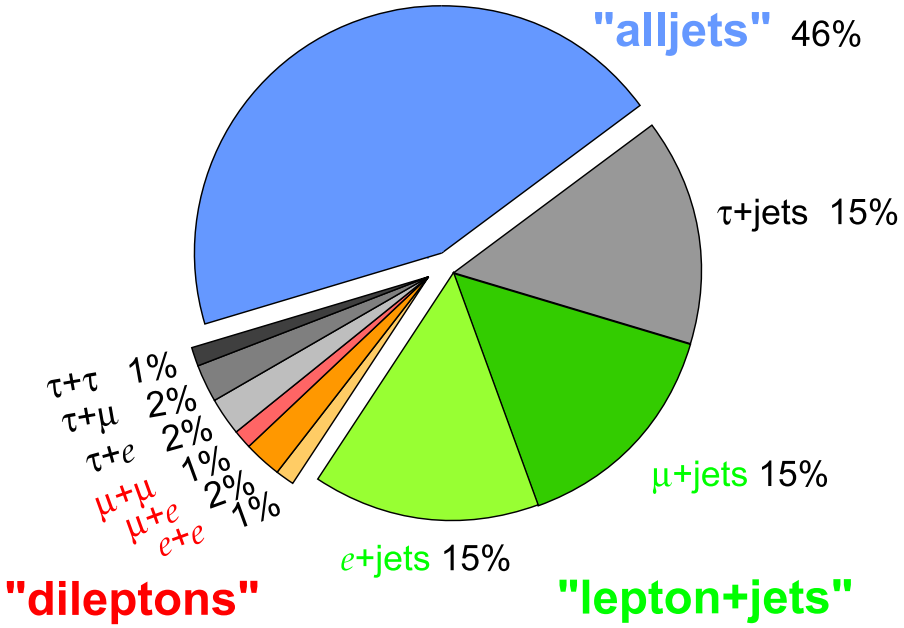

Figure 1.3: *Schematic representation of the relative contribution of the different $t\bar{t}$ decay channels.*

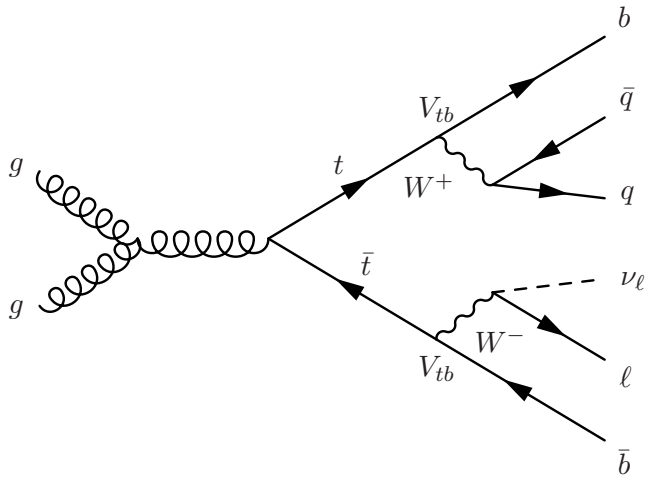

Figure 1.4: *The Feynman diagram for the top quark production via gg-fusion and the further decay in the semi-leptonic channel.*

is considered for di-leptonic final states. The di-leptonic channel usually refers to events with electrons or muons. Events including a τ lepton decaying hadronically are considered separately.

The two analysis presented in this thesis have been performed selecting lepton+jets events. This channel is indeed characterized by a good BR and a clear

signature: the presence of one lepton, one neutrino and two jets originating from a b-quark (b-jets) helps in separating this kind of events from the overwhelming QCD multijet background. Further details on the signature and the main backgrounds are discussed at the beginning of Chapter 3.

1.4 Top quark pair production cross section and charge asymmetry

This section is dedicated to a short review of the most recent results from the Tevatron and the LHC experiments. For what concerns the top quark charge asymmetry, more details are given and a brief theoretical introduction is reported. This measurement is more peculiar with respect to the cross section one and it needs more explanations.

1.4.1 Top quark pair production cross section

The measurement of the top quark pair production cross section ($\sigma_{t\bar{t}}$) is interesting for many reasons. First of all it can provide a test of QCD theoretical predictions, which now have an uncertainty of 10% [12]. Furthermore, it serves as a probe for possible new physics [13], which can manifest as an enhancement, or even deficit, in the rate of top quark pair production. Some new models predict new mechanisms of top quark production and new particles that can decay into top quark pairs. Measurements of the $t\bar{t}$ cross section serve as tests of these possible new physics processes and can place strong constraints on these models. Top quark events are finally an important background to new physics predicted processes, as for example Supersymmetry signatures. For this kind of searches it is fundamental to know top quark pair production cross section with precision.

Inclusive top quark pair cross section has been measured, first of all, in proton-antiproton collisions at a center-of-mass energy of 1.8 and 1.96 TeV by CDF and D0 collaborations. Both experiments have performed the analysis in many channels: lepton+jets, dilepton, all hadronic, τ+jets and τ+lepton. The best measurements come for both experiments from lepton+jets channel at 1.96 TeV and are briefly described below.

The CDF most recent result has been obtained using 4.6 fb^{-1} of data and employing two different techniques [14]. The first one is based on the capability of identifying jets originated from a b-quark (b-tagging technique in the following), while the second one doesn't use b-tagging information, but discriminates $t\bar{t}$ events from background by exploiting differences in their kinematics (kinematic technique in the following). In order to reduce the systematics coming from luminosity determination, $t\bar{t}$ cross section has been evaluated with respect to the Z/γ^* production one and then multiplied by the SM theoretical expectation for σ_{Z/γ^*}. This replaces a 6% uncertainty from the measured luminosity with a 2% uncertainty from the

theoretical Z/γ^* cross section. The final results are reported below, assuming a top mass of 172.5 GeV:

$$\sigma_{t\bar{t}} = 7.32 \pm 0.36(\text{stat.}) \pm 0.59(\text{syst.}) \pm 0.14(\text{theory}) \text{ pb} \quad b\text{-tagging techn.}, \quad (1.8)$$

$$\sigma_{t\bar{t}} = 7.82 \pm 0.38(\text{stat.}) \pm 0.37(\text{syst.}) \pm 0.15(\text{theory}) \text{ pb} \quad \text{kinematic techn.} \quad (1.9)$$

The results are limited by systematics; the main contributions come from the uncertainty on the energy scale of jets (JES), background contamination and b-tagging identification for the first technique. Combining these two results with the ones obtained in di-leptonic and all-hadronic channels (with 5.1 and 2.9 fb^{-1} respectively) [15], top quark pair production cross section has been measured to be:

$$\sigma_{t\bar{t}} = 7.50 \pm 0.31(\text{stat.}) \pm 0.34(\text{syst.}) \pm 0.15(\text{theory}) \text{ pb} \quad (1.10)$$

corresponding to a total uncertainty of 6.5%.

D0 measurement has been obtained analysing data corresponding to an integrated luminosity of 5.3 fb^{-1} [16]. Three different analysis have been performed using different techniques to separate signal from background. The first one exploits specific kinematic features of $t\bar{t}$ events (kinematic method in the following), the second uses b-jet identification capability (b-tagging method in the following) and the third uses both techniques (combined method in the following). The three results are reported below, assuming a top quark mass of 172.5 GeV:

$$\sigma_{t\bar{t}} = 7.68 \pm 0.31(\text{stat.})^{+0.64}_{-0.56}(\text{syst.}) \text{ pb} \quad \text{kinematic method}, \quad (1.11)$$

$$\sigma_{t\bar{t}} = 8.13 \pm 0.25(\text{stat.})^{+0.99}_{-0.86}(\text{syst.}) \text{ pb} \quad b\text{-tagging method}, \quad (1.12)$$

$$\sigma_{t\bar{t}} = 7.78 \pm 0.25(\text{stat.})^{+0.73}_{-0.59}(\text{syst.}) \text{ pb} \quad \text{combined method} \quad (1.13)$$

where the first error comes from statistics and the second from systematics. All results are limited by systematics. The main sources come from luminosity, signal modelling, jet reconstruction and b-jet identification for the last two techniques. The result obtained with the combined method has been further combined with the measurement performed in the di-leptonic channel with 5.4 fb^{-1} [17]. Top quark pair production cross section has been measured to be:

$$\sigma_{t\bar{t}} = 7.56^{+0.63}_{-0.56}(\text{stat.+syst.}) \text{ pb.} \quad (1.14)$$

Both the CDF and the D0 results are consistent with the SM prediction [12]: $\sigma_{t\bar{t}} = 7.46^{+0.48}_{-0.67}$ pb.

The measurement of top quark pair production cross section at the LHC is important, because it enables to extend QCD testing and new physics search to a higher energy scale. Furthermore $t\bar{t}$ rate production is enhanced by a factor 20 with respect to the Tevatron and so very precise results have been achieved even with $\frac{1}{4}$ of the Tevatron luminosity.

This analysis has been performed by both the ATLAS and the CMS collaborations in semi-leptonic, di-leptonic, lepton+τ and all-hadronic channels. Different techniques have been used relying or not on b-jet identification.

Chapter 3 is dedicated to the measurement of this cross section using a counting method. The analysis has been performed selecting lepton+jets events using the whole 2010 data collected by the ATLAS detector. Using the statistics available at the present day of writing more accurate measurements have been performed and briefly described in the following.

The most accurate one, obtained by the ATLAS collaboration, has been done in the semi-leptonic channel with an integrated luminosity of 0.70 fb^{-1} [18]. The measurement has been performed not relying on b-jet identification, but exploiting the specific kinematic features of $t\bar{t}$ events to separate the signal from the backgrounds. A likelihood has been built relying on four discriminating variables and the top quark pair cross section has been measured to be:

$$\sigma_{t\bar{t}} = 179.0 \pm 3.9(\text{stat.}) \pm 9.0(\text{syst.}) \pm 6.6(\text{lumi.}) \text{ pb}. \tag{1.15}$$

The obtained result is in agreement with NNLO theoretical predictions and, with a total uncertainty of 7%, it exceeds the precision of the theoretical calculation. This measurement is already limited by systematics. The most important contributions come from signal modelling, JES uncertainty and muon identification uncertainty.

The most accurate CMS value has been obtained combining the measurements performed in the electron+jets and muon+jets channels, using data corresponding to an integrated luminosity of 0.8 and 1.1 fb^{-1} respectively [19]. Signal events have been selected using b-jets identification. The cross section has been extracted thanks to a maximum likelihood fit. The obtained result is:

$$\sigma_{t\bar{t}} = 164.4 \pm 2.8(\text{stat.}) \pm 11.9(\text{syst.}) \pm 7.4(\text{lumi.}) \text{ pb} \tag{1.16}$$

in agreement with NNLO theoretical predictions. The uncertainty of 8.7% is dominated by systematics and the main contributions are JES and b-jet identification uncertainty.

Both measurements are already limited by systematics. Improvements can be obtained using more sophisticated techniques and clever profiling. The collection of more data itself will also help. Selection of events in the side-bands will enable to improve detector calibrations and increasing statistics will also permit to choose signal regions affected by higher statistical uncertainty but less sensitive to systematics. A possible limitation may however come from the uncertainty on luminosity, which is at the moment at the level of 4%. Improvements on this uncertainty are foreseen, moreover strategies involving cross section ratios, as done by the CDF collaboration, will be explored in order to overcome this.

1.4.2 Top quark charge asymmetry

This section is dedicated to top quark charge asymmetry measurement, which is one of the main topic of this thesis. The Section is organized as follows. After a

brief description of SM and BSM predictions, the measurements performed at the Tevatron and at the LHC by the CMS collaboration will be presented. The analysis realized by the ATLAS collaboration will be detailed in the Chapter 4.

Top quark charge asymmetry in the SM

Top quark charge asymmetry can only occur in asymmetric initial states in top quark pair production, so the main contribution comes from $q\bar{q}$ annihilation. It consists in the fact that the top quark is preferably emitted in the direction of the incoming quark and not in the one of the incoming antiquark, as shown in figure 1.8.

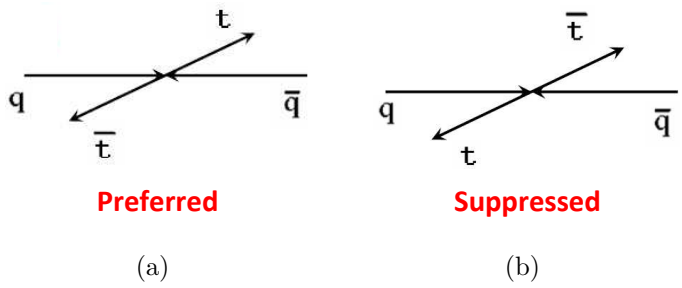

(a) (b)

Figure 1.5: *Schematic view of top quark pair charge asymmetry.*

Within the SM this asymmetry appears at NLO. QCD at tree level (LO) predicts that $t\bar{t}$ quark pair production at hadron colliders is charge symmetric, namely the differential charge asymmetry defined as [20]:

$$A(\cos\theta) = \frac{N_t(\cos\theta) - N_{\bar{t}}(\cos\theta)}{N_t(\cos\theta) + N_{\bar{t}}(\cos\theta)} \tag{1.17}$$

vanishes for every value of θ, where $N_{t(\bar{t})}(\cos\theta)$ is the number of top (antitop) quarks produced at a certain angle θ with respect to the incoming quark direction. Nevertheless, an asymmetry is generated at NLO from the interference of the diagrams shown in figure 1.6. The interference between tree level and one loop diagrams (first

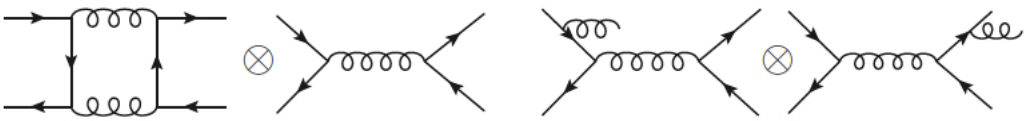

Figure 1.6: *Feynman diagrams contributing to the QCD charge asymmetry in quark-antiquark production.*

two diagrams) leads to a positive asymmetry, while the interference between ISR

and FSR diagrams (last two diagrams) leads to a negative one. The former is larger than the latter, so the resulting asymmetry is expected to be positive.

For what concerns the two other top quark pair production mechanisms: qg originated processes generate a contribution to the asymmetry much smaller than $q\bar{q}$ and gg fusion is obviously symmetric.

Top quark charge asymmetry has been measured at the Tevatron as forward-backward asymmetry.

In proton-antiproton collisions, the incoming quark will be mainly a valence quark from the proton, while the incoming antiquark will be a valence antiquark of the antiproton. As a consequence the direction of the incoming quark is well represented by the one of the proton beam. Top quark charge asymmetry translates, therefore, in the fact that the top quark is preferentially emitted in the direction of the proton beam (see Figure 1.7).

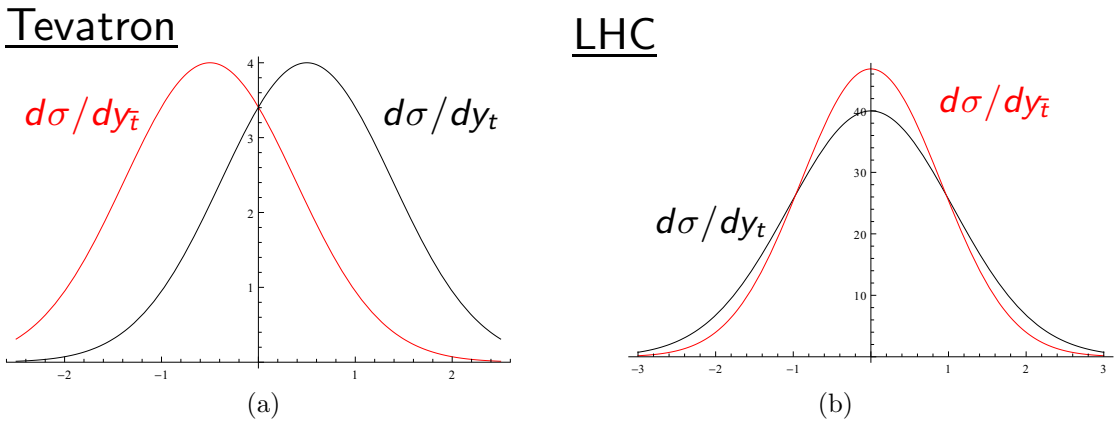

(a) (b)

Figure 1.7: *Top and antitop quark rapidity distributions: comparison between Tevatron (a) and LHC (b). While at Tevatron the charge asymmetry manifests itself in the fact that top quarks are preferentially emitted in the proton beam direction, at LHC it shows up in the fact that top quark rapidity distribution is broader than antitop quark one.*

If we consider the proton beam direction as forward and the antiproton one as backward, this relation converts into a forward-backward asymmetry. The most natural variable to study is:

$$A_{FB} = \frac{N(\Delta y > 0) - N(\Delta y < 0)}{N(\Delta y > 0) + N(\Delta y < 0)} \tag{1.18}$$

where A_{FB} is the forward-backward asymmetry, Δy is defined as the difference between top and antitop rapidities calculated with respect to proton beam direction ($\Delta y = y_t - y_{\bar{t}}$).

The LHC is a proton-proton machine, thus its initial state is symmetric and the forward-backward asymmetry vanishes. Top quark pair production asymmetry shows up in a different way. Quarks in the initial state will mainly be valence quarks, whereas antiquarks will always be sea quarks. As a consequence, the quark momentum fraction will be more frequently higher than the antiquark one and so top quarks, emitted preferentially in the incoming quark direction, will be more boosted than the antitop quarks, as shown in figure 1.8.

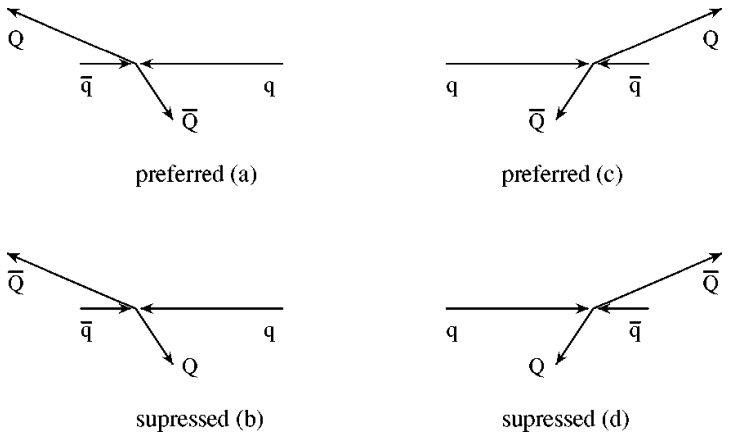

Figure 1.8: *Schematic view of top quark pair charge asymmetry at the LHC.*

Top quarks will be consequently characterized by a broader rapidity distribution with respect to the one of antitop, as can be seen in Figure 1.7.

Some variables which are sensible to the asymmetry are:

$$\Delta|\eta| = |\eta_t| - |\eta_{\bar{t}}| \tag{1.19}$$

$$\Delta|y| = |y_t| - |y_{\bar{t}}| \tag{1.20}$$

$$\Delta y^2 = y_t^2 - y_{\bar{t}}^2 \tag{1.21}$$

where $y_{t(\bar{t})}$ and $\eta_{t(\bar{t})}$ are top (antitop) rapidity and pseudorapidity respectively.

Based on this observation some observables have been conceived to measure the top quark charge asymmetry. The first one has been used by the ATLAS collaboration and it is defined as [21]:

$$A_C(\Delta|y|) = \frac{N(\Delta|y| > 0) - N(\Delta|y| < 0)}{N(\Delta|y| > 0) + N(\Delta|y| < 0)} \tag{1.22}$$

where $N(\Delta|y| > 0)$ is the number of events in which $\Delta|y|$ is positive, while $N(\Delta|y| < 0)$ is the number of events in which $\Delta|y|$ is negative.

The CMS collaboration in the most recent measurement has used a slightly different, but completely equivalent observable:

$$A_C(\Delta y^2) = \frac{N(\Delta y^2 > 0) - N(\Delta y^2 < 0)}{N(\Delta y^2 > 0) + N(\Delta y^2 < 0)} \tag{1.23}$$

where $N(\Delta y^2 > 0)$ is the number of events in which Δy^2 is positive, while $N(\Delta y^2 < 0)$ is the number of events in which Δy^2 is negative.

Other interesting observables that can be used are the so called forward and central asymmetry:

$$A_{central} = \frac{N(y_t < y_0) - N(y_{\bar{t}} < y_0)}{N(y_t < y_0) + N(y_{\bar{t}} < y_0)} \tag{1.24}$$

$$A_{forward} = \frac{N(y_t > y_0) - N(y_{\bar{t}} > y_0)}{N(y_t > y_0) + N(y_{\bar{t}} > y_0)} \tag{1.25}$$

where y_t and $y_{\bar{t}}$ are top and antitop quark rapidity respectively and y_0 is a free parameter. These two quantities are based on the fact that the number of top quarks is expect to be higher than the number of antitop quarks in the forward region and lower in the central one.

As already mentioned before, the asymmetry in the SM is small, since it appears only at NLO. The predicted value at the Tevatron is $(6 \pm 1)\%$ [22] [23] [24], while only $(1.30 \pm 0.11)\%$ asymmetry is expected at LHC, since top quark pair production is dominated by gg fusion [25].

Top quark charge asymmetry in BSM theories

Some BSM models predict however significant deviations of the asymmetry value from the one predicted by the SM. New physics contributions can enhance or decrease the SM asymmetry. As will be shown in the next section, Tevatron measurements have however excluded the presence of significant negative contributions. Only BSM models giving positive contributions to the asymmetry will be therefore discussed in the following.

Most of the proposed models predict the existence of a new particle that can contribute in $q\overline{q} \to t\bar{t}$ process in $s-$,$u-$, or $t-$channel. All possible vector bosons and scalars contributing have been classified in [26], the most popular ones are described below.

- *Axigluons:*
  This model predicts the presence of a color octet vector G^μ (axigluon) with axial couplings to quarks, which is produced in the s-channel. Such kind of particle is foreseen by the so-called "chiral models": QCD $SU(3)$ symmetry is considered to come from an higher symmetry group $(SU(3)_L \times SU(3)_R)$; the breaking of this more general symmetry originates 8 massless bosons (gluon) and 8 massive bosons (axigluon).

This new particle will show up as a bump in di-jets or $t\bar{t}$ invariant mass spectra. No excesses have been observed at the moment, so it has to have a large mass in order not to be produced on-shell. The contribution to the charge asymmetry can be dominated by the interference with SM diagrams or by the BSM squared amplitude. The interference term is proportional to $(-g_q \cdot g_t)$, where g_q is the coupling of axigluon with light quarks and g_t with top quark. Therefore, in order to have a positive asymmetry either the couplings are so large that the second term dominates or the coupling of the axigluon with the third family has opposite sign with respect to the one with light quarks.

- *Z' and W' boson:*
  A neutral vector boson B_μ or a charged boson B^1_μ, like Z' and W' bosons predicted by GUT, can be exchanged in the $t-$channel as in Figure 1.9:
  - $u\bar{u} \to t\bar{t}$ (Z'),
  - $d\bar{d} \to t\bar{t}$ (W').

  As can be seen from the diagrams, $t\bar{t}$ production requires flavour violating couplings, in particular flavour changing neutral currents are foreseen for Z'.

  In order to have at Tevatron energy an increase of the asymmetry and no excesses in $t\bar{t}$ production cross section, Z' and W' couplings should be large and the contribution to $\sigma_{t\bar{t}}$ coming from SM-BSM interference $(\delta\sigma_{int})$ should cancel with BSM squared amplitude $(\delta\sigma_{quad})$: $\delta\sigma_{int} + \delta\sigma_{quad} \sim 0$. The cancellation can not occur at the LHC too, so excesses in $m_{t\bar{t}}$ tails are foreseen.

  Another constraint to Z' model comes from the fact that it predicts the production of same sign tops (see Figure 1.10), which are still unobserved. This can be overcome by choosing particular Z' models.

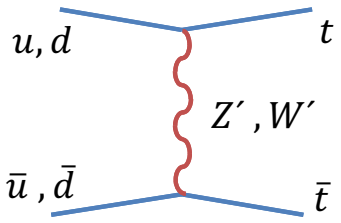

Figure 1.9: *Feynman diagram contributing to $t\bar{t}$ charge asymmetry involving Z' or W' bosons.*

- *Scalar triplet / scalar sextet:*
  An exotic scalar, colour triplet (ω^4) or colour sextet (Ω^4), with flavour violating couplings can be exchanged in the $u-$channel: $u\bar{u} \to t\bar{t}$ (see Figure 1.11). These particles are both bosonic colored states differing by their couplings

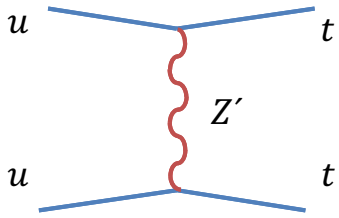

Figure 1.10: *Feynman diagram for same sign tt pair production.*

to quarks. For ω^4, the antisymmetry in colour indices implies that diagonal couplings to uu, tt identically vanish. For Ω^4, processes like $uu \to uu$ and $uu \to tt$ are at the contrary possible, but the production of same sign tops have not been observed yet. Specific models can however avoid this.

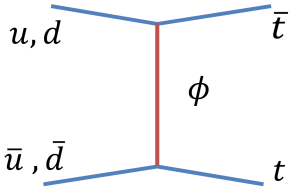

Figure 1.11: *Feynman diagram contributing to $t\bar{t}$ charge asymmetry involving Ω^4 or ω^4 scalars.*

The various models predict different values of the asymmetry at the LHC and at the Tevatron and different dependencies with respect to $t\bar{t}$ kinematic variables, in particular the top quark pair invariant mass ($m_{t\bar{t}}$).

The measurement of the charge asymmetry at the two colliders will give the possibility to discriminate between these models. The relation between the new physics contribution at the Tevatron (A_{FB}^{new}) for $m_{t\bar{t}} > 450$ GeV with the one to inclusive asymmetry at the LHC (A_C^{new}) is presented in Figure 1.12 (a), for the five models studied. This plot has been obtained considering couplings values in agreement with the constraints on the $t\bar{t}$ cross section and tail mentioned above. This plot exhibits a clear difference between W' boson and the rest of models, due to the different $u\bar{u}$ and $d\bar{d}$ parton densities at the two colliders. At the Tevatron ($p\bar{p}$ collider) both u, d from the proton and $\bar{u}$, $\bar{d}$ from the antiproton are valence quarks, so that $d\bar{d}$ is roughly $\frac{1}{4}$ smaller than $u\bar{u}$. At the LHC (pp) both $\bar{u}$, $\bar{d}$ are sea quarks and $d\bar{d}$ is only $\frac{1}{2}$ smaller than $u\bar{u}$. If the new physics contribution to the Tevatron asymmetry is sizeable, as suggested by the CDF measurement that will be described in the following, at the LHC W' boson could be distinguished from the rest of models by a measurement of A_C with a relative precision of around 20%. It can

be also observed that for the Z' boson there are minimum asymmetries $A_{FB}^{new} \geq 0.32$ and $A_C^{new} \geq 0.04$. This effect is due to the constraints coming from top quark pair measured cross section values.

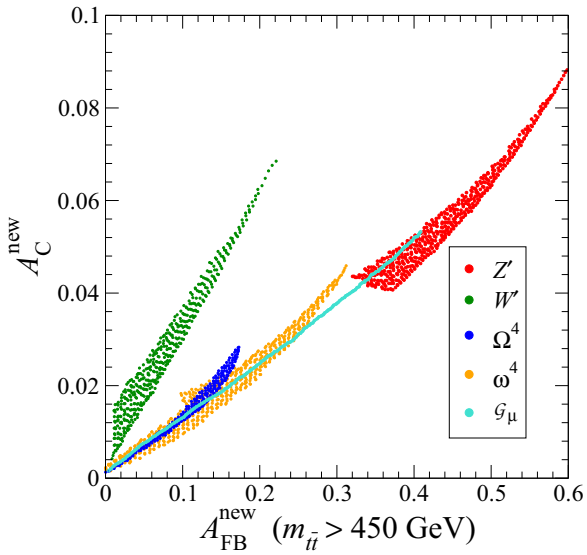

(a)

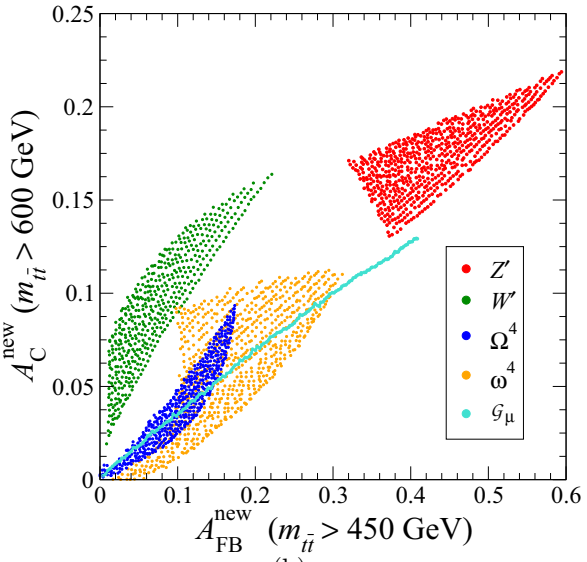

(b)

Figure 1.12: *Allowed regions for the new physics contributions to the FB asymmetry at Tevatron and the inclusive charge asymmetry at LHC (a). Allowed regions for the new physics contributions to the forward-backward asymmetry at Tevatron and the charge asymmetry at LHC for* $m_{t\bar{t}} > 600$ *GeV (b) [27].*

In Figure 1.12 (b) new physics contributions to the Tevatron asymmetry for $m_{t\bar{t}} > 450$ GeV are compared to the ones to the LHC asymmetry at high $t\bar{t}$ invari-

ant mass: $m_{t\bar{t}} > 600$ GeV. It can be seen that for Z' boson exchange the asymmetry enhancement is much more pronounced than for the rest of models and a measurement with a relative precision of $\sim 20\%$ would likely distinguish this model from the rest.

Axigluons, scalar triplet and scalar sextet can be distinguished looking at the distribution of the asymmetry as a function of $m_{t\bar{t}}$. While the contribution from axigluon increases significantly at large $m_{t\bar{t}}$, the increment for Ω^4 is less pronounced and for ω^4 a decrease at high $m_{t\bar{t}}$ is foreseen (see Figure 1.13).

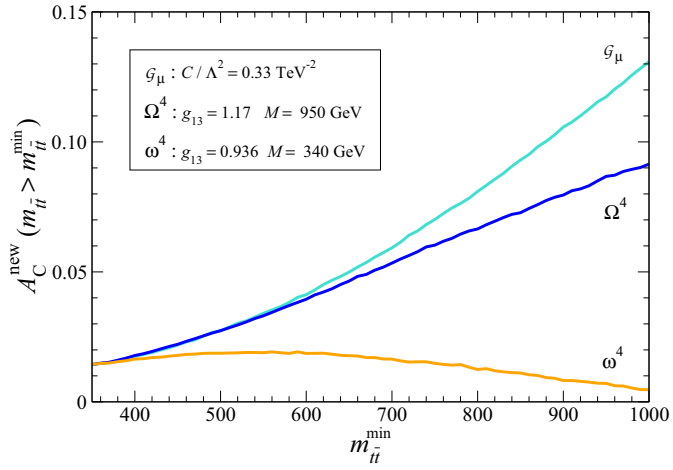

Figure 1.13: *Dependence of the charge asymmetry at LHC on the $m_{t\bar{t}}$ cut, for a point with $A_{FB}^{new} \simeq 0.13$, $A_C^{new} \simeq 0.016$ (inclusive) [27].*

Various BSM contributions have also a different dependence on $t\bar{t}$ angular distributions [28]. The sensitivity to new physics can be therefore enhanced by comparing the measurements in central and forward regions.

Tevatron measurements

Top quark forward-backward asymmetry has been measured both in lepton+jets and di-lepton channel. Two techniques have been explored: the first one performing the reconstruction of top and antitop directions and the other based on leptons angular distributions. Furthermore, differential asymmetry as a function of $m_{t\bar{t}}$ has been measured in lepton+jets channel. The most recent results are discussed in the following.

Inclusive asymmetry in lepton+jets channel
The most recent measurements have been performed by CDF [29] and D0 [30] using an integrated luminosity of 5.3 fb^{-1} and 5.4 fb^{-1} respectively. Top and antitop quarks rapidities have been reconstructed from decay products with techniques similar to the one that will be described in Section 4.4 and an unfolding technique has

been used to correct for detector and acceptance effects. The results obtained in the $t\bar{t}$ rest frame are reported below:

$$A^{FB} = (15.8 \pm 7.2(\text{stat.}) \pm 1.7(\text{sys.}))\% \qquad \text{CDF} \tag{1.26}$$

$$A^{FB} = (19.6 \pm 6.5(\text{stat.})^{+1.8}_{-2.6}(\text{sys.}))\% \qquad \text{D0} \tag{1.27}$$

and are higher than the SM prediction by a factor 2 σ.

These results are still affected by a significant statistical uncertainty. The most important systematic contributions come from signal modelling, especially ISR and FSR, uncertainty on background contamination and on jet reconstruction.

Differential asymmetry in lepton+jets channel
Both the CDF [29] and the D0 [30] collaborations have also measured the charge asymmetry as a function of top quark pair invariant mass ($m_{t\bar{t}}$). While CDF has seen a strong mass dependence, D0 result seems almost independent from $m_{t\bar{t}}$, as can be seen in Figure 1.14.

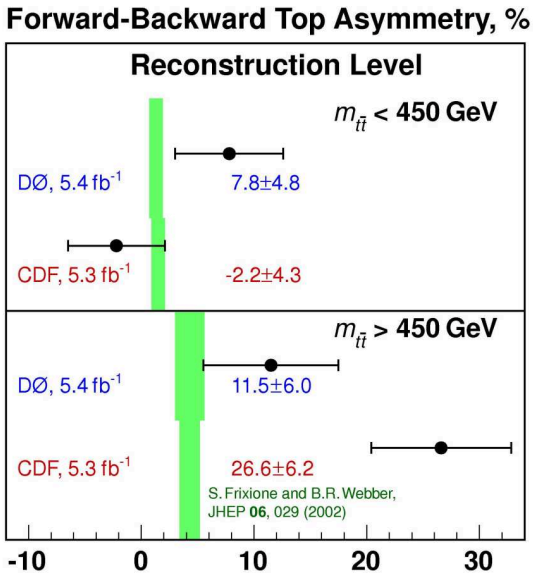

Figure 1.14: *Tevatron measurements of top quark charge asymmetry in two bins of top quark pair invariant mass. These results have not been unfolded to correct for detector resolution and acceptance effects [31].*

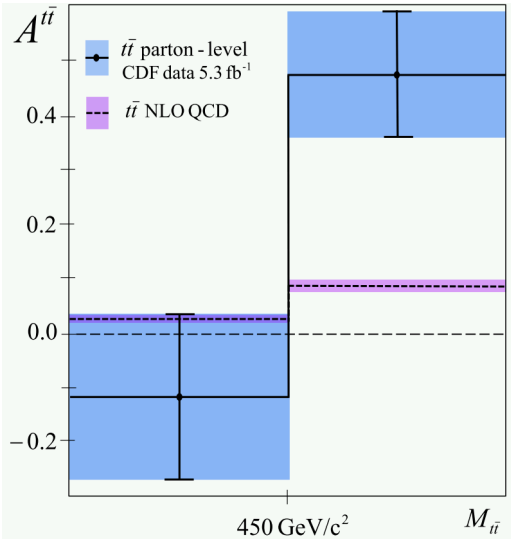

Figure 1.15: *CDF measurement of top quark charge asymmetry in two bins of top quark pair invariant mass at production level: [29]: the result has been unfolded to correct for detector resolution and acceptance effects.*

The CDF collaboration, in particular, has measured the asymmetry separately for events with $m_{t\bar{t}} < 450$ GeV and $m_{t\bar{t}} > 450$ GeV and corrected the results for acceptance and detector effects (see Figure 1.15). The measured asymmetry for high invariant mass is $A_{FB} = (48 \pm 10(\text{stat.}) \pm 5(\text{sys.}))\%$, 3 σ higher than SM prediction of $A_{FB}^{MCFM} = (9 \pm 1)\%$. The CDF result has generated a lot of excitement: if this will be confirmed it can be indeed a hint of new physics.

Inclusive asymmetry in lepton+jets channel, using lepton variables
In the same channel, D0 collaboration has measured the charge asymmetry using the leptons in each event. Since there is a correlation between the direction of top and antitop quarks and the one of the leptons coming from their decay, top-antitop forward-backward asymmetry translates into the fact that more positive leptons are emitted in the forward direction and more negative leptons in the backward one. Charge asymmetry can be measured therefore as:

$$A_{FB}^{l} = \frac{N_F^l - N_B^l}{N_F^l + N_B^l} \tag{1.28}$$

where N_F^l is the number of events that have $q_l y_l > 0$ and N_B^l is the number of events

Asymmetry	Channel	Measurement (%)	SM prediction (%)
CDF: inclusive	l+jets	$15.8 \pm 7.2(\text{stat.}) \pm 1.7(\text{sys.})$	6 ± 1
D0: inclusive	l+jets	$19.6 \pm 6.5(\text{stat.})^{+1.8}_{-2.6}(\text{sys.})$	6 ± 1
CDF: $m_{t\bar{t}} > 450$ GeV	l+jets	$48 \pm 10(\text{stat.}) \pm 5(\text{sys.})$	9 ± 1
D0: inclusive (lepton)	l+jets	$15.2 \pm 3.8(\text{stat.})^{+1.0}_{-1.3}(\text{sys.})$	2.1 ± 0.1
CDF: inclusive	di-lepton	$42 \pm 15(\text{stat.}) \pm 5(\text{sys.})$	6 ± 1
CDF: inclusive (lepton)	di-lepton	$21 \pm 7(\text{stat.}) \pm 2(\text{sys.})$	not available

Table 1.3: Summary of the measurements and the relative SM predictions.

with $q_l y_l < 0$.

The correlation between top quark and lepton directions is not perfect and so the expectation value is $(2.1 \pm 0.1)\%$. After correcting for detector and acceptance effects, the measured value is $A^l_{FB} = (15.2 \pm 3.8(\text{stat.})^{+1.0}_{-1.3}(\text{sys.}))\%$, $\sim 3\ \sigma$ higher than the prediction.

Inclusive asymmetry in di-lepton channel
The CDF collaboration has performed this analysis also in the di-lepton channel [32], using two different techniques. The first one is based on the reconstruction of top and antitop kinematics and the measured value in the $t\bar{t}$ rest frame is:

$$A_{FB} = (42 \pm 15(\text{stat.}) \pm 5(\text{sys.}))\% \tag{1.29}$$

which is 2.3 σ higher than the SM prediction.

The result is limited by statistical uncertainty; the most important sources of systematic uncertainties comes from background subtraction, signal modelling and jet reconstruction.

Inclusive asymmetry in di-lepton channel, using lepton variables
The second method takes advantage from the correlation between top and antitop quarks directions and the one of leptons coming from their decay. The difference between top and antitop quarks rapidities is replaced with the one between positive and negative leptons in the event. The lepton based asymmetry is measured to be:

$$A^{\Delta\eta}_{FB} = \frac{N(\Delta\eta_l > 0) - N(\Delta\eta_l < 0)}{N(\Delta\eta_l > 0) + N(\Delta\eta_l < 0)} = 0.21 \pm 0.07(\text{stat.}) \pm 0.02(\text{sys.}) \tag{1.30}$$

where $\Delta\eta = \eta_{l^+} - \eta_{l^-}$ and the systematic uncertainty is mainly due to background subtraction.

This result has not been corrected for detector and acceptance effects yet, so it's not directly comparable with predictions.

The summary of all results and the relative SM predictions are reported in Table 1.3.

LHC measurements

The measurement performed by the ATLAS collaboration will be described in detail in Chapter 4. For what concerns the CMS collaboration the analysis has been performed in lepton+jets channel using data corresponding to an integrated luminosity of 1.1 fb^{-1}[33]. The kinematics of each event is reconstructed using a technique very similar to the one that will be described for the ATLAS analysis (see Section 4.4) and then an unfolding technique has been used to correct for acceptance and detector effects. The measured asymmetry has been found to be:

$$A_C^y = -0.013 \pm 0.026(\text{stat.})^{+0.026}_{-0.021}(\text{syst.}) \tag{1.31}$$

where the most important sources of systematic uncertainty comes signal modelling and JES.

The result is in agreement with the SM prediction within the uncertainty.

In addition, the CMS collaboration has measured the asymmetry as a function of the top quark pair invariant mass, as can be seen in Figure 1.16. The plot doesn't show any dependence of the asymmetry with respect to $m_{t\bar{t}}$. The distribution can't be however directly compared to theoretical prediction and to CDF result, since it has not been corrected for acceptance and detector effects.

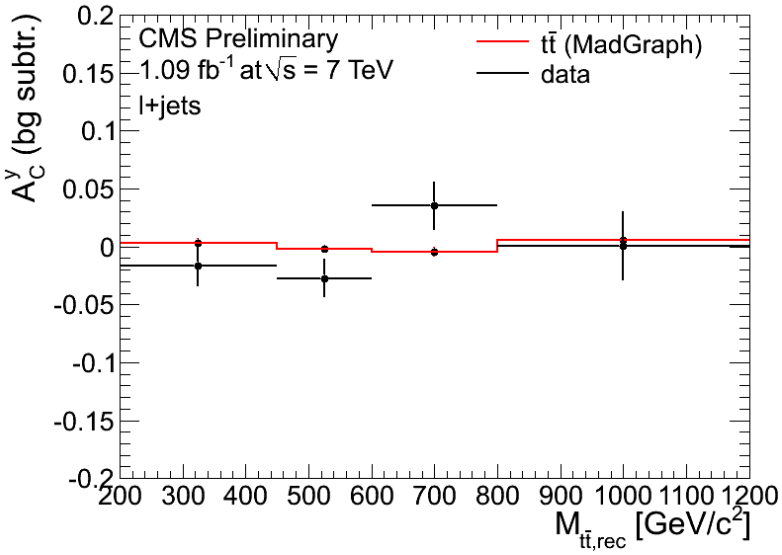

Figure 1.16: *CMS measurement of top quark charge asymmetry as a function of top quark pair invariant mass at reconstruction level [33]. This results have not been unfolded to correct for detector resolution and acceptance effects.*

Chapter 2

The LHC and the ATLAS experiment

ATLAS (A Toroidal LHC ApparatuS) is one of the four main experiments at the Large Hadron Collider (LHC) at CERN. In this chapter a brief introduction to the LHC collider and its physics program is given, together with a description of the ATLAS detector. The methods for the reconstruction and identification of physics objects involved in top quark events are also discussed. Finally some relevant performance results of the detector with pp collisions at 7 TeV centre-of-mass energy are reviewed.

2.1 The LHC collider

The LHC [34] is at present the largest and highest-energy particle accelerator in the world.

It has been built at CERN, in the circular tunnel that housed the Large Electron Positron Collider (LEP). It is a 27 km long tunnel, dug at a depth varying between 50 and 175 meters below the ground.

The LHC had been designed to provide both proton-proton (pp) and heavy ion (HI) collisions. For pp collisions, the design luminosity[1] is 10^{34} cm^{-2}s^{-1} and the foreseen centre-of-mass energy for the collision is 14 TeV. During the 2010 and 2011 runs, collisions at 7 TeV centre-of-mass energy have been provided.

[1] Luminosity is defined as

$$L = f \cdot \frac{n_1 \cdot n_2}{4 \cdot \pi \cdot \sigma^2} \cdot F \tag{2.1}$$

where σ is the transverse width of the beam (17 μm at the LHC at nominal conditions), assuming a gaussian particle distribution in the beam, f is the collision frequency defined as the reciprocal of the time delay between two collisions (1/25 ns = 40 MHz), n_1 and n_2 are the numbers of particles in the two colliding beams respectively (at the LHC $\sim$ 1011 protons per bunch are foreseen at nominal conditions) and F is a reduction factor due to the crossing angle ($\sim$ 0.85 at the LHC).

For HI collisions, the project foresaw to use lead ions beams with an energy of 2.8 TeV per nucleon, reaching a peak luminosity of 10^{27} cm^{-2}s^{-1}.

The LHC is mainly composed by superconducting magnets. They operate at a temperature of 1.9 K, which is provided by a cryogenic system based on liquid helium. The LHC is equipped with a 400 MHz superconducting cavity system and it is composed with different types of magnets. Dipole magnets (for a total of 1232 magnets) are used to keep the beams on their circular trajectory, while quadrupole magnets (for a total of 392) are necessary to keep the beams focused, in order to maximize the chances of interaction in the four different interaction points, where the two beams cross. Close to these four intersection points, the LHC has straight sections, in which the two beam pipes, in which particles circulate, become one and the particles are then made to collide. Within this space, triplet magnets are used to squeeze the beam transversely, to focus it at the interaction point. Thanks to these squeeze, the beam to be transported can be significantly larger than it needs to be at the interaction point, reducing intra-beam interactions.

At the collision points, four big experiments have been built: ATLAS [35] at point 1, CMS [36] at point 5, LHCb [37] at point 8 and ALICE [38] at point 2. The first two are multi-purpose experiments, designed to study high transverse momentum events for the search of the Higgs boson and other phenomena beyond the Standard Model. LHCb has instead been designed especially to study b-physics, while ALICE was built to analyse mainly heavy ion collisions, to study the formation of a quark-gluon plasma.

A schematic view of the LHC, the two beams and the four interaction regions is shown in Figure 2.1.

Along the ring there are sections dedicated to beam cleaning. They are located at points 3 and 7 and they include collimators that maintain the stability of the beam. They are designed to scatter particles with deviant momenta and large betatron[2] amplitudes. Furthermore, in point 6 a system is set up in order to dump the beams in case of problems or at the end of its lifetime during normal operation.

Colliding particles in the LHC are bunched together into bunches, made of $\sim 10^{11}$ protons. The design number of bunches is 2808, so that interactions happen every 25 ns.

Before being injected into the LHC, the particles are accelerated step by step up to the injection energy of 450 GeV, by a series of accelerators. For protons, the first system is the linear accelerator LINAC2, which generates them at an energy of 50 MeV. The protons then go through the Proton Synchrotron Booster (PSB) and are accelerated to 1.4 GeV. After that they are injected into the Proton Synchrotron (PS), where they are accelerated to 26 GeV. Finally, the Super Proton Synchrotron (SPS) is used to further increase their energy to 450 GeV. For lead ions the production is different. They are first accelerated by the linear accelerator LINAC 3. Then the Low-Energy Ion Ring (LEIR) is used as an ion storage and cooler unit.

[2]Betatron oscillations are transverse oscillations of particles in a circular accelerator about the equilibrium orbit.

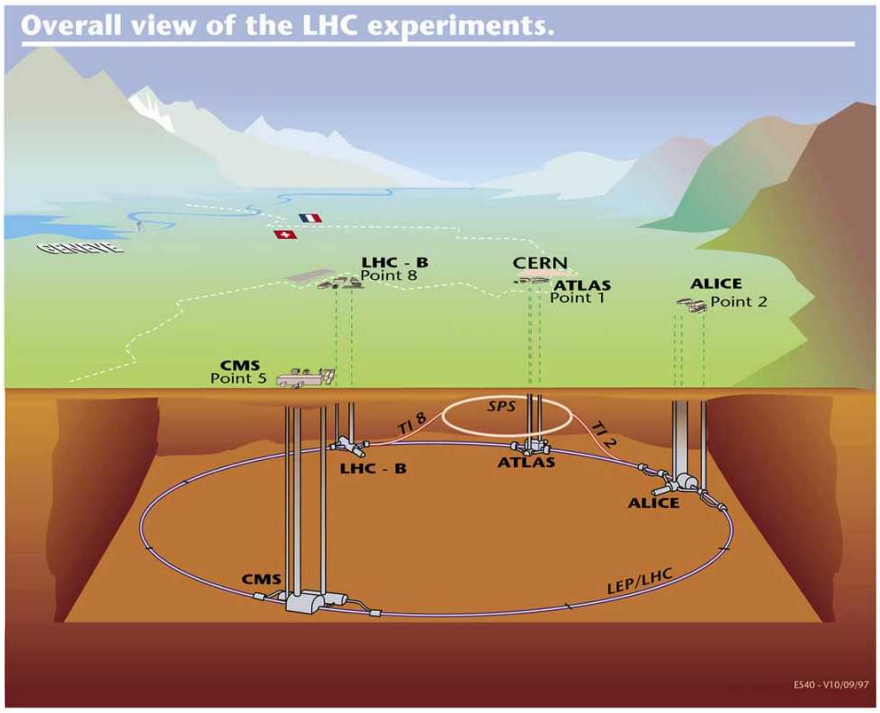

Figure 2.1: *A schematic view of the LHC, its two beams and the four interaction regions.*

The ions are then further accelerated by the PS and SPS before being injected into the LHC ring. The different accelerators are shown in Figure 2.2.

The LHC started its operations on 10 September 2008, with the first beams circulating into the rings, in both directions, without collisions. After a commissioning phase, first collisions were expected few days later. Unfortunately, on 19 September of the same year a major accident happened, due to a defective electrical connection between two magnets. In the accident 53 magnets were damaged. This caused a long stop of the machine, to repair the damaged magnets, to check the electrical connections and to improve the safety systems. During Autumn 2009, after more than one year stop, the operations started again, with the first collisions at a centre-of-mass energy of 900 GeV recorded by the four experiments on 23 November 2009. After a 900 GeV collisions data taking, the centre-of-mass energy was further increased to 2.36 TeV, beating the Tevatron's previous record of 0.98 TeV per beam and giving therefore collisions at the highest energy ever reached before. After some months, the first collisions at $\sqrt{s} = 7$ TeV were registered, on 30 March 2010, starting a new running period that went on until the beginning of November, when the LHC provided the first heavy ion collisions. After the lead ions collisions period and a

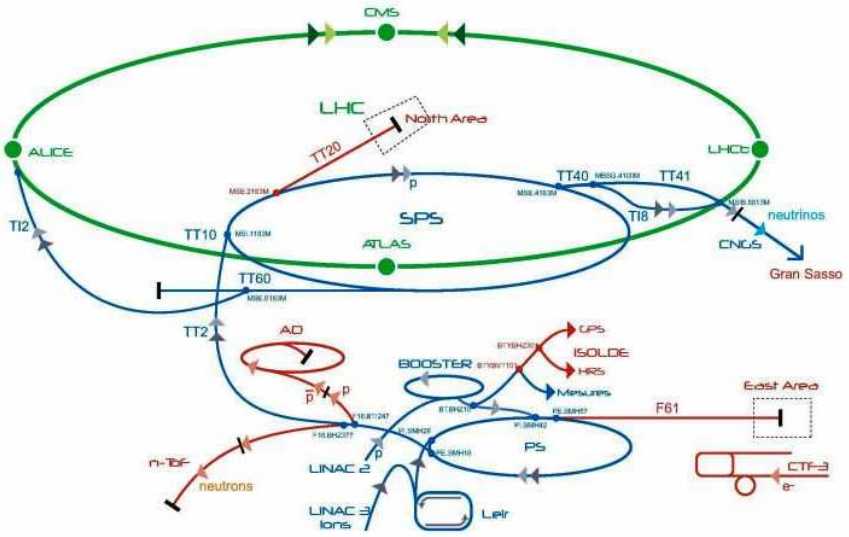

Figure 2.2: *A schematic view of the acceleration chain at CERN.*

technical stop during the winter, p-p collisions have started again on 13 March 2011.

During the commissioning phase, the number of colliding bunches has been progressively increased to reach the design value. At the end of 2010 the maximum number of colliding bunches has been 348, a maximum number of 1092 has been then reached in June 2011. At the end of 2011 pp run the number of colliding bunches is 1842: the nominal bunch separation of 25 ns has been reached. The maximum instantaneous luminosity that has been reached in 2010 is slightly higher than 2 10^{32} $cm^{-2}s^{-1}$, while during 2011 run a peak of 3.65 10^{33} $cm^{-2}s^{-1}$ has been achieved. In 2010 HI running collisions at 2.76 TeV per nucleon took place, reaching a peak instantaneous luminosity of 30 10^{24} $cm^{-2}s^{-1}$.

At the end of the 2010 pp running period, ATLAS accumulated 45 pb^{-1} of integrated luminosity, of the 48.9 pb^{-1} delivered by the LHC (upper plot in Figure 2.3(a)). Data-taking has re-started in March 2011 and at the end of the 2011 pp run 5.2 fb^{-1} were accumulated (Figure 2.3 (b)).

2.1.1 Physics at the ATLAS experiment

As mentioned before, four big experiments have been built to analyse the LHC collisions data. Their physics program covers a variety of topics in particle and nuclear physics. In the following I will concentrate on the ATLAS collaboration

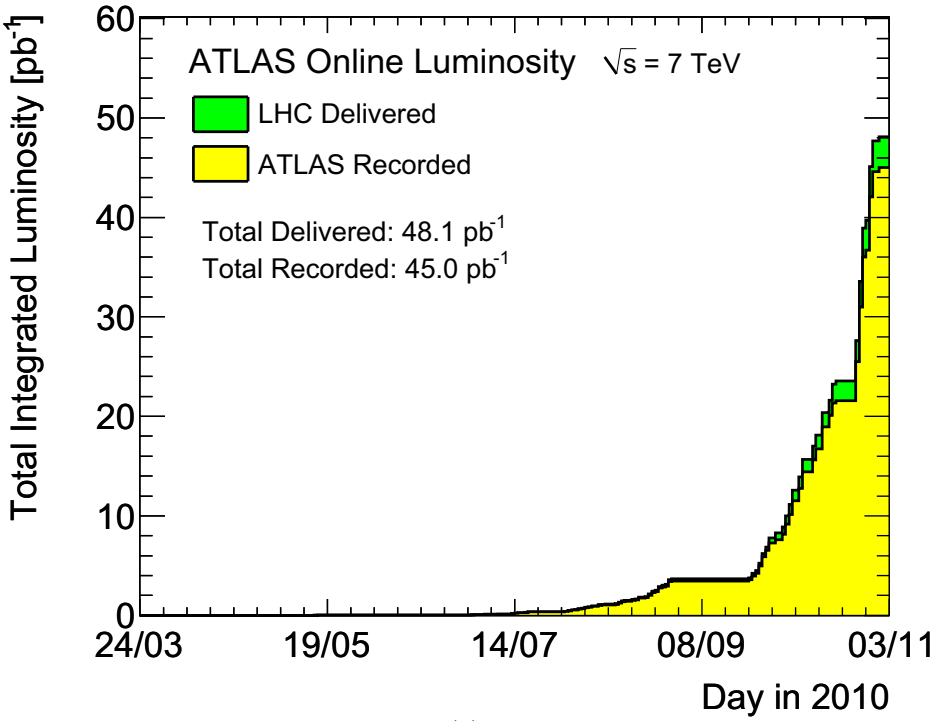

(a)

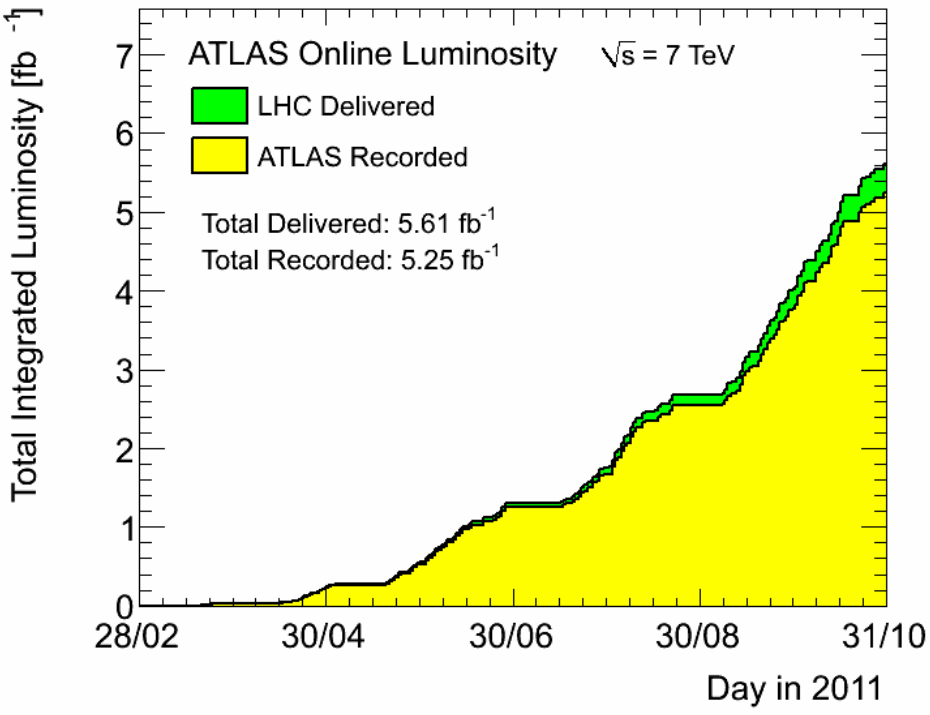

(b)

Figure 2.3: *Cumulative luminosity versus day delivered to (green), and recorded by ATLAS (yellow) during stable beams and for pp collisions at 7 TeV centre-of-mass energy. The upper plot refers to 2010, while the other to 2011 [39].*

results at the day of writing and plans.

- *Higgs boson*
  While the Standard Model (SM) of electroweak and strong interactions is in excellent agreement with the numerous experimental measurements, the dynamics responsible for electroweak symmetry breaking is still unknown. Within the SM, the Higgs mechanism is invoked to break the electroweak symmetry. A doublet of complex scalar fields is introduced, of which a single neutral scalar physical particle, the Higgs boson, remains after the symmetry breaking. Within the SM, the Higgs boson is the only particle that has not been discovered so far. The direct search at the LEP collider has led to a lower bound on its mass of 114.4 GeV [40]. Recently, the experiments at the Tevatron have excluded at 95%C.L. a SM Higgs with a mass in two mass ranges: $156 < m_H < 177$ GeV and $100 < m_H < 108$ [41]. The LHC experiments have the capability to extend the reach for a standard Higgs up to about 1 TeV. If the Higgs boson is found its mass and couplings will be determined. Higgs searches have been performed by ATLAS collaboration in different channels [42] [43] [44] [45] [46] [47] and using data corresponding to an integrated luminosity between 1 and more than 2 fb^{-1}. No significant excess ($< 2.1\ \sigma$) is found in the mass range $110 - 600$ GeV and exclusion limits at 95% C.L. have been placed in three different mass regions: $146 < m_H < 232$ GeV, $256 < m_H < 282$ GeV and $296 < m_H < 466$ GeV [48].

- *Standard Model*
  The study of SM physics is interesting for several reasons. The measurement of some of its parameters with precision can indeed open a window on new physics phenomena, that may show up in deviations with respect to the SM predictions. Furthermore, this kind of events are very useful for detector response calibration and to constraint the Parton Density Functions (PDFs). Finally they often represent a background to new physics predicted signals. Many studies have been done using 2010 and 2011 data and they show a good agreement with the SM predictions.

  In particular some studies have been done to measure gauge bosons couplings ($Z\gamma$, $W\gamma$, WW, ZW and ZZ) in different final states [49] [50] [51] [52] [53]. In addition, the kinematics of events with a W or a Z bosons has been explored [54] [55] and the charge asymmetry in W boson production has been measured [56]. These measurements have been used to constraint the PDF uncertainty [57]. Several studies have been done also in the QCD field, measuring jets spectra, their production cross sections and multiplicity [58] [59] [60] [61]. Furthermore, the production cross sections of W and Z bosons in association with QCD jets have been measured as a function of the number of jets [62] [63] [64]. The production cross sections of W and Z bosons in association with a jet originated from a b quark have been measured as well [65] [66]. Finally, for what concern the top physics sector, many studies have been done to measure

production cross sections and main properties, which are not discussed in this thesis, but documented in [67] [68] [69] [70] [71] [72] [73] [74] [75].

- *Supersymmetry*
  Many studies are dedicated to the search of Supersymmetry, which is one of the theoretically favoured candidates for physics beyond the SM. Models of supersymmetry involve new, highly massive particles. Some of them, as squarks and gluinos, usually decay into high-energy quarks and stable heavy particles that are very unlikely to interact with ordinary matter. Supersymmetric events are expected to be characterised by several high-momentum jets and missing transverse energy. ATLAS collaboration has searched for Susy events in different channels (jets+$\not\!\!E_T$, lepton(s)+$\not\!\!E_T$ and b-jets+$\not\!\!E_T$) and found no evidence of new physics [76] [77] [78] [79] [80]. Lower limits on chargino and gluino masses up to 1 TeV have been set, with 95% C.L.

- *Other Beyond the Standard Model (BSM) theories*
  BSM theories, different from Supersymmetry, are studied as well. These theories have been conceived to solve some open issues of the SM, such as the stability of electroweak symmetry breaking scale with respect to radiative corrections, the dark matter nature, neutrino masses, the large number of the SM free parameters, etc. Furthermore, some of them can explain inconsistencies between the SM predictions and the Tevatron data. This is the case of the top quark charge asymmetry measurement, already presented in detail in Chapter 1.

- *Heavy ion physics*
  The data taking with Pb-Pb collisions will give the possibility to discover new phenomena. The ALICE experiment is dedicated to HI physics, but also the other experiments have a HI program, even though they have not been designed for this purpose. In particular, thanks to the good performance of the calorimeter system, the ATLAS experiment has observed the "jetquenching" already with few pb^{-1} of data [81]. This new phenomena is characterised by large di-jet asymmetries, not observed in proton-proton collisions and it may point to an interpretation in terms of strong parton energy loss in a hot, dense medium.

The very high luminosity of the LHC is needed to pursue most of these studies, since the cross sections of the processes of interest are very low compared to the QCD jets production. High luminosity regime introduces however some difficulties as well. One of them is the presence of pile-up, that is the superposition of high cross section inelastic events over the candidates for new physics. At the design luminosity 23 pile-up events per bunch crossing are expected. The impact of pile-up on the two measurements presented in this thesis is described in the following chapters.

Another difficulty due to the nature of proton-proton collisions is that the QCD processes will dominate over the processes physicists are most interested in. This

imposes strong demands on the capability of the detectors to identify experimental signatures characteristic of the interesting processes.

The physics program therefore translates into requirements the LHC detectors have to face:

- **Fast response, high granularity and resistance to radiations.**
  The rates of events require a fast and sophisticated electronics, able to discriminate events and minimize the effect of pile-up. A high granularity of the detector is necessary to handle the high particle fluxes as well. The detectors must be resistant to high doses, both in terms of operation and aging.

- **Trigger.**
  The output bandwidth of the detector is limited and therefore the 40 MHz interaction rate must be reduced to few hundred Hz to be written to tape. The capability of triggering efficiently on interesting events with a very high background rejection is therefore crucial. The ATLAS trigger system is described in Section 2.2.5.

- **Full coverage.**
  In order to identify interesting events over the dominant QCD background, it is important to detect all particles produced in the collision. That requires a coverage over 2π in the azimuthal angle and pseudorapidity $|\eta| < 5$ (for the definition of pseudorapidity see Section 2.2).

- **Particle identification.**
  The capability to precisely reconstruct and identify electrons, muons, photons, tau leptons and jets is an essential requirement for the LHC experiments.

2.2 ATLAS

The ATLAS Experiment is positioned at Point1, in a cavern at a depth of 100 m. With its height of 25 m and its length of 44 m it is one of the biggest detectors ever built. It weights about 7000 tons and it has a cylindric symmetry. After the cavern was completed, the construction started in 2003 and it went on until July 2007, with the insertion of the innermost detector and the lowering of the last end-cap toroidal magnet. Since 2009 it has been recording cosmic-ray events and, since November 2009, proton-proton collision events at rates of up to 400 Hz.

To aid with the description of the detector, a brief summary of the coordinate system and nomenclature is given.

- The nominal interaction point is defined as the origin of the coordinate system.

- The z-axis is parallel to the beam and the x and y axes are perpendicular to the beam forming a right-handed cartesian coordinate system where x points

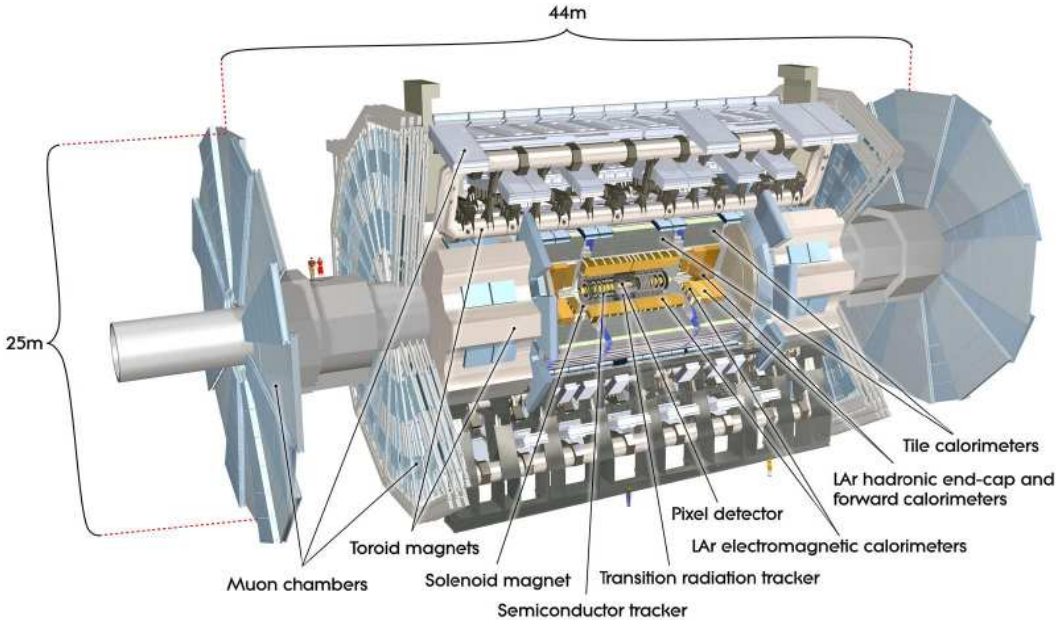

Figure 2.4: *A schematic view of the ATLAS detector [35].*

towards the centre of the LHC ring and y points upward. The x-y plane is called the transverse plane.

- The azimuthal angle, ϕ, is measured around the z-axis and the polar angle, θ, is measured from the z-axis.
- The pseudorapidity, defined as $\eta = -ln\tan(\theta/2)$, is often preferable as a polar coordinate, since pseudorapidity spectra are invariant under Lorentz boosts along z-axis.
- The distance ΔR in $\eta - \phi$ space is defined as $\Delta R = \Delta\eta^2 + \Delta\phi^2$.
- Particles are often described by their transverse momentum p_{T} and transverse energy (projections in the transverse plane), as these variables are a better indicator of interesting physics than the standard energy and momentum and because they are fixed to 0 in the initial state.

The ATLAS detector is composed of different subdetectors, as shown in Figure 2.4. Each of them plays an important role in the reconstruction of particles. The sub-detectors are arranged in layers leading out from the interaction point.

Closest to the beam pipe is the Inner Detector, used to reconstruct the trajectory of the charged particles and divided into Pixel, SemiConductor Tracker (SCT) and Transition Radiation Tracker (TRT) detectors. It covers $|\eta| < 2.5$. The whole system is enclosed by a solenoid magnet, which provides a magnetic field of 2 T that bends the charged particles and allows, as a consequence, a measurement of their momentum and charge. The inner and outer diameters of the solenoid are 2.46 m and 2.56 m and its axial length is 5.8 m. The flux is returned by the steel of the ATLAS Hadronic Calorimeter (Had Calorimeter) and its girder structure. As a result there is a negligible field within the Electromagnetic Calorimeter (EM Calorimeter) volume and a small field in the Had Calorimeter volume. To achieve the desired calorimeter performance, the solenoid layout has been carefully optimised to keep the material thickness in front of the calorimeter as low as possible: the solenoid assembly contributes a total of ~ 0.66 radiation lengths (X_0) at normal incidence.

The EM Calorimeter encloses the tracking chamber and is designed to precisely measure the energy of electrons and photons. Outside the EM Calorimeter there is the Had Calorimeter, which measures the energy of hadronic particles. The calorimeter system is hermetic out to $|\eta| < 4.9$ and it is $\sim 9 - 13$ radiation lengths thick, sufficient to capture the 99% of hadronic showers from single charged pions up to ~ 500 GeV.

Finally, the calorimeters are enclosed by the Muon Spectrometer, designed to reconstruct and identify muons. It is immersed in a magnetic field and it covers $|\eta| < 2.7$ with tracking chambers that provide precise measurements of momentum and charge and detectors used for fast triggering. The system that generates the magnetic field for the Muon Spectrometer is composed of three large air-core toroids: one barrel component and two end-caps. The field is centred on the beam axis, perpendicular to the solenoidal field that serves the Inner Detector. The performance of the toroids in terms of bending power is characterized by the field integral $\int Bdl$, where B is the field component normal to the muon direction and the integral is computed along an infinite momentum muon trajectory, between the innermost and outermost muon-chamber planes. The barrel toroid provides 1.5 to 5.5 Tm of bending power in the pseudorapidity range $0 < |\eta| < 1.4$, and the end-cap toroids approximately 1 to 7.5 Tm in the region $1.6 < |\eta| < 2.7$. The bending power is lower in the transition regions where the two magnets overlap ($1.4 < |\eta| < 1.6$).

Finally, ATLAS includes a three-level trigger system for evaluating and recording only the most interesting events during a run. The trigger is configurable at every level to provide a constant stream of data under any beam conditions.

In the following the various systems composing the detector will be described in detail.

2.2.1 The Inner Detector

The Inner Detector is the innermost system of the ATLAS detector. Its schematic view is shown in Figure 2.5. It is composed by three subdetectors: two silicon detectors, the Pixel Detector and the SCT, and the TRT. It is immersed in an axial magnetic field of 2 T and its overall dimensions are 2.1 m in diameter and 6.2 m in length.

The Inner Detector measures tracks from the passage of the charged particles. So it measures charged particles position and, being immersed in a magnetic field, also their p_{T} and charge.

A detailed description of the sub-detectors is given below and a summary of their main characteristics is also reported in Table 2.1.

- **The Pixel Detector**
  The Pixel Detector is the nearest system to the collision point and it is built directly onto the beryllium beam pipe in order to provide the best possible primary and secondary vertex resolution. It is composed by three cylindrical layers in the barrel region (at radii 50.5 mm, 88.5 mm and 122.5 mm) and two end-caps, each consisting of three disks (located at 495 mm, 580 mm and 650 mm from the detector centre). The Pixel Detector provides three precision measurement points for tracks with pseudorapidity $|\eta| < 2.5$ and it has a full coverage in ϕ. The detector structure is made of low-mass carbon fiber and integrates the cooling system, resulting in a total contribution to X_0 of about 3% per layer. Furthermore, all the detector components are designed to sustain a radiation dose of $\sim$ 500 kGy, which is the dose expected during detector life time. The basic elements of the Pixel Detector are the silicon sensor "modules", that are identical for barrel and disks. The 250 μm thick sensors are divided into pixels 50 μm wide and 400 μ m long, with 47232 pixels on each of the 1744 modules. The total number of channels for the whole detector is $\sim$ 80.4 millions for the whole detector.

  The design requirement was to achieve a resolution of 10 μm in the azimuthal direction and 115 μm along the beam direction. At present around 20 μm has been obtained in the azimuthal direction and 130 μm along the beam direction.

- **The SCT Detector**
  The SCT is the second element of the tracking system, going from the beam pipe outwards. It is composed by four cylinders in the barrel region, with radii between 299 mm and 514 mm and a full length of 1492 mm. Each of the two end-caps consists of 9 disks. It provides typically eight strip measurements (four space-points) for particles originating in the beam-interaction region. The detector consists of 4088 modules. The modules in the barrel are made up by two sensors at a 40 mrad stereo angle in order to measure both coordinates. The strips in the barrel have a constant pitch of 80 μm, while in the end-caps the strip direction is radial and of variable pitch.

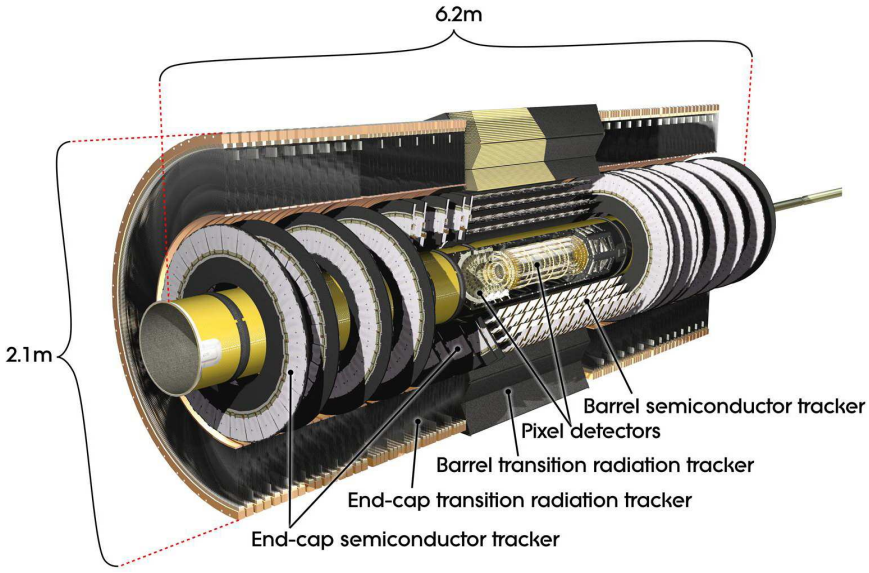

(a)

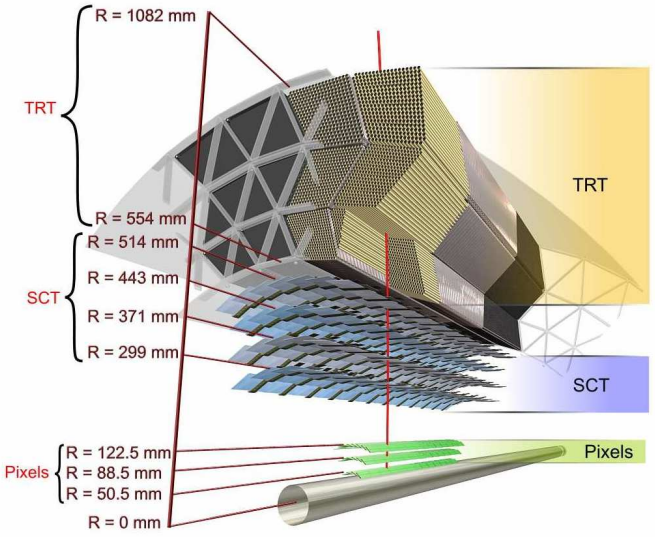

(b)

Figure 2.5: *Schematic views of the ATLAS Inner Detector [35].*

The intrinsic accuracies of the SCT are 17 μm in the azimuthal direction and

580 μm along the beam direction.

- **The TRT Detector**
  The TRT is the outermost system of the Inner Detector and its sensitive volume covers radial distances from 563 mm to 1066 mm. The detector consists of 298 304 proportional drift tubes (straws), 4 mm in diameter, read out by $\sim$ 351000 electronic channels. The straws in the barrel region are arranged in three cylindrical layers and 32 ϕ sectors; they have split anodes and are read out from each side. The straws in the end-cap regions are radially oriented and arranged in 80 wheel-like modular structures. The TRT straw layout is designed so that charged particles with transverse momentum $p_{\mathrm{T}} > 0.5$ GeV and with pseudorapidity $|\eta| < 2.0$ cross typically more than 30 straws.

  The spatial resolution of the TRT is 130 μm in all directions.

  The TRT can also be used for particle identification. Its tubes are interleaved with layers of polypropylene fibres and foils: a charged particle that passes through the boundary region between materials with a different refraction index emits X-ray radiation whose intensity is proportional to the relativistic factor. The TRT works with two threshold levels (defined at the level of the discriminator in the radiation-hard front-end electronics): the ratio of the high threshold hits versus all the hits can be used to identify electrons, as explained in Section 2.3.1.

Subdetector	Radius [cm]	Element size	Spatial resolution [μm]	Hits/track	Readout channels
Pixel	5 - 12	50 μm x 400 μm	10 (R-ϕ) x 115 (z)	3	80 x 106
SCT	30 - 52	80 μm	17 (R-ϕ) x 580 (z)	8	6 x 106
TRT	56 - 107	4 mm	130	30	3.5 x 105

Table 2.1: Summary of the main characteristics of the three ATLAS Inner Detector subdetectors [35]

- **The cooling system**
  For the Pixel Detector and the SCT, a cooling is necessary to reduce the effect of radiation damage to the silicon. They share a cooling system, using C_3F_8 fluid as a coolant. The target temperature for the silicon sensors after irradiation is 0°C for the Pixel Detector and -7°C for the SCT. Since the TRT operates at room temperature, a set of insulators and heaters isolate the silicon detectors from the environment of ATLAS.

For the analysis presented in this thesis the Inner Detector has played a crucial role for primary and secondary vertex identification [82]. A request for a primary vertex with at least 5 tracks is done to reject non collision background (i.e. events that don't come from p-p collisions, but from other sources as, for example, noisy

and dead channels, cosmic muons and beam halo particles). The resolution on the position of the primary vertex in x and z is reported in Figure 2.6, as a function of the number of tracks per vertex N_{tracks}. The tracks are selected asking a p_{T} of at least 400 MeV and to have a minimal number of hits in the Pixel and the SCT subdetectors. As expected the error decreases with increasing numbers of N_{tracks}. A resolution of ~ 100 μm is achieved for 5 tracks. The resolution significantly improve for higher energy tracks as can be seen in Figure 2.7. For vertexes reconstructed with tracks with $\sqrt{\sum p_T^2}$ (where p_{T} is the transverse momentum of each track used in the vertex fit) of 10 GeV, $\sim$ 10-20 (50) μm resolution is achieved in the x (z) direction. Moreover, thanks to good performances on position determination, secondary vertexes are identified. This capability has been very important for the analyses presented in this thesis, since it is the signature of b-quark originated jets. Furthermore, tracks reconstruction is fundamental for electrons and muons identification and measurement, as described in Sections 2.3.1 and 2.3.2. Details on the tracking algorithms used in ATLAS are not discussed in this thesis, but they can be found in [83]. Finally, from the transition radiation of the TRT, it is possible to discriminate electrons from heavier particles.

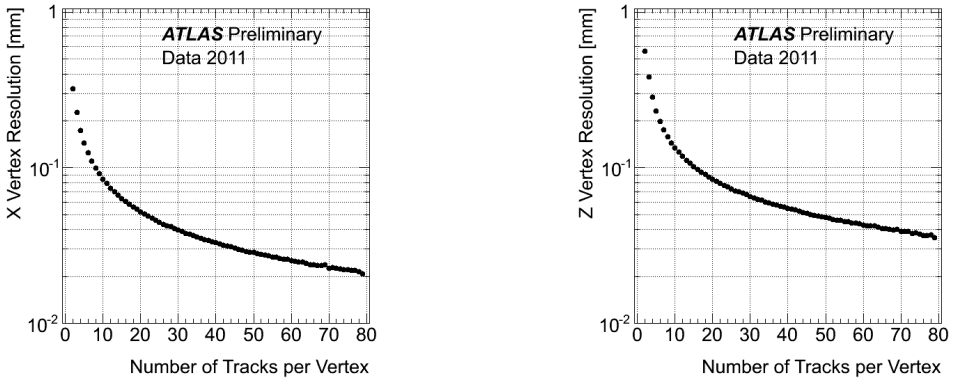

(a) (b)

Figure 2.6: *Estimated vertex resolution σ_X (a) and σ_Z (b) in 7 collision TeV data of 2011 as a function of the number of tracks per vertex [82].*

2.2.2 The Calorimeters

The calorimeter system includes both the EM Calorimeter and the Had Calorimeter. The first is dedicated to the measurement of electrons and photons, the latter to the measurement of hadrons. These calorimeters cover the range $|\eta| < 4.9$, using different techniques suited to the widely varying requirements of the physics processes of interest and of the radiation environment over this large η-range. A schematic view of the calorimeter system is shown in Figure 2.8

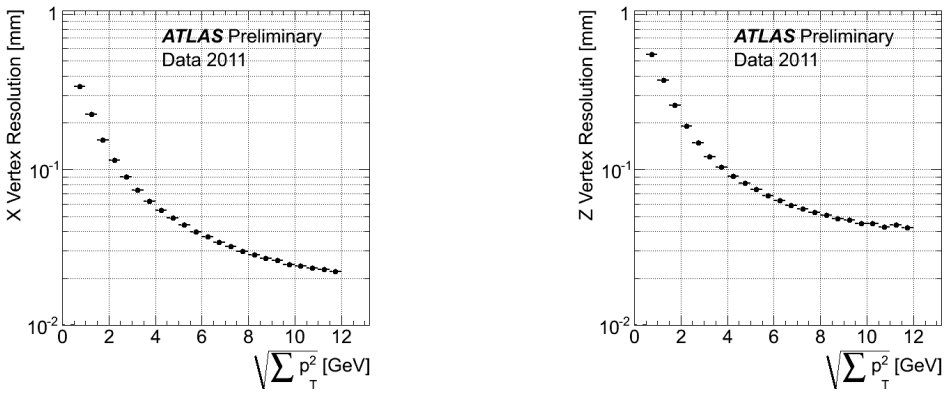

(a) (b)

Figure 2.7: *Estimated vertex resolution σ_X (a) and σ_Y (b) in $\sqrt{s} = 7$ TeV data of 2011 as a function of $\sqrt{\sum p_T^2}$, where p_T is the transverse momentum of each track used in the vertex fit [82].*

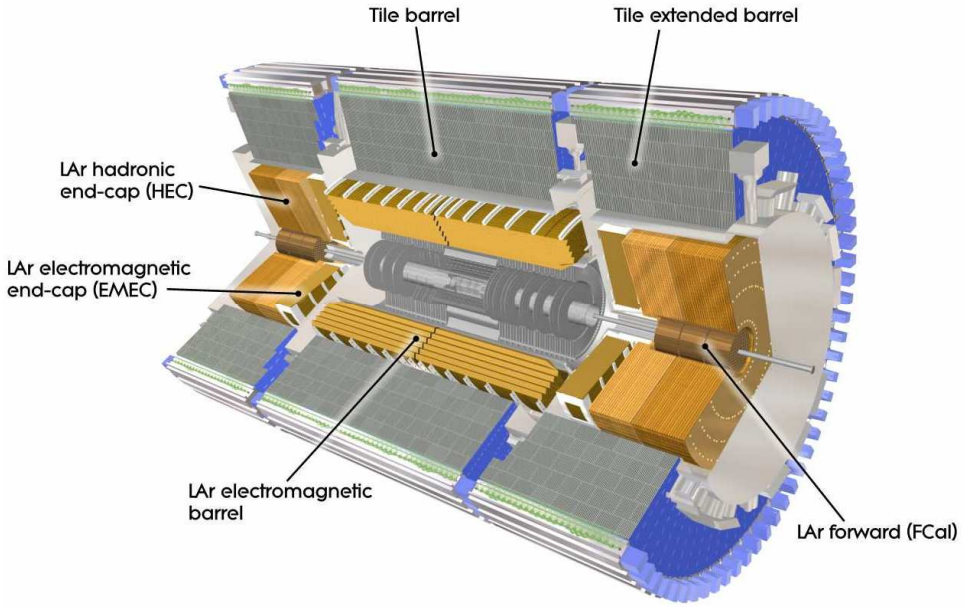

Figure 2.8: *Schematic view of the ATLAS Calorimetric system [35].*

The main purpose of the calorimeters is to measure the energy of the particles and their position. One of the most important requirements for calorimeters is to provide good containment for electromagnetic and hadronic showers: the number of jets reaching the muon system (*punch-through*) has to be limited in order to have a good muon identification. Therefore, calorimeter depth is an important consideration. The total thickness of the EM calorimeter is more than 22 radiation lengths (X_0) in the barrel and more than 24 X_0 in the end-caps. It contains electrons and photons showers up to ~ 1 TeV and it also absorbs almost 2/3 of a typical hadronic shower. The approximate 9.7 (10) interaction lengths (λ) of active calorimeter (EM + Had) in the barrel (end-caps) are adequate to provide good resolution for high-energy jets. The total thickness, including 1.3 λ from the outer support, is 11 λ at $\eta = 0$ and has been shown both by measurements and simulations to be sufficient to reduce punch-through well below the irreducible level of prompt or decay muons.

Some details on the different calorimeter regions are given below.

- **The EM Calorimeters**
  The EM calorimeter is a lead liquid Argon (LAr) detector [84]. To ensure the maximum azimuthal coverage the EM Calorimeter was designed with an accordion geometry, as shown in Figure 2.9: the readout electrodes and the lead absorbers are laid out radially and folded so that particles can not cross the calorimeter without being detected. It is divided into one barrel part ($|\eta| < 1.475$) and two end-caps ($1.375 < |\eta| < 3.2$), each one with its own cryostat. The position of the central solenoid in front of the EM calorimeter demands optimisation of the material in order to achieve the desired calorimeter performance. As a consequence, the central solenoid and the LAr calorimeter share a common vacuum vessel, thereby eliminating two vacuum walls. The barrel calorimeter consists of two identical half-barrels, separated by a small gap (4 mm) at z = 0. Each endcap calorimeter is mechanically divided into two coaxial wheels: an inner wheel covering the region $1.375 < |\eta| < 2.5$, and an outer wheel covering the region $2.5 < |\eta| < 3.2$.

  Over the region devoted to precision physics ($|\eta| < 2.5$), the EM calorimeter is segmented into three longitudinal sections: strips, middle and back. While most of the energy of electrons and photons is collected in the middle, the fine granularity of the strips is necessary to improve the $\gamma - \pi^0$ discrimination and the back measures the tails of highly energetic electromagnetic showers, and helps to distinguish electromagnetic and hadronic deposits. For the end-cap inner wheel, the calorimeter is segmented in two longitudinal sections and has a coarser lateral granularity than for the rest of the acceptance.

  Because most of the central calorimetry sits behind the cryostat, the solenoid, and the 1-4 radiation-lengths thick Inner Detector, EM showers begin to develop well before they are measured in the calorimeter. In order to measure and correct for these losses, up to $|\eta| = 1.8$ there is an additional presampler layer in front of the sampling portion (i.e. accordion) of the calorimetry. The

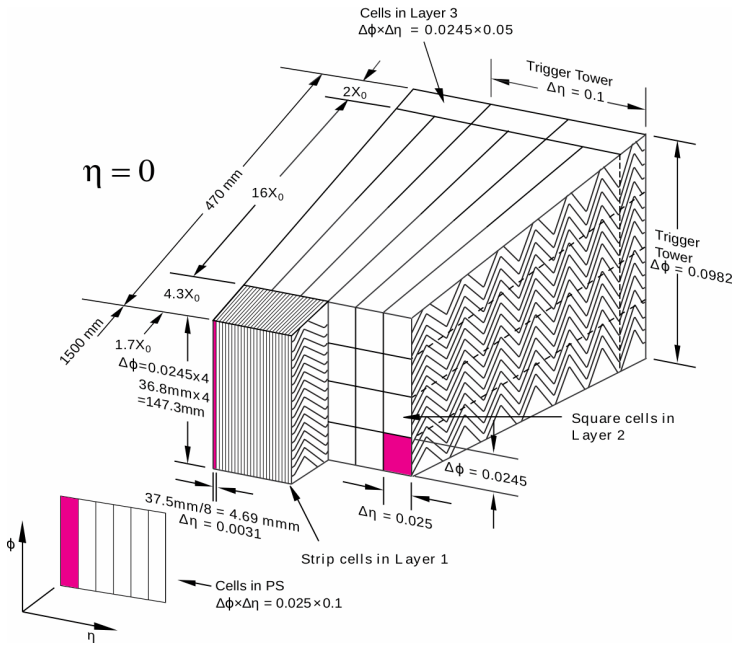

Figure 2.9: *Schematic view of the accordion geometry [35].*

presampler is 11 mm (5 mm) thick in the barrel (end-cap) and includes fine segmentation in η. Unlike the rest of the calorimetry, the presampler has no absorber layer. In practice, it behaves almost like a single-layer LAr tracker.

The transition region between the barrel and the end-cap EM calorimeters, $1.37 < |\eta| < 1.52$, is expected to have poorer performance because of the higher amount of passive material in front of the calorimeter, this region is often referred as crack region.

- **The Had Calorimeters**
  The Had Calorimeter is realized with a variety of techniques depending on the region: central, end-cap and forward.

  In the central region there is the Tile Calorimeter (Tile) [85], which is placed directly outside the EM Calorimeter envelope. The Tile is a sampling calorimeter which uses steel as absorber and scintillating tiles as active material. It is divided into a barrel ($|\eta| < 1.0$) and two extended barrels ($0.8 < |\eta| < 1.7$). Radially, the Tile goes from an inner radius of 2.28 m to an outer radius of 4.25 m. It is longitudinally segmented in three layers approximately 1.5, 4.1 and 1.8 interaction lengths thick for the barrel and 1.5, 2.6, and 3.3 interaction length for the extended barrel.

  The Hadronic End-cap Calorimeter (HEC) consists of two independent wheels per end-cap, located directly behind the end-cap EM calorimeter and sharing the same LAr cryostats. It covers the region $1.5 < |\eta| < 3.1$, overlapping

both with the Tiles and the Forward Calorimeter. The HEC uses the LAr technology. Each wheel is divided into two longitudinal segments, for a total of four layers per end-cap. The wheels closest to the interaction point are built from 25 mm parallel copper plates, while those further away use 50 mm copper plates. The outer radius of the copper plates is 2.03 m, while the inner radius is 0.475 m (except in the overlap region with the forward calorimeter where this radius becomes 0.372 m). The copper plates are interleaved with 8.5 mm LAr gaps, providing the active medium for this sampling calorimeter.

- **The Forward Calorimeters**
  The Forward Calorimeter (FCal) covers the $3.1 < |\eta| < 4.9$ region and is another LAr based detector. It is integrated into the end-cap cryostats, it is approximately 10 interaction lengths deep and consists of three 45 cm thick independent modules in each end-cap: the absorber of the first module is copper, which is optimised for electromagnetic measurements, while for other two is tungsten, which is used to measure predominantly the energy of hadronic interactions. The region where the FCal is set is very close to the beam pipe, so the expected radiation dose is very high. Therefore the electrode structure is different from the accordion geometry, consisting in a structure of concentric rods and tubes parallel to the beam axis. The LAr in the gap between the rod and the tube is the sensitive medium.

The LAr electronic calibration is done using pulse height samples, while the tiles signal is monitored in different ways. Cesium sources, which can scan across the detector, have been installed to check its response (the ratio of the reconstructed signal to the "true" signal). Charge can be injected into a single cell to test and calibrate the read-out electronics and finally lasers can provide light to test the optical connections and photomultiplier tubes response.

The ATLAS calorimetry is non-compensating, meaning that a hadron will deposit a smaller fraction of its energy in the active portion of the calorimeter, on average, than an electron or photon will. The difference must be taken into account by an additional correction applied to hadronic objects. There are several ways to select hadronic objects and correct their energy. This various calibration strategies will be discussed in Section 2.3.3.

The performance of the calorimeter system is summarized in Table 2.2.

In the analyses presented in this thesis, calorimeter system has played a crucial role for the reconstruction of electrons, jets and $\not\!\!E_T$, as shown in Section 2.3.

2.2.3 The Muon Spectrometer

The layout of the Muon Spectrometer is shown in Figure 2.10. The muon system has two different functions: it is needed for high precision tracking of muons and also for triggering on them. Muons frequently indicate an interesting event, and, therefore, a muon-based trigger is useful for selecting some new physics signals. On the other

Detector component	Required resolution (σ_E/E)	η coverage
EM calorimetry	$10\%\sqrt{E} \oplus 0.7\%$	± 3.2 ($\pm$ 2.5 for the trigger)
Had calorimetry		
barrel and end-cap	$50\%\sqrt{E} \oplus 3\%$	± 3.2
forward	$100\%\sqrt{E} \oplus 3.1\%$	± 4.9

Table 2.2: Nominal detector performance goals and coverage for the ATLAS detector [35].

hand, in order to precisely measure the decays of new particles, it is necessary to make accurate measurements of each muon's momentum.

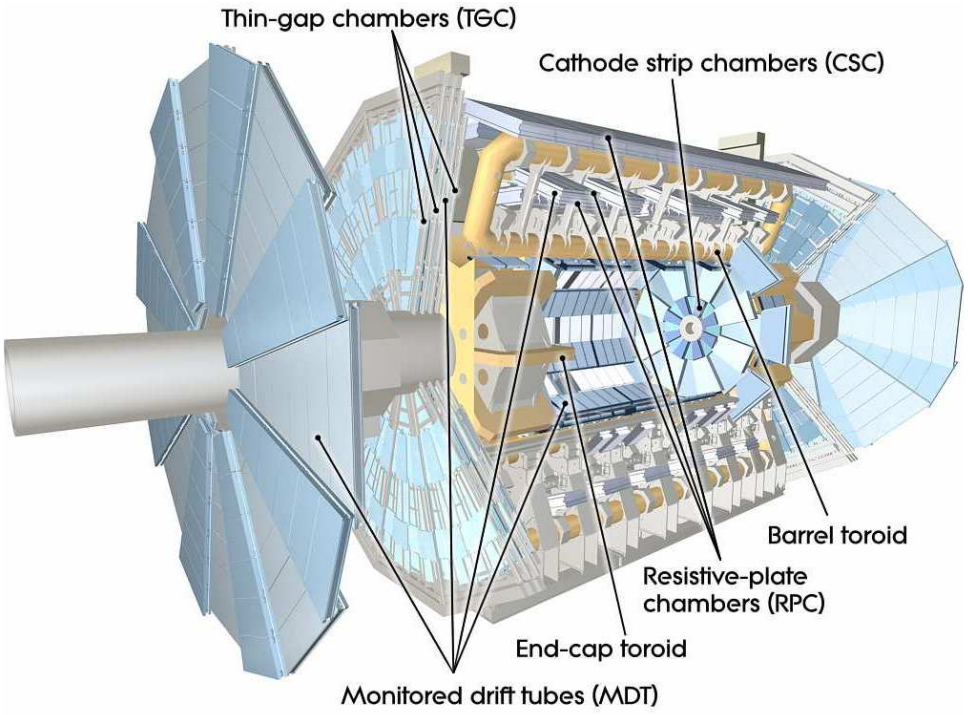

Figure 2.10: *Schematic view of the ATLAS Muon Spectrometer [35].*

The momentum measurement is based on the magnetic deflection of muon tracks. Such a large volume magnetic field, which is necessary to bend the particle trajectories, is provided by the large barrel toroid in the region $|\eta| < 1.4$, by two smaller end-cap magnets in the $1.6 < |\eta| < 2.7$ region and by a combination of the two in the transition region ($1.4 < |\eta| < 1.6$). This magnet configuration provides a field which is mostly orthogonal to the muon trajectories, while minimising the degradation of the resolution due to multiple scattering. Because the toroidal magnet system of the

Muon Spectrometer is completely independent of the solenoid in the Inner Detector, ATLAS is able to acquire two independent measurements of a muons momentum. The measurement is performed over most of the η-range by the Monitored Drift Tubes (MDT). At large pseudorapidities and close to the interaction point, Cathode Strip Chambers (CSC) with higher granularity are used: they have been designed to withstand the demanding rate and background conditions. The stringent requirements on the relative alignment of the muon chamber layers are obtained by the combination of precision mechanical-assembly techniques and optical alignment systems both within and between muon chambers.

Concerning the triggering function of the muon system, it covers the pseudorapidity range $|\eta| < 2.4$. Resistive Plate Chambers (RPC) are used in the barrel and Thin Gap Chambers (TGC) in the end-cap regions. The trigger chambers for the Muon Spectrometer serve a three-fold purpose: to provide the bunch-crossing identification, to provide a well-defined transverse momentum thresholds and to measure the muon coordinate in the direction orthogonal to that determined by the precision-tracking chambers. The barrel chambers are positioned on three cylinders concentric with the beam axis, at radii of about 5, 7.5, and 10 m. They cover the pseudorapidity range $|\eta| < 1$. The end-cap chambers cover the range $1 < |\eta| < 2.4$ and are arranged in four disks at distances of 7, 10, 14, and 21-23 m from the interaction point, concentric with the beam axis.

The reconstruction efficiency and resolution of the Muon Spectrometer were measured using cosmic ray events in 2008 and 2009 [86]. The reconstruction efficiency, integrated over the detector acceptance, is $\sim$ 94%. At $|\eta| = 0$ there is a gap in the detector for cable routing. If the region of the detector near this crack is excluded, the reconstruction efficiency is increased to 97%. The transverse momentum resolution was determined from this data to be

$$\frac{\sigma_{p_T}}{p_T} = frac0.29GeVp_T \oplus 0.043 \oplus 4.1 \times 10^{-4}GeV^{-1} \times p_T \tag{2.2}$$

for transverse momentum (p_T) between 5 and 400 GeV. The commissioning of the Muon Spectrometer has been continued with collision data and the performance of muon reconstruction is discussed in Section 2.3.2.

2.2.4 Forward detectors

One measurement which is very important for almost every physics analysis is the luminosity measurement [87]. As it is a fundamental quantity, three different detectors help in its determination. At $\pm$17 m from the interaction region there is the LUminosity measurement using Cerenkov Integrating Detector (LUCID) [88]. It detects inelastic pp scattering in the forward direction and it is the main online relative-luminosity monitor for ATLAS. It is also used, before collisions are delivered by the LHC, to check the beam losses. For the beam monitoring, also another detector has been inserted: the Beam condition Monitor (BCM).

The other detector used for luminosity measurement is called Absolute Luminosity For ATLAS (ALFA) [89]. It is located at ±240 m from the interaction point. It consists of scintillating fibre trackers located inside Roman pots which are designed to approach as close as 1 mm from the beam.

The last detector is Zero-Degree Calorimeter (ZDC) [89]. It is located at ±140 m from the interaction point, just beyond the point where the common straight-section vacuum-pipe divides back into two independent beam-pipes. The ZDC modules consist of layers of alternating quartz rods and tungsten plates which measure neutral particles at pseudorapidities $|\eta| \geq 8.2$.

2.2.5 Trigger

At present (2011), protons collide in ATLAS every 50 ns. This correspond to LHC luminosities $> 10\%$ of the design value. Some 100 million channels in the ATLAS detector must be read out by the data acquisition software during the LHC operation, resulting in ~ 1.5 MB events. Without any filtering, ATLAS would need to process and record ~ 60 terabytes of data every second, currently an impossible task. This is not a dramatic limitation, since interesting physics occurs mostly at rates of 10, 1 or < 0.1 Hz and so we are actually interested in a tiny fraction of the events produced. This is however a challenging task. Because only a small fraction of the events can be recorded, these events must be quickly searched for interesting signatures. A rapid decision must be made for each event. But rejected events are, of course, lost forever.

The ATLAS trigger system [90] is designed to record events at a rate of about 200 Hz, with a reduction of more than 5 orders of magnitude with respect to the collision rate.

ATLAS has implemented a three-level trigger system to handle the high-rate environment. At each level, physics objects are reconstructed with improved granularity and precision and over a larger fraction of the detector, culminating in complete event reconstruction in the final trigger stage. The first level (Level1 or L1) trigger is a configurable, pure-hardware trigger that is designed to make a decision on each event in under 2.5 μs and provide output at a rate up to 75 kHz. It makes an initial decision based on the timing from an electrostatic beam pick-up (BPTX), the coarse detector information from muon trigger chambers and towers of calorimeter cells, together with the multiplicity information from the Minimum Bias Trigger Scintillators (MBTS) and very forward detectors. The L1 provides regions of interest (RoIs) to the following level. The second level (Level2 or L2) triggers make a decision in under than 40 ms and provide output at rates up to 3.5 kHz. The L2 triggers run a simplified version of the event reconstruction in the regions of interest defined by the calorimeter and muon systems. Improved selection criteria, such as distinguishing electrons from photons by track matching, and improved calibrations are applied. In the level-three trigger, called the "event filter" (EF), the complete offline event reconstruction makes a decision in under 4 s and provides output at

200-400 Hz. The L2 and EF are both software triggers, unlike the L1 trigger, and they are together referred to as the "high-level trigger" (HLT). One L1 item may seed many HLT triggers, and many L1 items may seed a single HLT trigger. A full sequence of triggers from L1 through the EF is called a trigger "chain".

A "menu" of possible trigger items is prepared for each data taking run. The menu defines a complete list of what trigger items will be evaluated, what values the parameters of those items will take, and how the lower-level trigger items map into higher-level triggers. Some items are run unprescaled, meaning that any time an event is accepted by the trigger it will be passed on to the next level (or written out in the case of the EF). Others, in particular low-p_{T} triggers, may be run with relatively high prescales, so that only some of the events which pass the trigger are accepted. Any of the HLT triggers can be run in pass-through mode, in which no events are rejected but each event is evaluated nonetheless. This feature has been particularly useful during the initial trigger commissioning and will be used also for new trigger items. Because of the strict timing demands, if an event cannot be evaluated in the allotted time for each trigger stage, it is passed and flagged for a later examination.

After the EF, the events are divided into "streams", each containing the output from several different trigger chains. These streams are transferred to the Tier0, where the full offline event reconstruction is run, and the output is saved for distribution to computing centers around the world. Streams called the "express stream" and "calibration stream" contain an assortment of events which are deemed interesting or useful for calibration of the subdetectors. They are processed first in order to provide new calibrations to the detectors within 24-hour periods.

All the details about the trigger streams and chains used in my work are described in Section 3.2.2 for the top quark pair cross section measurement and in Section 4.2.2 for the top charge asymmetry one.

2.3 Object reconstruction in ATLAS

The analysis described in this thesis relate to physics processes with a top quark pair decaying semileptonically. The selection of this kind of events relies on the reconstruction and identification of electrons, muons, jets and b-jets. Furthermore they are characterized by the presence of neutrinos, which don't interact in the detector. Their energy can be nevertheless reconstructed as the difference between the initial state and the final state total momentum. In hadron colliders, such as the LHC, the initial momentum of the colliding partons along the beam axis is not known a priori, so the amount of total missing energy cannot be determined. However, the initial momentum transverse to the beam axis is zero, so the missing energy can be measured in the transverse plane (*missing transverse energy* $\not\!\!E_T$).

In the following, general reconstruction and identification algorithms used in ATLAS are described. Selection cuts used in my specific studies are discussed in

Section 3.2.1 and Section 4.2.1 for the analysis on 2010 and 2011 data respectively.

2.3.1 Electrons

The electron reconstruction and identification algorithms are designed to achieve both a large background rejection and a high and uniform efficiency for isolated electrons over the full acceptance of the detector and with transverse energies above 20 GeV. These electrons need to be separated from hadrons in QCD jets and from secondary electrons originating mostly from photon conversions in the tracker material. The electron reconstruction begins with the creation of a preliminary set of clusters in the EM Calorimeter, using a sliding window algorithm [91]. These seed clusters have a fixed size, 3×5 cells in $\eta\times\phi$, and they must have an energy of at least 2.5 GeV. For each reconstructed cluster, the reconstruction algorithm tries to find a matching track, within a $\Delta\eta \times \Delta\phi$ range, with respect to the cluster barycenter in the middle calorimeter layer. The cluster energy is determined by computing and summing four different contributions: the energy deposited in the calorimeter inside the cluster, the one deposited in the material in front of the EM Calorimeter, the one deposited outside the cluster (lateral leakage) and finally the energy deposited beyond the EM Calorimeter (longitudinal leakage). The corrections applied to the measured cluster energy are based on precise Monte Carlo simulations validated by comprehensive measurements with 900 GeV data [92]. The four terms are parametrized as a function of the cluster measured signals in the presampler (where present) and in the three accordion longitudinal layers. The parameters are computed at each pseudorapidity value corresponding to the centre of a middle cell and stored in a database [93].

The baseline ATLAS electron identification algorithm relies on variables which deliver good separation between isolated electrons and fake signatures from QCD jets. These variables include information from the calorimeter, the tracker and the matching between tracker and calorimeter. Three reference set of cuts have been defined for electrons (loose, medium, tight):

- *Loose cuts*: This set of cuts performs a simple electron identification based only on limited information from the calorimeters. Cuts are applied on the hadronic leakage and on shower-shape variables, derived from the middle layer of the EM Calorimeter only. This set of cuts provides excellent identification efficiency, but poor background rejection.

- *Medium cuts*: This set of cuts improves the background rejection quality, by adding cuts on the energy deposits in strips in the first layer of the EM Calorimeter and on the tracking variables. Strip-based cuts are adequate for e - π^0 separation. The tracking variables include the number of hits in the pixels, the number of silicon hits (pixels plus SCT) and the transverse impact parameter. The medium cuts increase the jet rejection by a factor of 6 with respect to the loose cuts, while reducing the identification efficiency by $\simeq 4\%$.

- *Tight cuts*: This set of cuts makes use of all the particle identification tools currently available for the electrons. In addition to the criteria used in the medium identification, cuts are applied:
  - on the number of hits in the first pixel layer (to reject electrons from conversions),
  - on the number of hits in the TRT,
  - on the ratio of high-threshold hits to the number of hits in the TRT (to reject the dominant background from charged hadrons),
  - on the difference between the cluster and the extrapolated track positions in η and ϕ,
  - on the ratio of the cluster energy to the track momentum ratio.

  The jet rejection is $\simeq 10^5$, while the identification efficiency is $\simeq 70\%$.

In the analysis described in this thesis the electron selection has been based on tight cuts, in order to achieve the best rejection of QDC di-jet background.

Since the beginning of the data-taking many studies have been done on the electron identification performance. The agreement of the Monte Carlo with the data is found to be good.

At the beginning of data taking electron reconstruction performance was studied using electrons from J/Ψ meson decay. The invariant mass of this meson was reconstructed despite the challenges introduced by the low p_{T} of the electrons, for which ATLAS is not optimised. Then the electrons from the Z boson decay have been studied and used for calibrations. Figure 2.11 shows the J/Ψ invariant mass in the top plot and the Z invariant mass in the bottom plot.

2.3.2 Muons

Muon reconstruction is based on the information from Muon Spectrometer, Inner Detector and calorimeters. Different kinds of muon candidates are built, depending on how the detector information is used in reconstruction.

- *Stand-alone muons*: The hits from Muon Spectrometer are combined into segments to form a track. The muon momentum is measured using this track and then it is corrected for the parametrized muon energy loss in the calorimeter, to obtain its momentum at the interaction point. The track is extrapolated back to the beam axis to obtain the muon η and ϕ coordinates and its impact parameter with respect to the interaction point.

- *Combined muons*: Stand-alone muons are combined with an Inner Detector track. The muon parameters are derived from a combined track fit to the hits in the two sub-detectors.

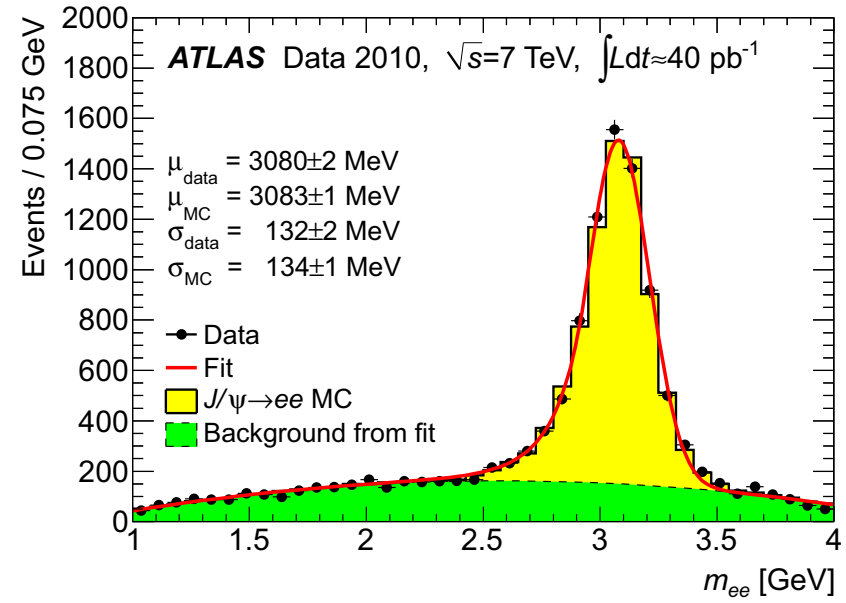

(a)

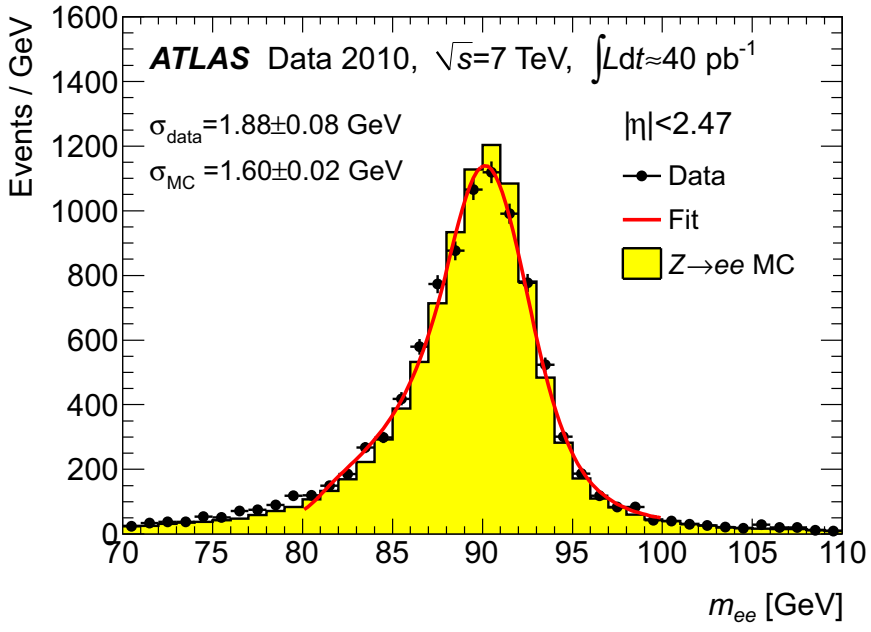

(b)

Figure 2.11: *(a) Invariant mass of J/Ψ meson, measured with an integrated luminosity of 39 pb^{-1} [94]; (b) Invariant Z mass for electron pairs with an integrated luminosity of 39 pb^{-1} [95].*

- *Segment tagged muons*: An Inner Detector track is used as a seed. The re-

construction algorithms then search for track segments in the precision muon chambers that can be associated to the Inner Detector track extrapolated to the Muon Spectrometer.

- *Calorimeter tagged muons*: They are built starting from an Inner Detector track. The track is identified as a muon if energy depositions compatible with the minimum ionising particle hypothesis can be associated to it.

In the two analysis, described in this thesis, only combined muons are selected.

In the early data analysis ATLAS uses two different chains to evaluate the muon performance in detail, STACO [96] and MuId [97]. These chains correspond to different sets of algorithms that build the classes of candidates listed above. Both muon combination algorithms create combined tracks out of pairs of Muon-only and Inner-Detector-only tracks. To do this, a χ^2 match is used and corrections are made for energy losses in the calorimeter, however the two algorithms handle the combined track in a slightly different way:

- STACO does a statistical combination of the track vectors to obtain the combined track vector,
- MuId re-fits the combined track, starting from the Inner Detector track and then adding Muon Spectrometer measures.

The two algorithm have shown very similar performances and can be both used for the analysis. In this thesis the MuId algorithm has been applied.

The muon reconstruction performance was studied first of all in minimum bias events, just comparing basic reconstruction quantities with the Monte Carlo simulation [98], and later on using muons coming from J/Ψ and Z decays. Detector efficiencies, hit multiplicities, muon isolation, and residual distributions of reconstructed muon tracks were measured and found to be well reproduced by the Monte Carlo simulation. The capability of the ATLAS detector to reconstruct muons on a wide p_{T} range is illustrated in Figure 3.1, where the di-muon spectrum is shown. Resonances down to J/Ψ and up to Z are evident.

2.3.3 Jets

Hadronic particles in ATLAS deposit their energies mainly in the calorimeter system. In an attempt to resolve particles coming from the hard scatter, these energy deposits may be grouped into objects called *jets*.

In the following jet reconstruction techniques are briefly described.

Jet input objects

As described in Section 2.2.2, the ATLAS calorimeters have a high granularity (about 187000 cells independently read-out) and a high particle stopping power

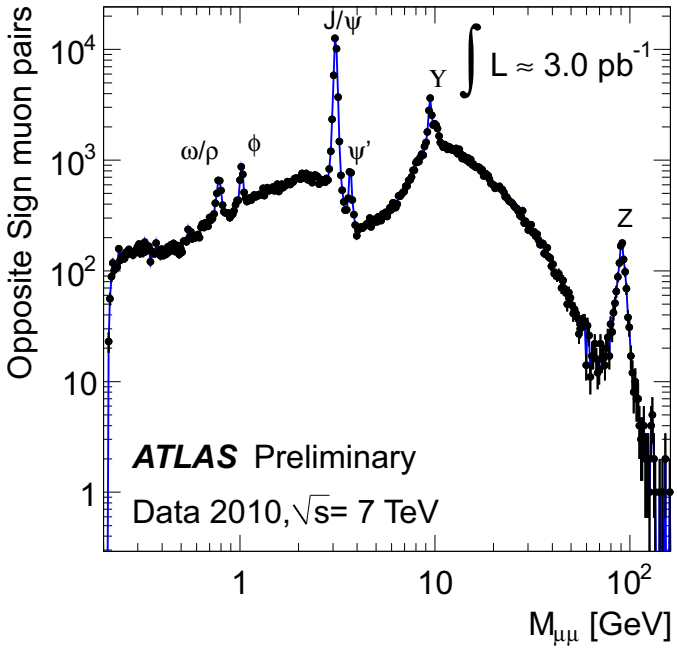

Figure 2.12: *Di-muon invariant mass spectrum for data, from combined opposite sign muons [99]. Peaks corresponding to various resonances are evident.*

over the whole detector acceptance ($|\eta| < 4.9$). This calorimeter features allow a high quality jet reconstruction in the challenging environment of the proton-proton collisions at the LHC.

Cells provide many information: energy, time, quality, and gain. They are primarily set at the so-called "electromagnetic scale", as it has been determined by electron test beams and simulations. This energy scale accounts correctly for the energy of electrons and photons, but it underestimates hadron energy, because the ATLAS calorimeters are not compensating. As a consequence electromagnetic showers generate larger signal than hadrons depositing the same energy and therefore a specific correction for the hadronic signals is needed.

It's not very convenient to use the individual cell signals, because they can be negative, due to noise effects, and because it is difficult to determine the source of the signal without signals from neighbours. The cells have thus to be collected into larger objects.

The jets used for the analyses presented in this thesis have been built from topological clusters (topoclusters). Topoclusters are basically an attempt to reconstruct three-dimensional energy deposits from the showers developing for each particle entering the calorimeter. The clustering starts with seed cells with a signal-to-noise ratio $\Gamma = E_{cell}/\sigma_{noise,cell}$ above 4. Then topological clusters are built by iteratively adding neighboring cells with $|\Gamma| > 2$. Finally, a ring of guard cells, with signal significances above a basic threshold $|\Gamma| > P = 0$, is added to the cluster. A schematic

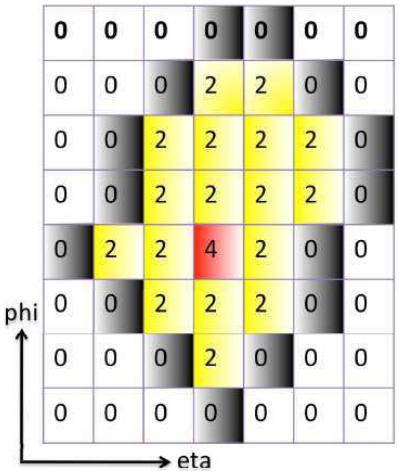

Figure 2.13: *Topocluster schematic representation.*

representation of a topocluster is shown in Figure 2.13. After the initial clusters are formed, they are analysed for local signal maximums by a splitting algorithm. If more than one maximum is found, the cluster is split.

Jet algorithms

The mapping from partons to jets is a complex problem and it depends strongly on the used jet algorithm. Many solutions have been used or proposed for defining jets. An important common feature is that, in ATLAS reconstruction software framework ATHENA, the same jet finder code can be run on objects like topoclusters, reconstructed tracks, and generated particles and partons.

The algorithm adopted by the ATLAS collaboration has default is the anti-k_t [100]. This belongs to the category of Cluster Algorithms which are based upon pair-wise clustering of the initial constituents. The algorithms define a distance measure between objects and also some condition upon which clustering should be terminated. Two distances are introduced: d_{ij} between entities (particles, pseudo-jets) i and j and d_{iB} between entity i and the beam (B). The clustering proceeds by identifying the smallest distance:

- if it is a d_{ij}, i and j are combined in a single jet,
- if it is d_{iB}, i is considered as a single jet and it is removed from the list of entries.

The distances are recalculated and the procedure repeated until no entities are left.

The quantities d_{ij} and d_{iB} are defined as follows:

$$d_{ij} = min(k_{ti}^{2p}, k_{tj}^{2p}) \frac{\Delta R_{ij}^2}{R^2} \tag{2.3}$$

$$d_{iB} = k_{ti}^{2p} \tag{2.4}$$

where

$$(\Delta R)_{ij}^2 = (y_i - y_j)^2 + (\phi_i - \phi_j)^2 \tag{2.5}$$

and k_{ti}, y_i and ϕ_i are the transverse momentum, the rapidity and the azimuth of particle i. In addition to the radius parameter R, the parameter p governs the relative power of the energy scale versus geometrical (R_{ij}) one. For large values of R, the d_{ij} are smaller, and thus more merging takes place before jets are complete. On the other hand the p parameter causes a preferred ordering of clustering: if the sign of p is positive clusters with lower energy will be merged first, if it's negative the clustering will start from higher energy clusters.

The anti-k_t algorithm p is set to -1 in Equation 2.3. This means that objects with high relative momentum k_T are merged first. As a consequence this algorithm has low sensitivity to soft radiation and jet area is very regular, as shown in Figure 2.14. This feature can be useful in order to estimate the contribution coming from the underlaying event.

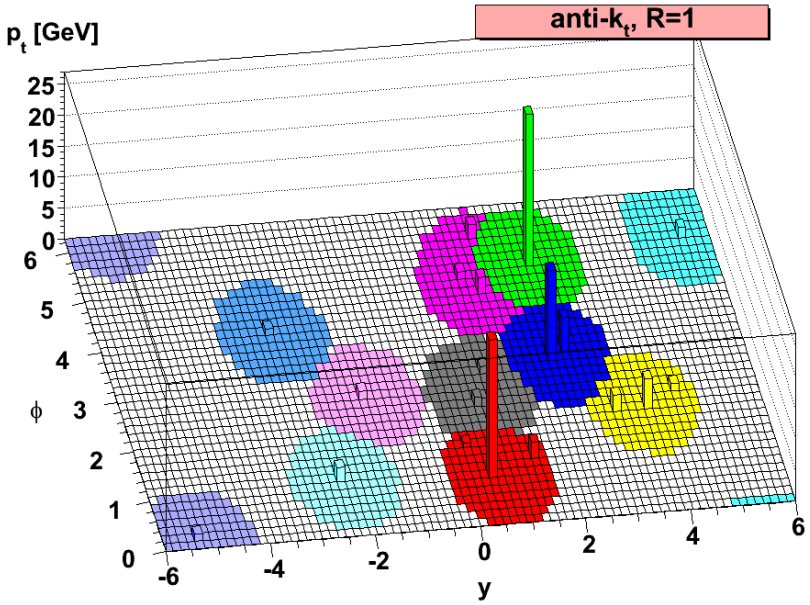

Figure 2.14: *A sample parton-level event (generated with* HERWIG *), clustered with anti-k_t algorithm. Areas of the resulting hard jets are shown [101].*

The choice of R parameter is analysis dependent: the typical default values used in ATLAS are R = 0.4 and R = 0.6. For top quark pair events, characterized by many jets in the final state, a smaller cone size is more suitable, so R = 0.4 has been chosen.

Jet calibration

The ATLAS calorimeters are not compensating, so the energy of hadronic particles is underestimated. In order to reconstruct the energy of the jets, a calibration procedure is needed.

ATLAS has developed several calibration schemes with different levels of complexity.

- *Simple p_{T} and η-dependent calibration scheme (EMJES calibration)*: The goal of the Jet Energy Scale calibration, here called EMJES because it is applied on top of the EM scale, is to correct the energy and momentum of jets measured in the calorimeter, using as reference the kinematics of the corresponding Monte Carlo Truth jets. The jet energy scale calibration is derived as a global function depending on p_{T} and η. Systematics are due to dead material and to uncertainties on calorimeters energy scale calculated from test beams, on simulation of the hadron showers in calorimeters and on Monte Carlo event generator description of fragmentation and underlaying event. This calibration technique has been used for both the analyses presented in this thesis, as described in Chapters 3 and 4.

- *Global cell energy density weighting calibration scheme (GCW calibration)*: Electromagnetic deposits in calorimeters are characterized by their compactness and relatively high energy density. The hadronic component produced by the hadrons has a broader energy deposit. The energy density is therefore sensitive to the type of energy deposit: electromagnetic or hadronic. The GCW calibration method exploit this sensitivity to assign to each cell a correction weight based on its energy density.

  The reconstructed jet energy is then defined as:

  $$E_{recoJets} = \sum_{i=cells} w_i(\rho) \cdot E_i \tag{2.6}$$

  The weights w_i are obtained minimizing the difference between E(reco jet) and the reference jet energy.

- *Local Hadron Calibration (LCW calibration):* The input for this calibration procedure are topological clusters. The clustering of the energy deposit in calorimeters allows to make a relatively good matching between clusters and stable particles in jets. Each cluster can be classified as mainly electromagnetic, hadronic or unknown, according to its shape (classification based on the

predicted shape obtained in simulation). Clusters classified as hadronic receive the appropriate calibration weight, to bring back the measured energy to the "true" energy deposit in calorimeter. Jets are then built from the calibrated clusters (while in the global calibration, jets were built from the uncalibrated clusters). There is still a difference between the calibrated energy and the reference jet energy due in particular to the fact that some particles composing the reference jet might be bent out of the acceptance of the reconstructed jet, or leave an energy which is too low to be included in a cluster. For this reason, additional corrections are requested in order to calibrate the reconstructed jet to the reference jet energy. With respect to the global calibration, where all detector effects are factorized in a unique weighting function, the local calibration proceeds step-by-step, correcting in a separated way the different detector effects (first, the non-compensation, and then the out of cone and the energy loss in dead material).

2.3.4 *b*-jets reconstruction

The aim of *b*-tagging algorithms is to distinguish jets containing *b* flavoured hadrons from light quark jets. For each selected jet they provide *b*-weights reflecting the probability that it originates from a *b*-quark. The discrimination of *b*-jets from light quark jets originates mainly in the relatively long life time of *b* flavoured hadrons, resulting in a significant flight path length L. This leads to measurable secondary vertices and impact parameters of the decay products. The transverse impact parameter d_0 is the distance in the transverse plane (x,y) between the point of closest approach of a track and primary vertex; the longitudinal impact parameter is the z-coordinate of this point. Various *b*-tagging algorithms can be defined, based on these discrimination variables (L, d_0 and z_0), on secondary vertex properties and on the presence of leptons within *b*-jets. In the following, the *b*-tagging algorithm used in this thesis is presented.

The SV0 algorithm is a very simple and a robust *b*-tagger, which doesn't need the a-priori knowledge of the properties of either *b*-jets or light jets.

It is based on the reconstruction of secondary vertices from the tracks within a jet. A track is associated to a jet, if its distance from the jet axis in ΔR is lower than a given threshold. Not all the tracks are considered in the secondary vertex reconstruction, but only the ones that satisfy some quality criteria, such as the number of hits in Pixel and SCT detectors. Furthermore a track is not allowed to be associated to multiple jets, but only to the closest one. Using these tracks as input, the SV0 algorithm starts by reconstructing two-track vertices significantly displaced (in three dimensions) from the primary vertex. The algorithm then removes two-track vertices with a mass consistent with a K^0_s meson, a Λ^0_s baryon or a photon conversion. In addition, two-track vertices at a radius consistent with the radius of one of the three Pixel Detector layers are removed, as these vertices likely originate from material interactions. For each jet, the tracks in surviving two-track vertices

are taken together and fitted to a single secondary vertex. In an iterative process it removes the track with the largest χ^2 contribution to the common vertex until the fit probability of the vertex is greater than 0.001 and the vertex mass is less than 6 GeV. Finally a cut is imposed on the signed decay length significance, $L/\sigma(L)$, of the reconstructed secondary vertex. Where the sign of $L/\sigma(L)$ is given by the one of the projection of the decay length vector on the jet axis. An illustration of a SV0-tagged jet is shown in Figure 2.15.

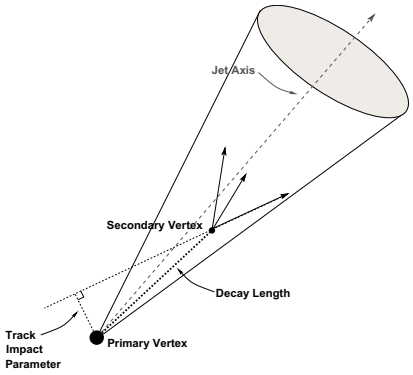

Figure 2.15: *A secondary vertex with a significant decay length indicates the presence of a long-lived particle in the jet. The secondary vertex is reconstructed from tracks with a large impact parameter significance with respect to the primary vertex.*

The full available 2010 statistics, corresponding to an integrated luminosity of 35 pb^{-1}, has been used to calibrate one working point: $\omega_{\mathrm{SV0}} = 5.85$, corresponding to $\epsilon_b = 50\%$ (SV050).

Figure 2.16 shows the efficiency of SV050 tagger as a function of jet p_{T} and jet η. The mistag rate, defined as the fraction of jets originated from light flavour which are tagged by b-tagging algorithm, is shown in Figure 2.17. Light-flavour jets can be mistakenly tagged as b-jets mainly because of the finite resolution of the Inner Detector and the presence of tracks stemming from displaced vertices from long-lived particles or material interactions.

Future analysis will adopt more advanced and higher performance taggers, that need special data driven calibration.

2.3.5 Missing transverse energy

The measurement of $\not{E}_T$ in an event with a top quark pair decaying semileptonically gives the possibility to reconstruct the energy of the neutrino, coming from the leptonic W decay. In the following it will be described how $\not{E}_T$ is reconstructed in ATLAS and it will be explained why it needs to be calibrated and how the calibration is performed. Furthermore, the performance of $\not{E}_T$ reconstruction with $\sqrt{s} = 7$ TeV collision data will be shown.

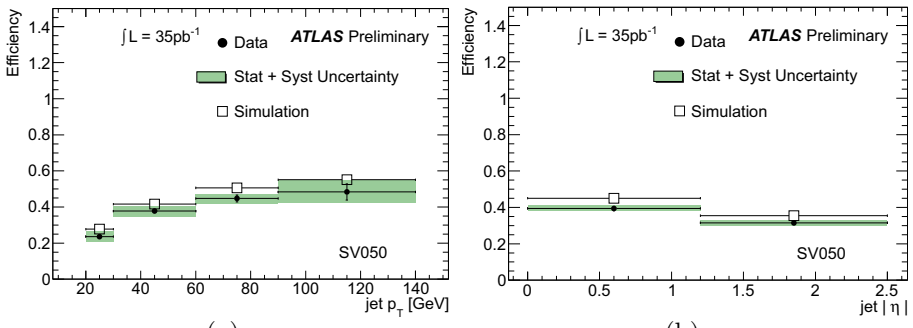

(a) (b)

Figure 2.16: *Expected and observed b-tagging efficiency for the SV050 tagger as a function of jet* p_{T} *(a) and jet* η *(b) [102]. This efficiency is calculated using events characterized by the presence of a jet and an associated reconstructed muon. Jets originated from a b quark are identified with respect to c-jets and light jets using the ratio between the muon* p_{T} *and the total jet* p_{T} *. Muons originated from b-hadrons have indeed an harder spectrum with respect to muons in c- and light-flavour jets.*

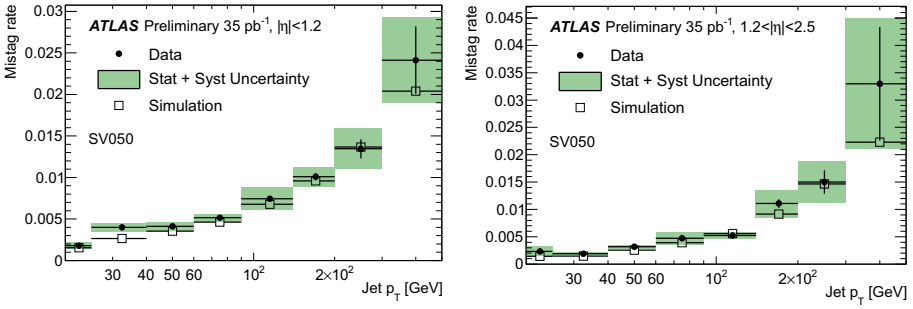

(a) (b)

Figure 2.17: *Expected and observed mistag rates as a function of jet* p_{T} *for central (*$|\eta| < 1.2$*; a) and forward jets (*$1.2 < |\eta| < 2.5$*; b) for the SV050 tagger [102]. Mistag rates are calculated from the negative part of the* S_{d_0} *or* $L/\sigma(L)$ *distributions. Prompt tracks, which are seemingly displaced due the finite resolution of the tracker, will be indeed characterized by symmetric about zero distributions. This tracks, in fact, will as often appear to originate from a point behind as in front of the primary vertex with respect to the jet axis. Proper corrections, accounting for the mistags due to long-lived particles and material interactions, have been applied.*

$\not\!\!E_T$ reconstruction

The $\not\!\!E_T$ reconstruction presently used in ATLAS for physics analysis includes contributions from transverse energy deposits in the calorimeters, corrections for energy loss in the cryostat and measured muons. Its components along the coordinate axes

in the $x - y$ plane therefore are:

$$E_{x(y)}^{\text{miss}} = E_{x(y)}^{\text{miss,calo}} + E_{x(y)}^{\text{miss,cryo}} + E_{x(y)}^{\text{miss},\mu} \tag{2.7}$$

The three terms will now be described in detail.

The $\not\!\!E_T$ calorimeter term: The calorimeter term is defined as:

$$\begin{aligned} E_x^{\text{miss,calo}} &= -\sum_{i=1}^{N_{\text{cell}}} E_i \sin\theta_i \cos\phi_i \\ E_y^{\text{miss,calo}} &= -\sum_{i=1}^{N_{\text{cell}}} E_i \sin\theta_i \sin\phi_i \\ E_T^{\text{miss,calo}} &= \sqrt{\left(E_x^{\text{miss,calo}}\right)^2 + \left(E_y^{\text{miss,calo}}\right)^2} \end{aligned} \tag{2.8}$$

where E_i, θ_i and ϕ_i are respectively the energy, the polar angle and the azimuthal angle of the calorimeter cells. The $\not\!\!E_T$ is reconstructed over the range $|\eta| < 5$ using only the calorimeter information.

Because of the high granularity of the calorimeter, it is crucial to suppress noise contributions, i.e. to limit the number of cells, N_{cell}, used in the $\not\!\!E_T$ sum. This is done by using only cells belonging to topoclusters, described in Section 2.3.3. Since the ATLAS calorimeters are non-compensating, it is necessary to develop a dedicated calibration scheme for the hadronic energy deposits in the calorimeters.

The first step in the commissioning of $\not\!\!E_T$ reconstruction, is to calibrate all the topocluster cells with the same scheme, independently of the object they belong to. Two calibration schemes have been developed, both based on the cell energy density: the global cell energy-density weighting calibration scheme and the local cluster weighting calibration scheme, already described in Section 2.3.3.

The most refined scheme developed in ATLAS calibrates cells energy on the base of the reconstructed "physics" object they belong to (refined calibration or *RefFinal*). Calorimeter cells are associated with a parent reconstructed and identified high-p_{T} object, in a chosen order: electrons, photons, hadronically decaying τ-leptons, jets and muons. They are separately and independently calibrated. The same is done for cells belonging to the topoclusters not associated with any object.

Once the cells are associated with categories of objects as described above and calibrated, $\not\!\!E_T$ is calculated as follows:

$$E_{x(y)}^{\text{miss,calib}} = E_{x(y)}^{\text{miss,e}} + E_{x(y)}^{\text{miss},\gamma} + E_{x(y)}^{\text{miss},\tau} + E_{x(y)}^{\text{miss,jets}} + E_{x(y)}^{\text{miss,calo},\mu} + E_{x(y)}^{\text{miss,CellOut}} \tag{2.9}$$

where each term is calculated from the negative sum of calibrated cell energies inside the corresponding objects. The $E_{x(y)}^{\text{miss,calo},\mu}$ is the contribution to $\not\!\!E_T$ from the energy lost by muons in the calorimeter. It contributes to the final $\not\!\!E_T$ according to the muon type used for the calculation of the $\not\!\!E_T$ muon term. The $E_{x(y)}^{\text{miss,CellOut}}$ term is

calculated from the cells in topoclusters which are not included in the reconstructed objects. An energy-flow algorithm has been developed to improve the calculation of the low-p_{T} contribution to $E_{x(y)}^{\mathrm{miss,CellOut}}$. Tracks are added to recover the contribution from the low-p_{T} particles which do not reach the calorimeter or do not seed a topocluster. The track momentum is used instead of the topocluster energy for the tracks associated to topoclusters, thus exploiting the better calibration and resolution of tracks at low momentum compared to topoclusters.

The most refined scheme used in *RefFinal* calculation improves the performance in terms of $\not{E}_T$ mean and resolution for events containing electrons, photons, taus, and muons for which the GCW or the LCW are not appropriate.

The final $E_{x(y)}^{\mathrm{miss,calib}}$ is then calculated from equation 2.9 adding the $E_{x(y)}^{\mathrm{miss},\mu}$ and $E_{x(y)}^{\mathrm{miss,cryo}}$ terms (see also Figure 2.18).

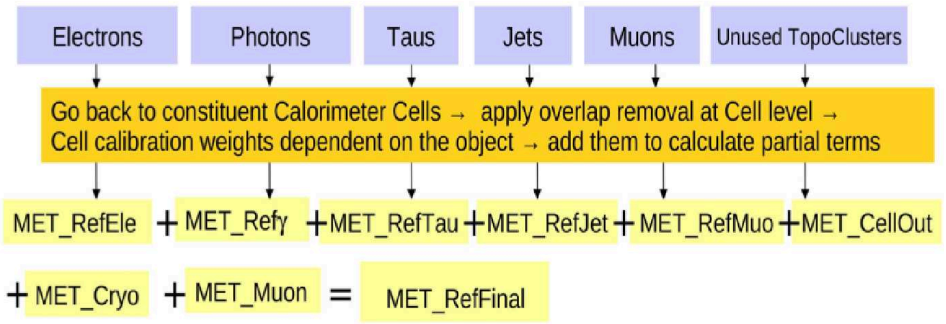

Figure 2.18: *Sketch to illustrate how the reconstructed physics objects are used to reconstruct $\not{E}_T$ [103].*

The $\not{E}_T$ muon term: The $\not{E}_T$ muon term is calculated from muon momenta measured in a range of pseudorapidity:

$$E_{x(y)}^{\mathrm{miss},\mu} = -\sum_{selected\ muons} E_{x(y)}^{\mu} \tag{2.10}$$

In the region $|\eta| < 2.5$ only good-quality muons in the Muon Spectrometer with a matched track in the Inner Detector are considered. The matching requirement considerably reduces contributions from fake muons.

The muon term is calculated in a different way for isolated and non-isolated muons[3].

- The p_{T} of an isolated muon is determined from the combined measurement of the Inner Detector and Muon Spectrometer. In this case the energy lost by the muon in the calorimeters ($E_{x(y)}^{\mathrm{miss,calo},\mu}$) is not added to the calorimeter term.
- For a non-isolated muon, the energy lost in the calorimeter cannot be separated from the nearby jet energy. The Muon Spectrometer measurement of the muon momenta after energy loss in the calorimeter is therefore used unless there is a significant mismatch between the spectrometer and the combined measurement. In this case the combined measurement minus the parametrized energy loss in the calorimeter is used.

For higher values of the pseudorapidity outside the fiducial volume of the Inner Detector ($2.5 < |\eta| < 2.7$), there is no matched track requirement and the Muon Spectrometer is used alone.

Apart from the loss of muons outside the acceptance of the Muon Spectrometer ($|\eta| > 2.7$), muons are lost in other small regions not covered by muon chambers. The muons reconstructed from the Inner Detector and calorimeter energy deposits can be used to recover these $\not\!\!E_T$ contributions.

The $\not\!\!E_T$ cryostat term: The cryostat between the LAr barrel EM Calorimeter and the Tile barrel has a thickness of about half an interaction length and it can lead to significant energy losses in hadronic showers. The cryostat term takes into account this lost energy. When the calorimeter term is calibrated with the LCW scheme, a corresponding correction is already done at the topocluster level, e.g. $E_{x(y)}^{\mathrm{miss,cryo}} = 0$.

The $\not\!\!E_T$ reconstruction, when it is calibrated with GCW, recovers this loss of energy in the cryostat using the correlation of energies between the last layer of the LAr calorimeter and the first layer of the Had Calorimeter. This correction is called the "cryostat term" when used for jet energy correction. It is defined as follows:

$$E_{x(y)}^{\mathrm{miss,cryo}} = -\sum_{jets} E_{x(y)}^{\mathrm{jet,cryo}} \tag{2.11}$$

where all reconstructed jets are summed in the event and:

$$\begin{aligned} E_x^{\mathrm{jet,cryo}} &= w^{\mathrm{cryo}} \sqrt{E_{EM3}^{\mathrm{jet}} \times E_{HAD1}^{\mathrm{jet}}} \frac{\cos\phi_{\mathrm{jet}}}{\cosh\eta_{\mathrm{jet}}} \\ E_y^{\mathrm{jet,cryo}} &= w^{\mathrm{cryo}} \sqrt{E_{EM3}^{\mathrm{jet}} \times E_{HAD1}^{\mathrm{jet}}} \frac{\sin\phi_{\mathrm{jet}}}{\cosh\eta_{\mathrm{jet}}} \end{aligned} \tag{2.12}$$

[3]A muon is not isolated if there is a jet in the event within a distance $\Delta\,\mathrm{R} = \sqrt{\Delta\eta^2 + \Delta\phi^2}$ of 0.3.

where w^{cryo} is a calibration factor, determined together with the cell signal calibration weights in the GCW fits. E_{EM3} and E_{HAD} are the energies in jets deposited on the third layer of the EM Calorimeter and in the first layer of the Had Calorimeter, respectively.

Performance of $\not\!\!E_T$ in proton-proton collisions

The performance of $\not\!\!E_T$ reconstruction in proton-proton collisions have been evaluated on 900 GeV, 2.36 TeV and 7 TeV centre-of-mass energy data. At the early stages of the data taking, just the calorimeter term in Equation 2.7 has been used for $\not\!\!E_T$ computation, as in minimum bias events the contribution from muons is negligible. Furthermore, topological cluster cells have been calibrated at the EM scale. The performance of $\not\!\!E_T$ at the EM scale are presented in [104] for 900 GeV and 2.36 TeV collisions and in [105] for 7 TeV collisions. The performance of calibrated $\not\!\!E_T$ in 7 TeV collision data are presented in [103], with already some results concerning the refined calibration of $\not\!\!E_T$. With full available 2010 statistics, the refined calibration has been commissioned and all the systematics have been evaluated as reported in [106].

For both analysis reported in this thesis a refined calibration has been used since it has the best performance, as shown in Figure 2.19. A quantitative evaluation of the $\not\!\!E_T$ performance can be obtained from a study of the (E_x^{miss},E_y^{miss}) resolutions as function of the total transverse energy $\sum E_{\text{T}}$, which is reconstructed from the calorimeters as:

$$\sum E_{\text{T}} = \sum_{i=1}^{N_{\text{cell}}} E_i \sin\theta_i \tag{2.13}$$

where E_i and θ_i are the cell energy and the polar angle, respectively and the sum only includes cells belonging to topoclusters.

The $\not\!\!E_T$ resolution, expressed as $\sigma(E_{x(y)}^{\text{miss}})$, scales in good approximation as $\sigma(E_{x(y)}^{\text{miss}}) = a \times \sqrt{\sum E_{\text{T}}}$, with scaling factors a depending both on detector and reconstruction performances. The lower is a, the best performance is achieved. The distributions shown in Figure 2.19 have been obtained using $Z \to ll$ events in data. In general no genuine $\not\!\!E_T$ is expected in these events, except a small contribution from the semi-leptonic decay of heavy-flavour hadrons in jets. Thus most of the $\not\!\!E_T$ reconstructed in $Z \to ll$ decays is a direct result of imperfections in the reconstruction process or the detector. This, coupled with the clean event signature for a $Z \to ll$ event and the relatively large cross section, means that it is a good channel in which to study $\not\!\!E_T$. The resolution is estimated from the width of the (E_x^{miss},E_y^{miss}) distribution in bins of $\sum E_{\text{T}}$. The core of each distribution is then fitted with a Gaussian over twice the expected resolution obtained from previous studies and the fitted width, σ, is shown as a function of $\sum E_{\text{T}}$.

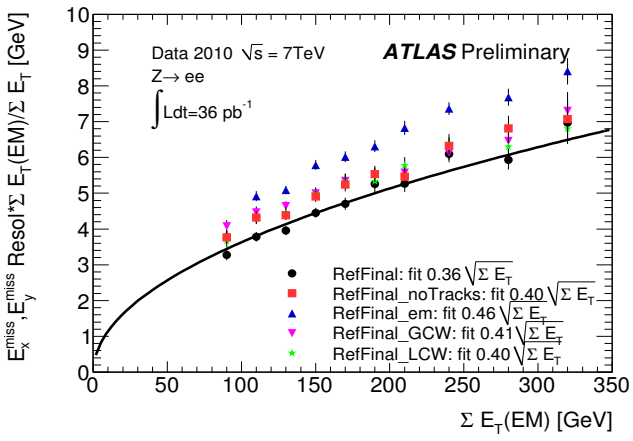

(a)

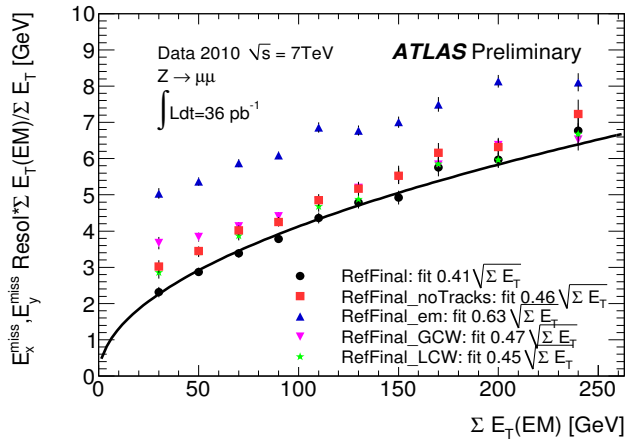

(b)

Figure 2.19: E_x^{miss} *and* E_y^{miss} *resolution as a function of the total transverse energy in calorimeters for* $Z \to ee$ *(a) and* $Z \to \mu\mu$ *(b) events in data. The* $\sum E_{\text{T}}$ *is at the EM scale and* E_x^{miss} *and* E_y^{miss} *are scaled by the ratio* $\sum E_{\text{T}}(EM)/\sum E_{\text{T}}$*. Different calibrations of* $\not\!\!E_T$ *are compared: the refined calibration with an without the use of the particle flow scheme for low* p_{T} *tracks, the uncalibrated* $\not\!\!E_T$*, the GCW calibration scheme and the LCW calibration scheme. The curve is the fit to the resolution of* $E_{x(y)}^{\text{RefFinal}}$*, and fit values are indicated for all* $\not\!\!E_T$ *calibration schemes used. The difference in the resolution observed between* $Z \to ee$ *and* $Z \to \mu\mu$ *events is expected due to the fact that* $\sum E_{\text{T}}$ *includes the electrons momenta in* $Z \to ee$ *events while muons momenta are not included in* $Z \to \mu\mu$*. After subtracting the electron momenta, the* $\not\!\!E_T$ *resolution in* $Z \to ee$ *is fully consistent with* $Z \to \mu\mu$*. Conversely, the resolution in* $Z \to \mu\mu$ *events after adding to the* $\sum E_{\text{T}}$ *in calorimeters the* p_{T} *of the two muons, is consistent with* $Z \to ee$*. [106].*

2.4 Physics analysis model

A single data taking run in ATLAS can last for many hours. Typically, one long run is taken during an LHC fill, and, if necessary, between fills, the run is stopped for detector calibrations. These runs are divided into *luminosity blocks* that are a few minutes long each. Luminosity blocks are the smallest units of data for an analysis in ATLAS. Each luminosity block can be included or excluded in the final analysis, as explained in Section 2.4.2.

ATLAS data are available to collaboration members in a variety of formats to fulfill the requirements of several kind of analyses: development of reconstruction algorithms, detector calibration, debugging and, finally, physics analysis. Data for physics analysis need to be filtered according to detector conditions and are accessed using the LHC Computing Grid [107]. In the following of this section, these aspects are detailed.

2.4.1 Data formats

ATLAS data are centrally divided into different streams, which correspond to the trigger that has been fired by the event. For example, in the analysis presented in this thesis the so-called "Egamma" and "Muon" streams have been considered, for which one trigger based on EM Calorimeter information and on muon chamber information respectively has been fired.

There are different data formats produced when data are collected.

The first two data formats are not used for analysis: the Byte-stream Data, which is a persistent presentation of the event data flowing from the HLT (which is the last level of the trigger decision, as described in Section 2.2.5) and the Raw Data Object Data (RDO) which is a C++ object representation of the byte-stream information. The latter can be sometimes used for detailed detector studies, when information about each single channel is needed.

Once the raw data have been collected and the program of offline calibrations has been performed, the reconstruction can start. The Event Summary Data (ESD) are the output of the reconstruction: these samples contain all the information about the detectors (e.g. energy released in each calorimeter cell) and about the reconstructed physics object (e.g. jets). The ESDs contain enough information to do, for example, track refitting: this is therefore the format usually used for the rapid tuning of reconstruction algorithms and calibrations. The next step is the production of Analysis Object Data (AOD) samples, which contain only a summary of the reconstruction (e.g. the information about calorimeter cells is not copied into AODs).

From these data format, some derived samples (dESD, dAOD) can be extracted, in which just a subset of the events is retained, but the information at event level remain the same. For example dAOD are produced by ATLAS Top Working Group asking the presence of one electron or one muon.

Another available data format are flat ntuples[4] (Derived Physics Data, DPD), which are derived from ESDs or AODs. These were mainly intended to be used by performance working groups, but they are intensively used also in physics analyses. Each performance group produces its own DPD, with a subset of event information. These ntuples are therefore small and easy to handle.

In addition, to further decrease the data dimensions, retaining only the events and information that are interesting for the analysis, a preselection is applied to the events, before the DPD production. The reduction is done following three criteria:

- *Skimming*: this implies the selection of the desired events from a larger dataset, e.g. selecting only events with one electron or one muon;
- *Thinning*: this implies the selection of only the required objects or containers of objects from the desired events, e.g. discarding photon containers if not needed;
- *Slimming*: this implies the selection of just the desired properties of an object, e.g. not using all the information about calorimeter cells associated to a jet.

The first analysis described in this thesis has been performed on 2010 data using AOD, while for the second one, 2011 data has been analysed and DPD produced by the ATLAS Top Working Group have been used.

2.4.2 Data quality

After data has been taken, the runs are assigned several data quality flags which define if the data are good enough to be used for physics analysis. Data quality flags are assigned for each sub-detector (separately for each component, i.e. barrel or end-cap) and for each reconstructed object (e.g. electrons, muons etc.) in each detector region. Moreover, the flags are assigned on a luminosity block base, to maximize the amount of data useful for the analyses. The flags are assigned by data quality shifters, looking at the status of the detector during a particular run and checking a set of histograms with interesting distributions, e.g. the distribution of timing for the pixel hits. A tool is implemented which automatically checks if the distribution under investigation is good or not, just comparing the distribution to a reference. But the data quality flag still needs to be assessed by a human being. For each physics analysis, according to the reconstructed object involved in it, a list of good quality luminosity blocks is defined: this is the so-called "Good Run List". This is obtained combining all the data quality flags and good luminosity block from the interesting subsystems/objects.

The good run list used by the ATLAS Top Working Group selects events in which green flags are set for all the objects involved in top quark pair events selection: trigger, electrons, muons, missing energy, jets and b-tagging. The integrated

[4] TTree objects based on the ROOT package [108]

luminosity corresponding to the good luminosity blocks is 35 pb^{-1} and 4.71 fb^{-1} for 2010 and 2011 data respectively. Figure 2.20 shows the relative fraction of good quality data delivered by the various ATLAS subsystems during the LHC fills with stable beams in pp collisions and after switching on the tracking detectors. In the upper plot, runs between March 30^{th} and October 31^{st} 2010, corresponding to a recorded integrated luminosity of 45 pb^{-1}, are accounted. The lower one has been obtained from 2011 data collected from March 13^{th} and October 30^{th} and corresponds to a recorded integrated luminosity of 5.2 fb^{-1}. When the stable beam flag is raised, the tracking detectors undergo a so-called "warm start", which includes a ramp of the high-voltage and, for the pixel system, turning on the preamplifiers. The inefficiency due to this is not included in the table above, but accounted for in the ATLAS data taking efficiency. The inefficiencies in the LAr calorimeter are mostly due to isolated HV trips and noise bursts. These will be partially recovered in the future. The other small inefficiencies are due to individual isolated problems with a given subdetector.

Inner Tracking Detectors			Calorimeters				Muon Detectors			
Pixel	SCT	TRT	LAr EM	LAr HAD	LAr FWD	Tile	MDT	RPC	CSC	TGC
99.1	99.9	100	90.7	96.6	97.8	100	99.9	99.8	96.2	99.8

Luminosity weighted relative detector uptime and good quality data delivery during 2010 stable beams in pp collisions at √s=7 TeV between March 30th and October 31st (in %). The inefficiencies in the LAr calorimeter will partially be recovered in the future.

Inner Tracking Detectors			Calorimeters				Muon Detectors				Magnets	
Pixel	SCT	TRT	LAr EM	LAr HAD	LAr FWD	Tile	MDT	RPC	CSC	TGC	Solenoid	Toroid
99.8	99.6	99.2	97.5	99.2	99.5	99.2	99.4	98.8	99.4	99.1	99.8	99.3

Luminosity weighted relative detector uptime and good quality data delivery during 2011 stable beams in pp collisions at √s=7 TeV between March 13th and October 30th (in %), after the summer 2011 reprocessing campaign

Figure 2.20: *Luminosity weighted relative fraction of good quality data delivered by the various ATLAS subsystems during the LHC fills with stable beams in pp collisions at* $\sqrt{s} = 7$ *TeV, and after switching the tracking detectors on [109]. Top plot: runs between March* 30^{th} *and October* 31^{st} *2010, corresponding to a recorded integrated luminosity of 45* pb^{-1}*, are accounted. Bottom plot: runs between March* 13^{th} *and October* 30^{th} *2011, corresponding to a recorded integrated luminosity of 5.2* fb^{-1}*, are accounted.*

2.4.3 Data distribution

The ATLAS Computing Model [107] foresees that just limited operations are done in situ by the computing facility at CERN (Tier0). The rest of the operation is done at the other computing sites (Tier1 and Tier2), which are spread around the world. The Tier0 performs monitoring, calibration and first-pass processing; it also hosts the first secure copy of the raw data and of the first pass output data formats. The 10 Tier1 sites receive the raw data and the first pass processing, and host the second secure copy of the raw data. They provide scheduled access for physics and detector groups to the processed data, and perform the reprocessing when calibrations and algorithms improve. They also host copies of the conditions database. The Tier2 sites are associated with a Tier1, and provide on-demand access to the processed data for physics analysts. Derived datasets produced by the physics groups are copied to the Tier2 facilities for further analysis. They also provide the simulation capacity for the experiment.

During my work I have used the Tier2 facilities in order to select data interesting for my analysis.

Chapter 3

Top quark pair production cross section measurement with full 2010 statistics

In this chapter a measurement of the top quark pair production cross section, performed with full available 2010 data, is described. At the beginning of my PhD I have done also a preliminary study on Monte Carlo simulation. This work is not discussed in this thesis, but is fully documented in [110] and [111].

The results presented in this chapter has been reported in one paper [112], in two ATLAS collaboration conference notes [113] [114] and in one internal report [115].

The analysis has been done selecting events in which top quark pairs decay semileptonically. Within the Standard Model (SM), the top quark almost always decays in $t \to Wb$ and the decay topologies are determined by the decays of the W bosons, as described in Section 1.3.2. The semileptonic mode ($t\bar{t} \to \ell\nu j\, bjj$) has a branching ratio (BR) of 34.3%, combining both e and μ lepton flavours[1]. Events in which one W decays hadronically and the other one in an hadronically decaying τ + ν have been not considered. The identification of hadronically decaying τ's is far more challenging with respect to the electron and muon one, because of the large QCD background at the LHC. Dedicated studies have been done and reported in [116].

Semileptonic events are characterized by the presence of one isolated lepton, missing transverse energy and jets, some with b flavour.

The dominant background processes to this channel are given by direct p-p production of a W in association with jets and by QCD multijets events. Both of them have been estimated using data-driven techniques as described in Sections 3.3 and 3.5.1. Other backgrounds are single top, Z+jets and diboson events, which have a minor impact and have been estimated using Monte Carlo predictions.

- *W+jets*: This background is very difficult to keep under control. If the W

[1] The BR include the small contributions to $W \to \ell$ from $W \to \tau \to \ell$.

boson decays leptonically and it is produced in association with at least 4 jets, it can have indeed exactly the same experimental signature of the signal. Furthermore the predictions coming from Monte Carlo are not very reliable, since they are affected by large uncertainty ($> 60\%$). For this reason data driven techniques for its estimate have been developed. This background can be strongly reduced asking for the presence of a b-jet in the event, using b-tagging techniques. The fraction of heavy flavour jets produced in association with the W is small, but still not negligible. Furthermore the request of one b-jet causes an increase in the uncertainty on the W+jets background estimate, as described in detail in Section 3.4.

- *QCD*: Multijet events, produced by the strong interactions, are expected to contain neither isolated leptons nor $\not\!\!E_T$. However, they are present in the selected samples due to the imperfect reconstruction in the detector. Mismeasurement of missing transverse energy in combination with a fake isolated lepton is quite uncommon, but since the QCD cross section is 4 order of magnitude greater than the top quark pair one, the contribution of this background is not negligible. Non-isolated leptons coming from heavy quark decay can simulate an isolated electron or muon coming from the W boson. In addition, fake electrons can come from photon conversions and hadrons and so this background gives a bigger contribution in the electron channel. As for W+jets this background is estimated using data driven techniques in both electron and muon channel.

- *Single top*: Top quarks can be produced also individually through weak interaction. The presence of other jets in the event can simulate a top quark pair decay.

- *Z+jets*: As the W boson, also the Z boson decaying leptonically can be produced in association with hadronic jets. These events are not characterized by true missing energy and they can be included in the selection if one of the lepton coming from the Z is not identified or reconstructed. Furthermore the Z boson production cross section is 10 times smaller with respect to the W boson one, so the contribution of this background is significantly lower with respect to the W background.

- *Dibosons*: This background includes WW, WZ and ZZ production. It is strongly reduced by the fact that its cross section is ten times smaller with respect to the top quark pair production one.

This analysis is based on a counting method. The number of top quark pair candidates N_{sig} is obtained from the difference between the number of events passing a given set of cuts observed in data (N_{obs}) and the estimated background contribution N_{bkg}.

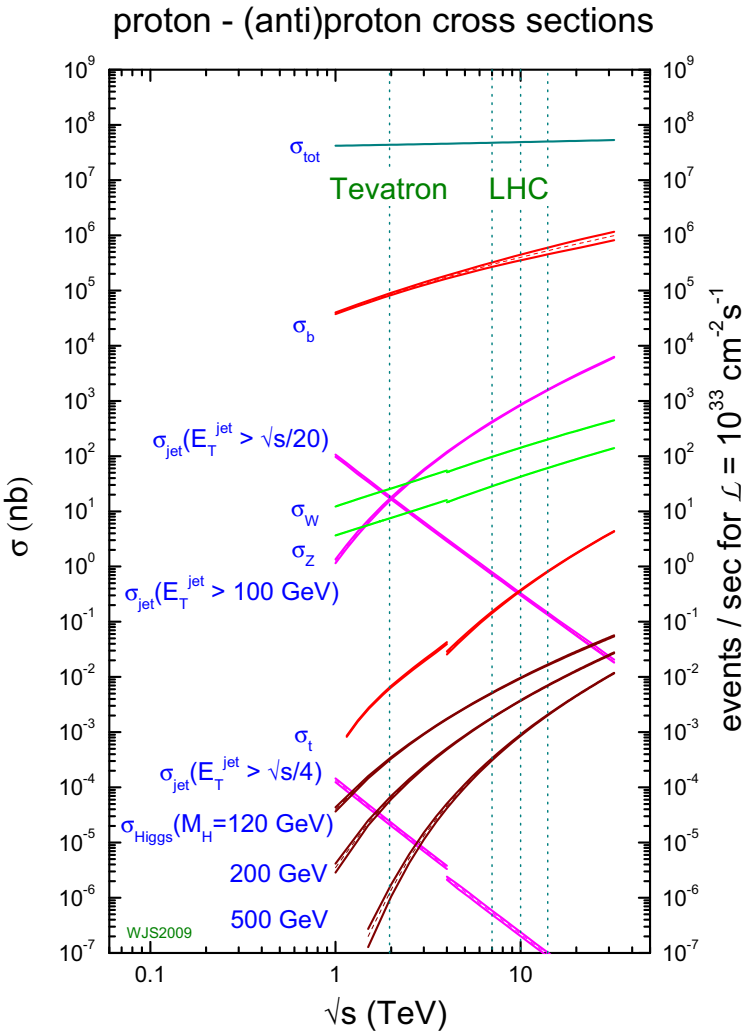

Figure 3.1: *Cross sections for several interesting and proposed physics processes as a function of center-of-mass energy [117]. The discontinuity at 4 TeV is from the transition from proton-anti-proton on the left to proton-proton collisions on the right. The vertical lines indicate the running energy of the Tevatron ($\sqrt{s}$ = 1.96 TeV), the current running energy of the LHC ($\sqrt{s}$ = 7 TeV), and two possible future running energies of the LHC ($\sqrt{s}$ = 10 and 14 TeV). The cross sections shown are, from largest to smallest, the total scattering cross section (σ_{tot}), the bottom-quark production cross section (σ_b), the production cross sections for jets above several energy cut offs (σ_{jet}), the W, Z, and top-quark production cross sections (σ_W, σ_Z, σ_t) and the production cross sections for a theoretical SM Higgs boson at with several masses (σ_{Higgs}).*

The $t\bar{t}$ cross section is then extracted using the formula:

$$\sigma(t\bar{t}) = \frac{N_{sig}}{L \times \epsilon} = \frac{N_{obs} - N_{bkg}}{L \times \epsilon} \tag{3.1}$$

where L is the integrated luminosity and ϵ is the signal acceptance that will be discussed in Section 3.6.

Results are discussed for two different selections of signal candidates: one which makes use of the b-tagging information and one which does not.

Within this analysis I have primarily focused on the estimate of W+jets background. In particular I have performed some preliminary studies on Monte Carlo simulations, some of which reported in [118], and then I have applied the developed techniques on data to obtain the W+jets estimate used in the presented analysis. In addition, I have contributed to the choice of signal selection cuts and to the development of data driven techniques for QCD background estimate.

The chapter is organized as follows. After a brief introduction, the data and the Monte Carlo simulation samples used for the analysis are presented. In Sections 3.2.1 and 3.2.2 the reconstructed object and common event selections are described. The cut and count analysis is then discussed in detail, including the estimates of backgrounds using data control samples. Finally the results obtained in the electron and muon decay channels are combined for each of the two selections considered.

3.1 Data sample

3.1.1 Data

The analysis presented in this chapter is based on the full available proton collision 2010 data, collected by the ATLAS detector. As explained in section 2.4.2 only the data satisfying specific quality requirements are considered for the analysis. The ATLAS Top Working Group selects events with stable beams and in which green flags are set for all the objects involved in top quark pair events selection: trigger, electrons, muons, missing energy, jets and b-tagging. The data used for the analysis correspond to an integrated luminosity of $35.3 \pm 3.2\%$ pb^{-1} .

ATLAS data are centrally divided into different streams, which correspond to the trigger that has been fired by the event. Since the selected events are characterized by the presence of an energetic muon or an energetic electron, the so called "Egamma" and "Muon" streams have been considered. Triggers used in the analysis are described in detail in Section 3.2.2 for both electron and muon channel.

3.1.2 Monte Carlo

Monte Carlo simulation samples have been used to develop and validate the analysis procedures, to calculate the acceptance for $t\bar{t}$ events and to evaluate the contributions from some background processes. After event generation, all samples have

been processed with the GEANT4 [119] simulation of the ATLAS detector [120], reconstructed and passed through the same analysis chain as the data.

For the generation of $t\bar{t}$ signal and single top events, MC@NLO [121] v3.41 was used, with Parton Density Function (PDF) set CTEQ66 [122], assuming a top mass of 172.5 GeV and normalising the $t\bar{t}$ cross section to the prediction of HATHOR[123] of 165.2 pb at approximate next-to-next-to leading order (NNLO) in QCD. For single top the s, t and Wt channels are included, normalising to the MC@NLO cross section and using the "diagram removal scheme" [124] for Wt to remove overlaps with the $t\bar{t}$ final state.

For the generation of W+jets, Drell-Yan events (γ/Z+jets) and QCD multijet events, ALPGEN v2.13 was used, invoking the MLM matching scheme [125] with matching parameters `RCLUS`=0.7 and `ETCLUS`=20, and using PDF set CTEQ6L1 [126]. The additional jets in events were controlled with the ALPGEN parameter `ptjmin=15`. For each of these background processes separate samples have been generated that include $b\bar{b}$ and $c\bar{c}$ quark pair production (with no minimum transverse momentum cut on the heavy quarks) at the matrix element level. For W+jets an additional sample containing W+c or $\bar{c}$+jets exists. These heavy flavour samples have been matched with their light jet counterparts as described below. For the Drell-Yan sample the phase space has been restricted to $40 < m(l^+l^-) < 2000$ GeV. The W/Z+jets samples were normalised with a K-factor of 1.25.

For the QCD multijet sample, the generator-level p_{T} of the leading parton must be at least 17 GeV. QCD multijet events have also been subjected to filtering prior to the full event simulation: the events must have either a truth muon within $|\eta| < 2.8$ with a p_{T} of at least 10 GeV, or contain at least three truth jets (reconstructed from simulated stable particles after hadronisation with the anti-k_t algorithm with parameter R=0.4) with a greater than 25 GeV, as well as an additional truth jet with a p_{T} greater than 17 GeV. The QCD samples were normalised using the ALPGEN prediction. All events were hadronised with HERWIG [127], using Jimmy [128] for the underlying event model.

Diboson WW, WZ and ZZ events were produced using HERWIG and normalised with appropriate K-factors to match the total cross section from NLO QCD calculations made with MCFM [129].

Heavy flavour overlap removal

Unlike the matching of matrix element (ME) partons and jets from the parton shower (PS) there is no attempt in ALPGEN to match heavy flavour (b and c) quarks explicitly. Thus it is possible for the same heavy flavour states to arise in multiple samples. For example it is possible for a state of $W+$ $b\bar{b}$ to arise from the W + two additional partons sample and from the W + $b\bar{b}$ + no additional partons sample. To avoid double counting when combining multiple ALPGEN samples together it is therefore necessary to veto certain classes of events in each of the samples.

The approach chosen to remove this double counting exploits the different strengths

of the ME and PS treatment in ALPGEN. The ME performs best when there is a large opening angle between the quarks. The PS performs best for collinear splittings. The events are classified according to the sample they are generated in, and the distance in η–ϕ space, ΔR, between heavy quark pairs in the event compared to a matching distance ΔR_{max} (chosen to be 0.4 in this case). The treatment of the different samples is then as follows:

- W+light jets: Events are vetoed if they contain heavy quarks in the ME or if there are any heavy quark pairs from the PS with $\Delta R > \Delta R_{\text{max}}$;
- W+c or $\bar{c}$ + jets: Events are vetoed if they contain heavy quark pairs from the PS with $\Delta R > \Delta R_{\text{max}}$;
- W+$c\bar{c}$ + jets: Events are vetoed if the $c\bar{c}$ pair in the ME has $\Delta R < \Delta R_{\text{max}}$ or if there are any $b\bar{b}$ pairs from the PS with $\Delta R > \Delta R_{\text{max}}$;
- W+$b\bar{b}$ + jets: Events are vetoed if the $b\bar{b}$ pair in the ME has $\Delta R < \Delta R_{\text{max}}$.

Approximately 5.5% of the total number of W+jets events is vetoed by this procedure.

Samples used to evaluate systematic uncertainties

Uncertainties on the $t\bar{t}$ acceptance have been evaluated by comparing the predictions of MC@NLO with those of POWHEG [130] interfaced to both HERWIG and PYTHIA. The effects of the variations in the amount of initial and final state radiation (ISR/FSR) have been studied using the ACERMC generator [131] interfaced to PYTHIA, and varying the parameters controlling ISR and FSR in a range consistent with experimental data [132]. Finally samples with different PDF sets have been used to compute this contribution to the total uncertainty.

As explained before, W+jets background is estimated from data, but the developed techniques are not 100% data driven and they need some input from Monte Carlo. It's important to test the robustness of this input against the choice of the Monte Carlo generator and the choice of its critical parameters. The uncertainty on these methods has been evaluated comparing the predictions obtained with different Monte Carlo samples as explained in Section 3.3. For this purpose W+jets and Z+jets samples generated with SHERPA [133] have been used and ALPGEN samples with some varied parameters have been generated[2]. The set of varied parameters covers the renormalization and the factorization scales, controlled in ALPGEN by the *iqopt* parameter. Furthermore samples with a different *ktfac* values have been generated: this parameter controls the scale of α_s of each additional parton vertex. Finally the parameters that control the matching in p_{T} (*ptjmin*) and ΔR (*drjmin*) between matrix element and parton shower have been varied. All these samples have not been processed with the GEANT4 simulation of the ATLAS detector. Event selection has been done on Monte Carlo truth objects.

[2]Parameters are varied one at the time.

3.2 Object and event selection

3.2.1 Object selection cuts

The reconstruction of $t\bar{t}$ events makes use of reconstructed electrons, muons, jets and the missing transverse energy $\not{E}_T$. The following criteria have been used to define the selected objects in the events.

- *Electrons*:

  Electrons are selected using the electron quality requirements enclosed in the tight electron definition, described in Section 2.3.1. Furthermore some kinematic cuts are applied: their p_{T} is required to be greater than 20 GeV and the pseudorapidity of the calorimeter energy cluster associated with the candidate must satisfy: $|\eta_{cluster}| < 2.47$, excluding the calorimeter crack region at $1.37 < |\eta_{cluster}| < 1.52$. Electrons from prompt W decay are isolated from jet activity, unless there is an accidental overlap with a jet in the event. At the opposite, two important sources of backgrounds, hadrons faking electron signature and electrons from heavy-flavour decays, are characterized by close jet activity. In order to suppress this contamination we require an isolation cut. The E_{T} deposited in the calorimeter towers in a cone in η-ϕ space of radius $R = 0.2$ around the electron position is summed and the E_{T} due to the electron is subtracted. Leakage corrections are then applied in order to minimise the dependence on the p_{T} of the electron and pile-up effects. Finally the remaining E_{T} is required to be less than 4 GeV.

- *Muons*:

  Muons are reconstructed using MuId algorithm and only combined muons are selected for the analysis as described in Section 2.3.2. Kinematic cuts are also applied: the muon p_{T} is required to be greater than 20 GeV and the muon $|\eta|$ lower than 2.5. Furthermore quality cuts are applied on the Inner Detector track associated to the muon. These cuts set a lower limit on the number of Pixel, SCT and TRT hits associated to the track and an upper limit on the number of Pixel and SCT layers on track with absence of hits (Pixel and SCT holes). To reduce the background from leptons from heavy flavour decays inside jets, the muons in each event are required to be isolated. The corresponding calorimeter isolation energy in a cone of $R = 0.3$ is required to be less than 4 GeV and the analogous sum of the track transverse momenta in a cone of $R = 0.3$ is also required to be less than 4 GeV. Additionally, muons are required to have a distance ΔR greater than 0.4 from any jet with p_{T} >20 GeV in order to further suppress muons from heavy flavour decays inside jets.

- *Jets*:

Jets are reconstructed with the anti-k_t algorithm ($R = 0.4$) clustered from EM-scale topological clusters in the calorimeters. These jets are then calibrated to the hadronic energy scale, using the EMJES calibration. A p_{T} and η dependent correction factor, obtained from simulation [134], is applied on jets as described in Section 2.3.3. The jet origin correction is applied: the jet direction is changed such as it points back to primary vertex. Pile-up corrections, for subtracting contributions to measured energy due to multiple proton interactions, have not been applied at this stage of the analysis. Finally jets are requested to be well separated from a selected electron. If a jet is the closest jet to an electron candidate and the corresponding distance ΔR is less than 0.2, the jet is discarded from the selection in order to avoid double-counting of electrons as jets.

- *b-jets*: Jets are tagged as b-jets if the secondary vertex-based tagger SV0, described in Section 2.3.4, returns a weight value above the threshold of 5.85. This weight corresponds to about 50% tagging efficiency, obtained from studies of simulated $t\bar{t}$ events [135].

- *Missing transverse energy:*

  Missing transverse energy has been reconstructed using the most refined scheme developed in ATLAS, which calibrates topoclusters energy on the base of the reconstructed "physics" object they belong to, as described in Section 2.3.5. Deposits associated with jets are taken at the corrected energy scale (EMJES), while the contribution from deposits associated with electrons are substituted by the calibrated transverse energy of the electron, taking away the correction for out-of-cluster effects to avoid double cell energy counting. Finally, the contribution from muons is included after an adjustment for the muon contribution to calorimeter energy deposits.

3.2.2 Event selection cuts

The analysis starts by requiring events selected online by a single lepton trigger (e or μ), with a threshold which is fully efficient for leptons satisfying $p_{\mathrm{T}} > 20$ GeV. The detailed trigger requirements vary through the data-taking period, due to the rapidly increasing LHC luminosity and the commissioning of the trigger system. For electrons, a Level1 electromagnetic trigger object of at least 10 GeV is always required. In later data, an event filter trigger based on a more refined electromagnetic cluster selection and subsequently a calorimeter-track match has been required. Muons are selected requiring a 10 GeV-threshold muon trigger chamber track at Level1, matched by a muon reconstructed in the precision chambers at the event filter level in later data.

An electron trigger is required to match to a reconstructed electron that passed all the analysis cuts within ΔR=0.15, where ΔR is the η-ϕ distance between the

ROI of the trigger and the calorimeter cluster of the offline electron. For muon triggers a match has been required between the track of a reconstructed muon that passed all the analysis cuts and a ROI within ΔR=0.15.

To suppress non-collision backgrounds, only the events that have a reconstructed primary vertex with at least 5 tracks are accepted for the analysis. Events are then discarded if any jet with $p_{\mathrm{T}} > 20$ GeV at the EMJES scale and positive energy fails a set of quality cuts, which corresponds to *Loose bad* jet definition from the ATLAS Jet and Missing Energy performance group. These kind of jets are not associated to in-time real energy deposits in the calorimeters and they are caused by various sources ranging from hardware problems in the calorimeter, the LHC beam conditions and the atmospheric muon-ray induced showers. The bad jet definition relies on the set of calorimeter variables reported below:

- f_{EM} is the fraction of the jet energy in the EM Calorimeter,
- f_{max} is the maximum energy fraction in one calorimeter layer,
- HEC_f is the fraction of jet energy in the Liquid Argon Hadronic (LAr) Endcap Calorimeter,
- $LArQuality$ is the fraction of LAr calorimeter cells with a cell Q-factor, which is a measure of the difference between the measured and the prediction of the pulse shape used to reconstruct the cell energy,
- $Timing$ is the jet time with respect to the bunch crossing, calculated via an energy weighted sum of the timing from all the cells associated to the jet,
- $n90$ is the minimum number of energy ordered cells which account for at least 90% of the jet energy,
- η_{EM} is the jet pseudo-rapidity w.r.t. the detector origin,

The bad jets selection cuts are summarized on Table 3.1. A jet is flagged as bad if it satisfies at least one of these requirements.

To avoid inconsistencies and double counting, events in which a selected electron and muon candidate (before the muon-jet ΔR isolation requirement) share the same track have been removed and not considered in the rest of the analysis.

3.2.3 Systematic uncertainty related to selection cuts

The signal acceptance and some background processes are estimated from Monte Carlo simulation. The results are reliable only if the ATLAS detector response and imperfections, as much as the performance of the various physics objects are well modelled in the simulation. Uncertainties on this modelling must be translated in a systematic uncertainty on the signal acceptance and on the number of background events produced by Monte Carlo.

Category	cuts
Loose	$f_{EM} > 0.95 \cap \lvert LArQuality \rvert > 0.8$ $HEC_f > 0.8 \cap n90 <= 5$ $HEC_f > 0.5 \cap \lvert LArQuality \rvert > 0.5$ $\lvert Timing \rvert > 25ns$ $f_{EM} < 0.05$ $f_{max} > 0.99 \cap \lvert \eta_{EM} \rvert < 2$

Table 3.1: Loose bad selection cuts: a jet is flagged as bad if it satisfy at least one of these requirements.

The Monte Carlo simulation modelling of the lepton trigger, reconstruction and identification efficiencies[3] have been made to agree with data by applying efficiency scale factors as multiplicative event weights. These weights have been assessed using "tag and probe" techniques on $Z \to ee$ and $Z \to \mu\mu$ events selected in 2010 data, as well as on Monte Carlo simulated Z samples. These events are selected by requiring the presence of a lepton satisfying all selection cuts (tag lepton) and one lepton satisfying a subset of cuts (probe lepton) with an invariant mass in a window around the true Z boson mass. This would permit to have a pure Z sample in data. The efficiency of a given selection cut is then obtained as the probability of the probe lepton to pass this cut.

Each SF is defined as follows:

$$SF_{trigger,reco,Id} = \frac{\varepsilon_{trigger,reco,Id}(Z, data)}{\varepsilon_{trigger,reco,Id}(Z, MC)} \tag{3.2}$$

where $\varepsilon_{trigger,reco,Id}(Z, data\ (MC))$ are the efficiencies at the various stages as extracted with the tag and probe method, which is assumed to provide an unbiased estimation of the *true* efficiency ratio between data and Monte Carlo. The dependence of these weights as a function of geometric, kinematic and isolation quantities has been tested.

The electron trigger and reconstruction scale factors have been found to be constant and equal to 0.995 ± 0.005 and 1.000 ± 0.015 respectively. The electron identification efficiency shows, at the opposite, a significant dependence on the electron η, due to a mis-modelling of TRT variables, and also a dependence on the electron E_{T}. The value of this scale factor has been parametrized as a function of these two quantities. For what concern muons reconstruction and identification, the weights have been found to constant and their product is equal to 0.999 ± 0.004, while the trigger weight has shown a dependence on the muon η. The uncertainty on these quantities include statistical and systematic uncertainty. The most important contributions to the systematic uncertainty come from the dependence Z mass

[3]Reconstruction efficiency refers to standard object selection cuts proposed by performance groups, while identification efficiency refers to top-analysis specific selection cuts.

window cut, the background subtraction procedure to Z sample in data and the dependence on the choice of lepton quality cuts.

The accuracy of the lepton momentum scale and resolution in simulation was checked using reconstructed distributions of the Z mass, as reported in and [95] [136]. Small discrepancies have been found in data and Monte Carlo resolution. As a results of these studies, functions for smearing the p_{T} of the lepton, as a function of its p_{T} and η have been provided. The uncertainty on the signal acceptance and on the backgrounds estimated from Monte Carlo has been calculated varying the various scale factors and object energy scales within the uncertainties. The effect of lepton energy scales has been evaluated taking also into account the repercussion on the missing transverse energy. Since $\not\!\!E_T$ is obtained as the negative sum of all energy deposits in the detector, a change in the energy of a reconstructed object will directly translate in a variation of $\not\!\!E_T$ value. For each event $\not\!\!E_T$ has been then re-calculated using the rescaled lepton energy instead of the original one.

Furthermore the electron energy scale is corrected in the data at analysis level, in order to reproduce the Z boson mass peak.

The jet energy scale (JES) uncertainty has been computed as a function of the jet p_{T} and η using a tool provided by the ATLAS Jet-ETmiss performance group (`MultijetJESUncertaintyProvider` tool). The uncertainty for jets with $p_{\mathrm{T}} > 25$ GeV and $|\eta| < 2.5$ is about 5%. The increased uncertainty for close-by jets is taken into account by adding in quadrature a 5% uncertainty when another jet with $p_{\mathrm{T}} > 10$ GeV is found within Δ R< 0.6. The signal acceptance and the number of background events are calculated for JES up and JES down variation. As for lepton energy scale, $\not\!\!E_T$ variations have been taken into account. The difference with respect to the results with nominal JES is taken as a systematics. The errors coming from JES uncertainty are asymmetric, but in the following they are quoted as symmetric if the difference is not significant. The jet momentum in the simulated samples is smeared in order to match the resolution measured in the data and the difference with respect to the unsmeared Monte Carlo simulation is considered as the systematic uncertainty.

The performance of the SV0 b-tagging algorithm has been studied in the data in various control samples [135]. These studies show that the simulation efficiencies for tagging b, c quarks in jets have to be scaled by jet p_{T} dependent factors that differ from unity by at most 18%. The uncertainty on the b-tagging efficiency is dominated by systematics and varies from 8% at low p_{T} to 20% at high p_{T}. The uncertainty is approximately a factor of two larger for c-tagging. The rate for light quarks tags has to be scaled by a p_{T} dependent factor with values between 0.92 and 2.59 and associated uncertainties ranging between 20% and 100%.

The LHC instantaneous luminosity varied by several orders of magnitude during the 2010 data-taking period, reaching a peak of about 2×10^{32} cm^{-2}s^{-1}. At this luminosity an average of about three extra pp interactions are superimposed on each collision event. This "pile-up" background produces additional activity in the detector, affecting *e.g.* jet reconstruction and isolation energy variables. The

data driven determinations of efficiencies and background levels naturally include the effect of pile-up. When Monte Carlo simulation is used, the samples used have an average of two additional pileup events simulated with PYTHIA, overlayed to the hard scattering process before event digitization and reconstruction. This corresponds approximately to the average level of pile-up in the data taking periods under consideration. A systematic uncertainty has been computed comparing the results with the nominal pile-up in the simulation with those obtained by a reweighting procedure designed to obtain the same distribution for the number of vertices in the simulation and the data sample.

3.2.4 Signal region and control region selection

The specific event selection of events for the single lepton analysis consists of a series of kinematic requirements on the reconstructed objects defined in Section 3.2.1. For each lepton flavour signal events are selected asking:

- the appropriate single electron or single muon trigger has fired,
- the event contains exactly one lepton (electron or muon) with $p_{\mathrm{T}} > 20$ GeV, matching the corresponding trigger object,
- $\not\!\!E_T > 35$ GeV and $m_T(W) > 25$ GeV (electron channel), or $\not\!\!E_T > 20$ GeV and $\not\!\!E_T + m_T(W) > 60$ GeV[4] (muon channel),
- at least four jets with $p_T > 25$ GeV all with $|\eta| < 2.5$.

This sample is labeled "pretag" referring to the fact that no b-tagging information has been used. A subset of this sample is then defined with the additional requirement that at least one of the jets with $p_{\mathrm{T}} > 25$ GeV is tagged as a b-jet. It is referred to as the "tagged" sample. Control samples for background determination are defined asking the presence of exactly one, two and three jets (instead of at least four). Furthermore the tagged subset samples are selected requiring that at least one of the jets is tagged as a b-jet.

Figure 3.2 shows the jet multiplicity for events in the pretag (top row) and in the tagged (bottom row) samples. The signal region is comprised of the last ($\geq$ 4-jet) bin in histograms of the tagged and pretag samples.

Figure 3.3 shows the distribution of the number of tagged jets in events passing the signal selection (at least four jets).

Table 3.2 and 3.3 list the corresponding number of events in the four tagged and untagged samples. For all samples the contributions estimated from Monte Carlo simulation for $t\bar{t}$, W+jets, Z+jets and single top events are listed. The errors include uncertainties from the object reconstruction and identification and the

[4]Here $m_T(W)$ is the transverse mass, defined as $\sqrt{2p_T^{\ell}p_T^{\nu}(1-\cos(\phi^{\ell}-\phi^{\nu}))}$ where the measured $\not\!\!E_T$ vector provides the neutrino information.

theoretical cross section uncertainty. The uncertainty on the $t\bar{t}$ cross section is 40% for all jet multiplicity bins, while the one for single top and dibosons is 10% and 5% respectively. The uncertainty on W(eν, $\mu\nu$ and $\tau\nu$)+jets and Z(ee, $\mu\mu$ and $\tau\tau$)+jets depends on the number of associated jets. A 20% and 30% uncertainties are considered for the 1-jet and 2-jet bins respectively, 40% for the 3-jet bin and 60% uncertainty for the predictions for the sample with at least 4 jets.

The data driven estimates for the QCD multijet background discussed below are also quoted.

The background within the selected samples is dominated by W+jets events, which have the same final state signature as $t\bar{t}$ signal events. However, there are non-negligible contributions from processes where the reconstructed lepton does not originate from the decay $t \to (W \to \ell\nu)b$, but instead from a mis-reconstructed jet.

3.3 Data Driven estimate of W+jets background without b-tagging request

In this section three techniques for W+jets background estimate, before b-tagging request, are presented.

- The first approach exploits the fact (known as Berends scaling) that the ratio of W+n jets to W+n+1 jets is expected to be approximately constant as a function of n [137, 138]. The number of W events in the 4-jet pretag sample can thus be estimated as:

$$W^{\geq 4\text{jets}} = W^{2\text{jets}} \cdot \sum_{i=2}^{\infty} (W^{2\text{jets}}/W^{1\text{jet}})^i \tag{3.3}$$

  Here, the measurements of W+1jet and W+2jet control samples are performed before the requirement that one jet is tagged as a b-jet.

- The second approach uses the fact that the W/Z ratio is better known than the inclusive W+jets rates. The number of W events in the 4-jet pretag sample can thus be estimated as:

$$W^{\geq 4\text{jets}} = W^{1\text{jet}}_{\text{data}} (Z^{\geq 4\text{jets}}/Z^{1\text{jet}})_{\text{data}} \cdot C_{\text{MC}}, \qquad C_{\text{MC}} = \frac{(W^{\geq 4\text{jets}}/W^{1\text{jet}})_{\text{MC}}}{(Z^{\geq 4\text{jets}}/Z^{1\text{jet}})_{\text{MC}}} \tag{3.4}$$

  where C_{MC} is a coefficient estimated from Monte Carlo; $Z^{1\text{jet}}$ and $Z^{\geq 4\text{jets}}$ are the number of events characterized by the presence of a Z boson produced in association with exactly one jet and at least 4 jets respectively. The selection of these events and the estimation of C_{MC} are described in Section 3.3.1.

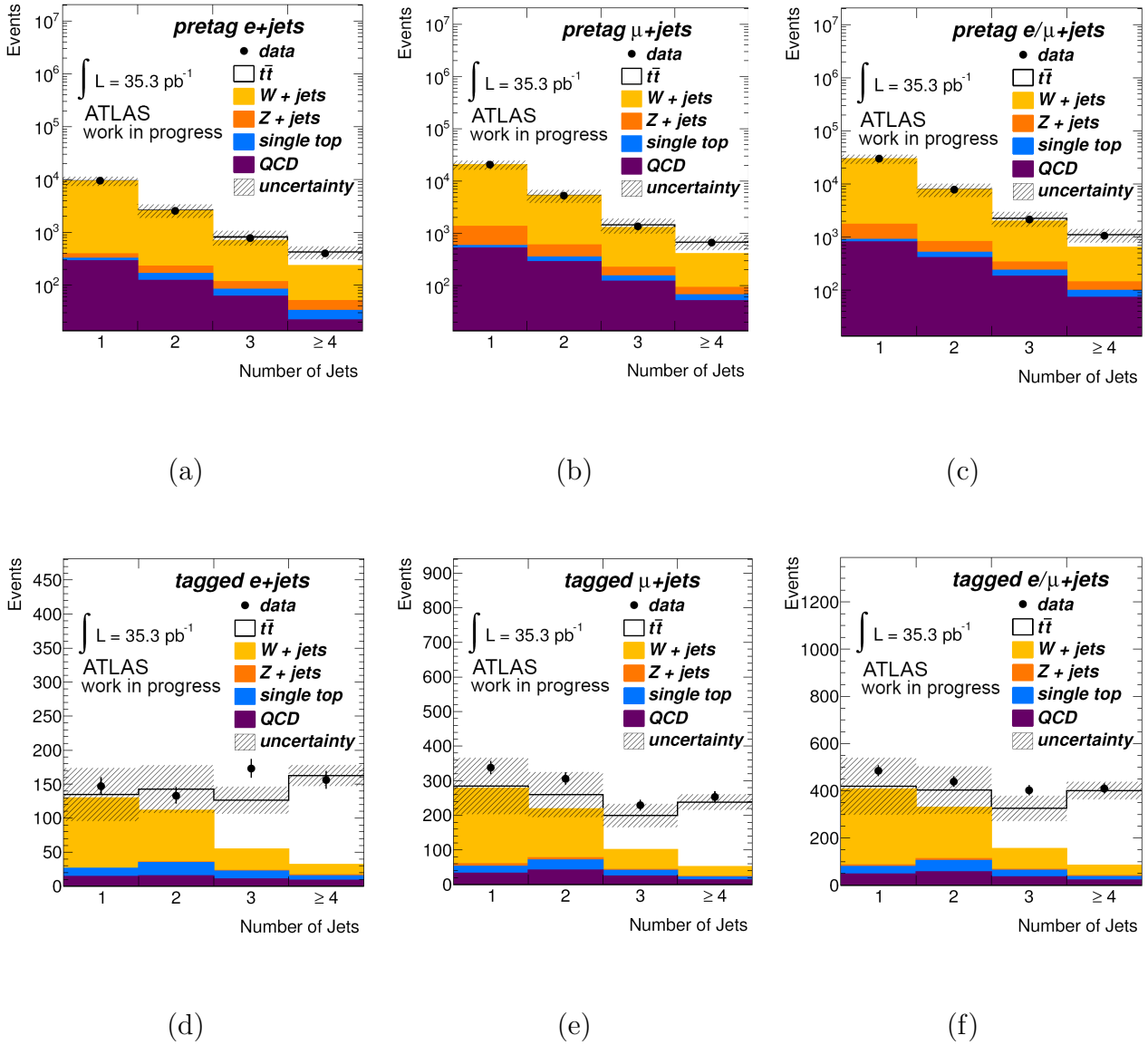

Figure 3.2: *Jet multiplicity distributions (i.e. number of jets with $p_T > 25$ GeV). Top row - pretag samples: a) electron channel, b) muon channel and c) e/mu combined. Bottom row - tagged sample: d) electron channel, e) muon channel and f) e/mu combined. The data are shown by the points with error bars, compared to the sum of all expected contributions, taken from simulations ($t\bar{t}$, single top, W and Z+jets) or estimated using a data driven technique (QCD multijet). The hatched area shows the uncertainty on the total expectation due to the uncertainty on the W+jets, QCD and other background estimate.*

e+jets channel, pretag				
	1-jet	2-jet	3-jet	≥4-jet
$t\bar{t}$ (MC)	14.3 ± 2.9	61.0 ± 9.2	116.3 ± 12.8	193.5 ± 27.1
QCD (DD)	287 ± 143.5	123 ± 61.5	62 ± 31.0	22 ± 11.0
W+jets (MC)	9005.4 ± 1891.7	2337.2 ± 748.1	584.2 ± 251.2	182.5 ± 115.0
Z+jets (MC)	65.1 ± 13.7	62.4 ± 20.0	32.2 ± 13.8	18.1 ± 11.4
single top (MC)	35.7 ± 4.3	42.2 ± 5.1	21.6 ± 3.9	10.9 ± 2.5
dibosons (MC)	35.3 ± 2.8	30.1 ± 2.4	9.3 ± 1.5	2.7 ± 0.6
Total background	9428.6 ± 1897.1	2594.9 ± 750.9	709.3 ± 253.5	236.2 ± 116.1
Total expected	9442.9 ± 1897.1	2655.9 ± 751.0	825.6 ± 253.8	429.7 ± 119.2
Observed	9481	2552	781	400

(a)

e+jets channel, tagged				
	1-jet	2-jet	3-jet	≥4-jet
$t\bar{t}$ (MC)	5.1 ± 1.1	32.7 ± 5.9	74.7 ± 11.2	135.1 ± 23.0
QCD (DD)	14.4 ± 7.2	15.2 ± 7.6	10.8 ± 8.5	8.6 ± 9.4
W+jets (MC)	105.0 ± 38.8	77.1 ± 34.7	31.9 ± 18.2	15.9 ± 12.4
Z+jets (MC)	0.3 ± 0.1	1.5 ± 0.5	1.1 ± 0.5	1.5 ± 1.0
single top (MC)	12.6 ± 1.9	20.3 ± 3.0	11.8 ± 2.5	6.7 ± 1.7
dibosons (MC)	1.1 ± 0.2	1.8 ± 0.3	0.7 ± 0.2	0.2 ± 0.1
Total background	133.3 ± 39.5	115.9 ± 35.7	56.4 ± 20.3	32.9 ± 15.6
Total expected	138.4 ± 39.6	148.6 ± 36.1	131.1 ± 23.2	168.0 ± 27.8
Observed	147	133	173	156

(b)

Table 3.2: Number of events in the (a) pretag and (b) tag samples with different jet multiplicities in the electron channel. The observed number of events are shown, together with the Monte Carlo simulation estimates for $t\bar{t}$, W+jets, Z+jets and single top events, normalised to the data integrated luminosity of 35 pb^{-1} . The data driven estimates (DD) for QCD multijet (see Section 3.5.1) backgrounds are also shown. The uncertainties on data driven background estimates include the statistical uncertainty and all systematic uncertainties.

μ+jets channel, pretag				
	1-jet	2-jet	3-jet	≥4-jet
ttbar (MC)	19.3 ± 3.9	81.0 ± 12.2	161.3 ± 17.7	273.0 ± 38.2
QCD (DD)	521.6 ± 156.5	287.4 ± 86.2	121.4 ± 36.4	51.3 ± 15.4
W+jets (MC)	18994.5 ± 3983.1	4613.2 ± 1476.7	1067.7 ± 459.1	313.8 ± 197.7
Z+jets (MC)	771.0 ± 161.9	246.4 ± 78.9	69.4 ± 29.8	25.4 ± 16.0
single top (MC)	57.3 ± 6.9	63.5 ± 7.6	31.8 ± 5.7	15.0 ± 3.5
dibosons (MC)	63.3 ± 5.1	55.3 ± 4.4	16.1 ± 2.6	4.0 ± 0.8
Total background	20407.8 ± 3989.4	5265.8 ± 1481.3	1306.4 ± 461.6	409.6 ± 199.0
Total expected	20427.0 ± 3989.4	5346.8 ± 1481.4	1467.7 ± 461.9	682.6 ± 202.6
Observed	20582	5228	1356	653

(a)

μ+jets channel, tagged				
	1-jet	2-jet	3-jet	≥4-jet
$t\bar{t}$ (MC)	7.0 ± 1.5	43.1 ± 7.8	102.0 ± 15.3	192.2 ± 32.7
QCD (DD)	33.1 ± 9.9	41.4 ± 12.4	24.2 ± 7.3	13 ± 3.9
W +jets (MC)	220.7 ± 81.7	144.4 ± 65.0	58.8 ± 33.5	28.9 ± 22.5
Z +jets (MC)	7.1 ± 1.8	6.1 ± 2.1	2.7 ± 1.2	2.0 ± 1.3
single top (MC)	20.9 ± 3.1	30.5 ± 4.6	17.5 ± 3.7	9.2 ± 2.3
dibosons (MC)	1.9 ± 0.3	3.1 ± 0.6	1.2 ± 0.3	0.3 ± 0.1
Total background	283.6 ± 82.3	225.5 ± 66.4	104.5 ± 34.5	53.4 ± 23.0
Total expected	290.6 ± 82.4	268.7 ± 66.8	206.5 ± 37.8	245.6 ± 40.0
Observed	337	304	225	246

(b)

Table 3.3: Number of events in the (a) pretag and (b) tag samples with different jet multiplicities in the muon channel. The observed number of events are shown, together with the Monte Carlo simulation estimates for $t\bar{t}$, W+jets, Z+jets and single top events, normalised to the data integrated luminosity of 35 pb^{-1} . The data driven estimates (DD) for QCD multijet (see Section 3.5.1) backgrounds are also shown. The uncertainties on data driven background estimates include the statistical uncertainty and all systematic uncertainties.

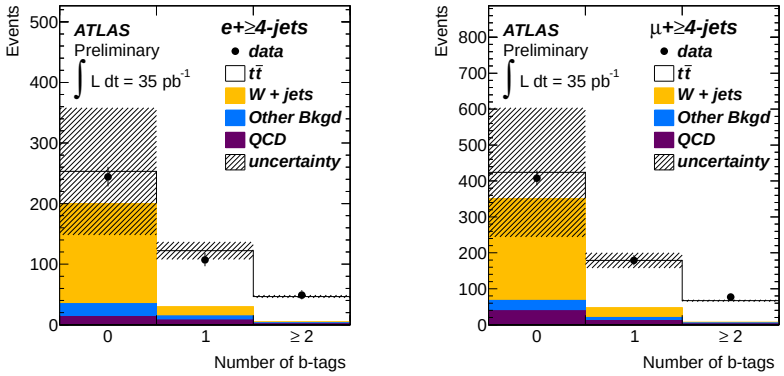

Figure 3.3: *Distribution of the number of tagged jets in events passing the selection in the electron (a) and muon (b) channel. The data are shown by the solid points, compared to the sum of all expected contributions, taken from simulations ($t\bar{t}$ signal, single top, W and Z+jets) or estimated using a data driven technique (QCD multijet). The hatched area shows the uncertainty on the total expectation due to the uncertainties on the background estimates*

- The third approach is based on the fact that W+jets production is charge asymmetric: W^+ production is enhanced with respect to W^-, because of proton PDF functions. For this background, the number of events with a positive lepton is greater than the number of events with a negative one, while the top pair production results almost in the same number of positive and negative lepton candidates. Since the charge asymmetry in the W+jet production is relatively well known, the amount of W bosons in a given sample can be estimated as

$$N_{W^+} + N_{W^-} = \left(\frac{r_{MC}+1}{r_{MC}-1}\right)(D^+ - D^-), \tag{3.5}$$

  where $D^+(D^-)$ are total numbers of events in data with positively (negatively) charged lepton, and $r_{MC} \equiv \frac{\sigma(pp\to W^+)}{\sigma(pp\to W^-)}$ is evaluated for the signal region kinematic cuts from Monte Carlo simulation.

The second approach has been found to give the most precise results, hence it is used as baseline: the W+jets background is estimated to be 160 ± 40 and 310 ± 60 in electron and muon channel respectively. The other two approaches provide a useful cross check of the results.

The relations on which the first two techniques are based are valid for the $W \to e\nu$ background in the electron channel and the $W \to \mu\nu$ background in the

muon channel. $W \to \tau\nu$ events, where the τ decays leptonically, are also a significant background. The jet multiplicity distribution in these events, after the lepton identification and kinematical cuts, is however significantly different from that of $W \to l\nu$ (with $l = e, \mu$) events. For this reason, this background is estimated separately, using the Monte Carlo simulation to predict the ratio of $(W \to \tau\nu)/(W \to l\nu)$. The charge asymmetry method treats the $W \to l\nu$ and $(W \to \tau\nu)$ backgrounds together.

This section is organized as follows. The estimation obtained with the W/Z ratio method is discussed in Section 3.3.1, while the estimate based on the Berends scaling is discussed in Section 3.3.2. Finally, the results obtained with the charge asymmetry method are described in Section 3.3.3.

3.3.1 W/Z ratio method

This approach relies on the selection of three control samples: W+1jet events and Z+1jet and Z+$\geq$4jet events.

Selection and composition of $W \to l\nu$ control sample

W+1jet event candidates are selected using the same criteria for leptons and missing energy as for the $t\bar{t}$ signal candidates. Events passing the single lepton trigger and exactly one offline reconstructed lepton are selected. In the muon channel, the transverse missing energy is required to be larger than 20 GeV and the triangular cut is applied[5]. In the electron channel, the transverse missing energy is required to be larger than 35 GeV and the transverse mass larger than 25 GeV. The W+1jet control sample is defined requiring exactly one jet with $p_{\mathrm{T}} > 25$ GeV and $|\eta| < 2.5$.

In Table 3.4 the number of selected events is reported. The number of estimated background events is also shown.

The QCD is the largest background to be subtracted from the observed number of $W \to l\nu$ candidates. It is estimated using the data driven techniques described in Section 3.5.1. The other considered backgrounds are $W \to \tau\nu$, Z, single top, top quark pair and diboson events. The expected rates are taken from the Monte Carlo simulation and the uncertainties are obtained taking into account theoretical cross section uncertainty, luminosity uncertainty and detector response effects, dominated by the JES uncertainty.

The rate of W+1jet is measured to be 8813 ± 182 for the electron channel and 18537 ± 321 for the muon channel.

Selection and composition of $Z \to ll$ control samples

Z event candidates are preselected using the same single lepton triggers used for W and signal candidates. The presence of two offline reconstructed electrons or muons,

[5] $\not\!\!E_T + m_T(W) > 60$ GeV.

Sample	1-jet pretag e	1-jet pretag μ
observed	9481	20582
multijets (DD)	287.0±143.5	521.6±156.5
$W(\tau\nu)$+jets (MC)	230.3±53.0	613.8±141.2
Z+jets (MC)	65.1±15.0	771.0±177.3
$t\bar{t}$ (MC)	14.3± 2.9	19.3± 3.9
single-t (MC)	35.7± 4.3	57.3± 6.9
diboson (MC)	35.3±2.8	63.3± 5.1
Total (non $W(l\nu)$+jets)	667.7 ± 154.1	2046.3 ± 248.6
Estimated $W(l\nu)$+jets	8813.3 ± 182.2	18535.7 ± 310.4

Table 3.4: Observed event yields in the pretag 1-jet samples and estimated contributions from non-W processes and $W \to \tau\nu$. The estimation for multijet events is data driven (DD), all other estimates are based on simulation (MC). The last row gives the number of $W(l\nu)$+jet events, estimated as the difference between the number observed events in data and all background contributions.

with $p_T > 20$ GeV, with opposite charge and with an invariant mass between 80 GeV and 100 GeV, is required.

The W/Z ratio method requires the kinematical selection on the leptons from the Z to match those applied to the charged lepton and the neutrino on W and $t\bar{t}$ signal candidates. Since these selections are different for the electron and muon channel, we also define two selections for the Z candidates. The first selection, which we call "selection A", is used to apply the W/Z ratio method to the estimation of the $W(\mu\nu)$+jets background and requires the sum of the transverse momentum of the negative lepton and the transverse mass of the two leptons to be larger than 60 GeV, in addition to the preselection cuts described above.

The second selection, used in the estimation of the $W(e\nu)$+jets background and called "selection B", requires the p_{T} of the negative lepton to be larger than 35 GeV and the transverse mass between the two leptons is required to be larger than 25 GeV.

The low jet multiplicity control samples are selected by requiring exactly one jet with $p_T > 25$ GeV and $|\eta| < 2.5$. The signal-like Z control samples require at least four jets with $p_T > 25$ GeV and $|\eta| < 2.5$.

The number of selected events in the electron and muon channel is shown in Table 3.5. The QCD background is estimated as the number of same sign leptons passing the selection. Only statistical uncertainty is quoted. The systematic one, coming from charge misidentification, has been found to be negligible.

The other backgrounds are estimated from Monte Carlo simulation and their uncertainty is obtained taking into account theoretical cross section uncertainty, luminosity uncertainty and detector response effects, dominated by the JES uncertainty.

	+1jet, sel. A	≥4jet, sel. A	+1jet, sel. B	≥4jet, sel. B
Selected events (ee)	872	15	598	9
QCD background (ee)	5 ± 2.2	0 ± 0	5 ± 2.2	0 ± 0
other backgrounds (ee)	3.2 ± 0.1	0.5 ± 0.1	2.3 ± 0.1	0.4 ± 0.1
Measured Z(ee) rate	863.8 ± 29.6	14.5 ± 3.9	590.7 ± 24.6	8.6 ± 3
Selected events ($\mu\mu$)	1669	25	1164	17
QCD background ($\mu\mu$)	0 ± 0	0 ± 0	0 ± 0	0 ± 0
other backgrounds ($\mu\mu$)	6.1 ± 0.13	1.0 ± 0.1	4.2 ± 0.1	0.7 ± 0.1
$Z(\mu\mu)$ events	1662.9 ± 40.8	24.0 ± 5.0	1159.8 ± 34.1	16.3 ± 4.1
Z(ee)+$Z(\mu\mu)$	2526.7 ± 50.5	38.5 ± 6.3	1750.5 ± 42.0	24.9 ± 5.1

Table 3.5: Number of events in the Z+1jet and $Z+$ ≥4jet control samples described in the text.

The uncertainty on the $Z+$ ≥4jet/Z+1jet ratio is dominated by the statistical uncertainty on the numerator. Since this ratio is expected to be independent of the Z decay mode, we sum the number of the $Z \to ee$ and $Z \to \mu\mu$ events for each of the two selections. The combined ratio is then

$$\frac{Z+ \geq 4j}{Z+1j} = (1.52 \pm 0.25) \cdot 10^{-2} \tag{3.6}$$

for selection A, used in the estimate of the $W(\mu\nu)$+jets background, and

$$\frac{Z+ \geq 4j}{Z+1j} = (1.42 \pm 0.29) \cdot 10^{-2} \tag{3.7}$$

for selection B, used in the estimate of the $W(e\nu)$ background.

W+jets background estimation

The expected rate of W+jets events after the requirement of at least 4 jets, but before the b-tagging requirement, has been evaluated using Eq. 3.4. The results obtained are 160 ± 40 and 310 ± 60 in electron and muon channel respectively.

The total uncertainty include the one on the measured $W(l\nu)$ and $Z(ll)$ rates, discussed above. Furthermore, the following sources of systematic uncertainty have been considered:

- The uncertainty on the C_{MC} factor in Eq. 3.4 has been evaluated from the difference between predictions obtained varying ALPGEN generator parameters, using SHERPA samples and varying the PDF set. The first component has been evaluated using ALPGEN samples with varying parameters described in Section 3.1.2. The event selection of W and Z control samples has been applied on Monte Carlo truth objects and the corresponding value of C_{MC} has been evaluated for each ALPGEN sample. The values which have been obtained

Channel	**Electron**	**Muon**
sample	C_{MC}	
default	1.20 ± 0.10	1.03 ± 0.07
δR	$1.04 - 1.05 \pm 0.06$	$0.96 - 0.99 \pm 0.05$
p_T	$0.98 - 1.14 \pm 0.08$	$0.92 - 1.07 \pm 0.07$
$ktfac$	$0.99 - 1.02 \pm 0.06$	$0.95 - 0.99 \pm 0.06$
iqopt	1.02 ± 0.05	0.98 ± 0.04

Table 3.6: Variation of $C_{\rm MC}$ parameter (Eq. 3.4) from varying various parameters of Alpgen Monte Carlo: the δR and $p_{\rm T}$ of the matching between the parton shower and matrix element calculations, while $ktfac$ and *iqopt* are related to the factorization, the renormalization and the shower scales. For each parameter variation, the range of values obtained is shown.

are reported in Table 3.6. Since the variations are within the uncertainty due to the limited Monte Carlo statistics of the samples, the RMS of the values is taken as systematic uncertainty. This uncertainty has been then added in quadrature to the difference between the nominal Alpgen and Sherpa values. This gives a total theoretical uncertainty of 12% for the electron channel and 9.4% for the muon channel. The PDF uncertainty has been found to be 3.2%.

- The effects of detector reconstruction uncertainties have been evaluated. These uncertainties affect both $C_{\rm MC}$ prediction and the estimation of backgrounds to W+1jet and Z control samples obtained from Monte Carlo. The most important one is that associated to the JES, which is about 3%.

In Table 3.7 we report the predicted number of $W \to l\nu$ events, computed according to Eq. 3.4. The $W \to \tau\nu$ contribution has been estimated from the data driven $W \to l\nu$ rate and the Monte Carlo prediction of the ratio between $W \to \tau\nu$ and $W \to l\nu$ rates, and is also reported in the table.

3.3.2 Berends scaling method

This methods relies on the selection W+1jet and W+2jet control samples in both electron and muon channel. The first one is the same used for the W to Z ratio method. For what concern the second one, it has been selected by applying the same criteria for leptons and missing energy as for the $t\bar{t}$ signal candidates and then requiring the presence of exactly two jets.

In Table 3.8 the number of selected events is reported. The number of estimated background events is also shown. The rate of W+2jet events is measured to be 2160 ± 89 for the electron channel and 4299 ± 156 for the muon channel. The measured and expected rates are in good agreement.

Channel	**Electron**	**Muon**
Estimated $W \to l\nu$	150.7	290.6
Estimated $W \to \tau\nu$	6	19
Statistical uncertainty	21%	17%
Purity of control samples	3%	2%
Theoretical uncertainties	12%	9.4%
JES	3%	3%
PDFs	3.2%	3.2%
Total W+jets background	156.7 ± 38.1	309.6 ± 61.1

Table 3.7: Number of W background events estimated using the W/Z ratio method, before the selection of at least one b-tagged jet.

Sample	2-jet pretag e	2-jet pretag μ
observed	2552	5228
multijets (DD)	123.0±61.5	287.4±86.1
$W(\tau\nu)$+jets (MC)	73.1±23.4	195.7±62.6
Z+jets (MC)	62.4±20.0	246.4±78.9
$t\bar{t}$ (MC)	61.0± 9.2	81.0±12.2
single-t (MC)	42.2± 5.1	63.5± 7.6
diboson (MC)	30.1± 2.4	55.3± 4.4
Total (non $W(l\nu)$+jets)	391.8 ± 72.9	929.3 ± 137.9
Estimated $W(l\nu)$+jets	2160.2 ± 88.7	4298.7 ± 158.5

Table 3.8: Observed event yields in the pretag 2-jet samples and estimated contributions from non-W processes and $W \to \tau\nu$. The estimation for multijet events is data driven (DD), all other estimates are based on simulation (MC). The last row gives the number of $W(l\nu)$+jet events, estimated as the observed events in data minus all other backgrounds.

The ratio between the 2 jet and 1 jet rates is measured to be

- $0.245 \pm 0.006 \pm 0.008$ for the electron channel,
- $0.232 \pm 0.004 \pm 0.004$ for the muon channel,

where the first uncertainty is statistical and the second is the systematics.

The expected rate of W+jets events after the requirement of at least 4 jets but before the b-tagging requirement has been evaluated using Eq. 3.3 and it has been found to be 180 ± 50 in the electron channel and 320 ± 70 in the muon channel.

Channel	**Electron**	**Muon**
Estimated $W \to l\nu$	172.0	301.0
Estimated $W \to \tau\nu$	7.6	19.8
Statistical uncertainty	5%	6%
Purity of control samples	18%	9%
Validity of the extrapolation	22%	19%
JES	2%	2%
Total W+jets background	179.6 ± 47.2	320.7 ± 68.1

Table 3.9: Number of W background events estimated using the Berends scaling method, before the selection of at least one b-tagged jet.

The following sources of systematic uncertainty have been considered:

- The purity of the W+jet control sample, discussed in the previous sections.
- The assumption that the (W+(n+1) jets/W+n jets) ratio is constant has been checked using the ALPGEN samples with different generator parameters described above and SHERPA samples. Systematic uncertainty is calculated as the spread around unity of the value of $(W^{\text{2jets}}/W^{\geq \text{4jets}}) \cdot \sum_{i=2}^{\infty}(W^{\text{2jets}}/W^{\text{1jet}})^i$, which has been found to be 19% in the μ channel and 22% in the e channel. The PDF uncertainty in the same quantity has been found to be 3%. The sum of these two contributions in quadrature has been considered as the total theoretical uncertainty in the validity of the extrapolation.
- The effect of the experimental uncertainties on the assumption that the (W+(n+1) jets/W+n jets) ratio is constant has also been considered. The only significant contribution comes from the JES uncertainty and it has been found to be 2%.

In Table 3.9 I report the predicted number of $W \to l\nu$ events, computed according to Eq. 3.3. The $W \to \tau\nu$ contribution has been estimated from the data driven $W \to l\nu$ rate and the Monte Carlo prediction of the ratio between $W \to \tau\nu$ and $W \to l\nu$ rates and is also reported in the table.

	1-jet pretag e	1-jet pretag μ	2-jet pretag e	2-jet pretag μ
Observed	1815	1593	404	370
QCD multijet (DD)	517 ± 89	65 ± 28	190 ± 43	20.0 ± 9.7
$W(\tau\nu)$+jets (MC)	39 ± 10	43 ± 11	11.7 ± 4.4	13.6 ± 5.1
Z+jets (MC)	19.0 ± 9.1	48 ± 12	11.6 ± 5.2	14.0 ± 4.8
$t\bar{t}$ (MC)	1.7 ± 0.8	1.7 ± 0.8	7.0 ± 3.0	7.7 ± 3.3
single-t (MC)	4.4 ± 0.7	5.0 ± 0.8	5.2 ± 0.8	5.1 ± 0.8
diboson (MC)	4.8 ± 4.8	5.7 ± 5.7	3.8 ± 3.8	4.4 ± 4.4
Total (non $W(l\nu)$+jets)	585 ± 90	168 ± 33	229 ± 44	65 ± 13
Estimated $W(l\nu)$+jets	1230 ± 100	1425 ± 52	175 ± 49	305 ± 23

Table 3.10: Observed event yields in the pretag 1-jet and 2-jet samples and estimated contributions from non-W processes and $W \to \tau\nu$. The estimation for QCD multijet events is data driven (DD), all other estimates are based on simulation (MC). The last row gives the number of $W(l\nu)$+jet events, estimated as the observed event count minus all other contributions.

The results are in good agreement with those obtained with the W/Z ratio technique.

As can be noticed from Table 3.9, this method suffers for higher systematic uncertainty with respect to the W to Z ratio method, but it enjoys a lower statistical error.

For this reason the Berends scaling method was used for the analysis on top observation performed on an integrated luminosity of 3 pb^{-1} [112]. In this paper the first ATLAS measurement of $t\bar{t}$ cross section was reported. The event selection was very similar to the one described in Section 3.2. The only differences were in looser electron identification cuts and in the use of muon channel $\not\!\!E_T$ and transverse mass cut also for electron channel. Both these cuts have been tightened in the present analysis in order to get rid of the QCD background in the electron channel. The number of selected events in W+1jet and W+2jet control region are reported in Table 3.10. As can be seen comparing this table with respect to Tables 3.9 and 3.10, the QCD contribution is indeed reduced by a factor of 10 (from 28% to 3% in the 1-jet sample and from 47% to 5% in the 2-jet sample).
The results obtained with 3 pb^{-1} are reported below:

$$W_{\text{pretag}}^{\geq 4\text{-jet}} = 11.2 \pm 2.2(\text{stat.}) \pm 4.0(\text{syst.}), \quad e \text{ channel},$$
$$W_{\text{pretag}}^{\geq 4\text{-jet}} = 18.9 \pm 4.1(\text{stat.}) \pm 5.0(\text{syst.}), \quad \mu \text{ channel}.$$

The systematic uncertainty is dominated by that on the method and on the purity of W+1jet and W+2jet control samples.

Channel	**Electron**	**Muon**
D^+	230	374
D^-	170	279
r_{MC}	1.66	1.67

Table 3.11: Numbers of candidates in the top signal region with a lepton of positive and negative charge, in the electron and muon channels, together with the value of r_{MC} used in Eq. 3.5 to estimate the W+jets background.

3.3.3 Charge asymmetry method

Since this method has been used to evaluate the normalisation of W+jets background for the top quark charge asymmetry analysis, a detailed description of this technique is reported in Section 4.3.2. In the following, only the results obtained with 2010 data are reported.

W+jets background in the signal region (≥ 4 jets) before b-tagging is extracted from Equation 3.5. The formula is valid because $N_{W^+} - N_{W^-} \approx D^+ - D^-$ to a very good approximation. Here $D^\pm$ denote the total number of events selected in the data with a positive or negative lepton and N_{W^+}, N_{W^-} are the numbers of W^+, W^- events in the signal region.
Apart from statistical uncertainty, which is the dominant one, the sources of systematic uncertainty considered are listed below.

- The uncertainty on the value of r_{MC} coming from PDF uncertainty has been estimated comparing the predictions obtained with different sets of PDFs.
- The effects of Monte Carlo modelling on the value of r_{MC} has been studied using two different MC generators: Sherpa and Alpgen.
- The effect of charge misidentification has also been investigated and found to be negligible.

The numbers of candidates in data in the signal ($\geq$ 4-jet) region with positive and negative charges, and the values of r_{MC} used for extracting the W+jets background are shown in Table 3.11. The estimated numbers of W+jets events and their uncertainties are found in Table 3.12.

As can be seen from table 3.12, this method is characterized by low systematic uncertainty, but suffers for large statistical uncertainty.

3.4 Data Driven estimate of W+jets background with b-tagging request

In principle the number of W+jets events in the tagged sample can be obtained using W to Z ratio method by selecting events with Z boson produced with at least

Channel	**Electron**	**Muon**
JES	3.6	3.6
PDF	6.3	6.2
MC generator	5.3	3.2
Total systematics	9.0	7.8
Statistical	33.2	27.0
Total W+jets background	242 ± 83	379 ± 106

Table 3.12: Relative uncertainties (expressed as percentages) in the estimate of the W+jets background before the selection of at least one b-tagged jet, using the charge asymmetry method. The estimated background is shown in the last row.

4 jets with the additional request that one of them is tagged as a b-jet. A closure test has been done on Monte Carlo simulation and results are promising. With present integrated luminosity however the method can't be used because it suffers for high statistical uncertainty. The number of $Z^{\geq 4\text{jets}}$ events observed in data after the request that one of the selected jets pass b-tagging requirement is lower than 5. Berends scaling method is affected by a lower statistical error, but the assumption that the ratio of W+n jets to W+n+1 jets is constant as a function of n is no more satisfied after the request of one b-jet.

We thus construct the W+jets estimate after b-tagging request as:

$$W^{\geq 4\text{jet}}_{\text{tagged}} = W^{\geq 4\text{jet}}_{\text{pretag}} \cdot f^{\geq 4-\text{jet}}_{\text{tagged}} \tag{3.8}$$

where the $W^{\geq 4\text{jet}}_{\text{pretag}}$ is an estimate of W+jets event count in the pretag $\geq$4-jet sample and $f^{\geq 4-jet}_{tagged}$ is the fraction of these events that will be tagged (defined as the fraction of events with one or more jets passing the b-tagging criteria).

This factor is not estimated directly from Monte Carlo, since the uncertainty of the flavor composition of $W+ \geq 4$ jets is huge, but it is calculated as:

$$f^{\geq 4-\text{jet}}_{\text{tagged}} = f^{2-\text{jet}}_{\text{tagged}} \cdot f^{\text{corr}}_{2\to\geq 4} \tag{3.9}$$

where f^{2-jet}_{tagged} is a measurement of the W+jets tag fraction in the 2-jet sample and $f^{corr}_{2\to\geq 4}$ is a correction factor that scales the fraction of tagged events in the 2-jet sample to the fraction of tagged events in the $\geq$4-jet sample, accounting for the differences in flavour composition and the corresponding event tagging probabilities. The first term is measured in data, while the second one is estimated from Monte Carlo simulation.

This technique relies on the fact that tag fraction can be measured without bias in the 2-jet sample, because of low top quark pair signal contamination, and on the fact that the ratio between the fraction of tagged events in the 2-jet sample and the fraction of tagged events in the $\geq$4-jet sample is predicted with lower uncertainty with respect to the absolute fraction in the $\geq$4-jet sample.

For $f_{\text{tagged}}^{2-\text{jet}}$ evaluation, we take the pretag yield and subtract the pretag non-W backgrounds as given in Table 3.8. This gives an estimate of the W+jets contribution in the 2-jet sample. The same is done in the tagged sample: the estimated non-W backgrounds, as shown in Tables 3.2 and 3.3, are subtracted from the measured yield after applying the tagging criteria resulting in an estimate of the W+jets contribution in the 2-jet sample after tagging. The ratio of the two represents our measurement of the fraction of tagged events in the 2-jet sample:

$$\begin{aligned} f_{\text{tagged}^{e+2-\text{jet}}} &= 0.028 \pm 0.005(\text{stat.}) \pm 0.004(\text{syst.}), \\ f_{\text{tagged}^{\mu+2-\text{jet}}} &= 0.040 \pm 0.004(\text{stat.}) \pm 0.003(\text{syst.}). \end{aligned}$$

The final ingredient, the correction factor $f_{2\to4}^{\text{corr}}$, is defined as $f_{2\to\geq4}^{\text{corr}} = f_{\text{tagged}}^{\geq4-\text{jet}} / f_{\text{tagged}}^{2-\text{jet}}$. It is obtained from simulation studies on ALPGEN W+jets events and is determined to be:

$$f_{2\to4}^{\text{corr}} = 2.8 \pm 0.8(\text{syst.}), \quad e \text{ channel}, \tag{3.10}$$

$$f_{2\to4}^{\text{corr}} = 3.2 \pm 0.9(\text{syst.}), \quad \mu \text{ channel}. \tag{3.11}$$

The following assumptions were made for the determination of this correction factor and its associated uncertainties (which are assumed to be Gaussian):

- A 100% uncertainty on the W+bb+jets and W+cc+jets fractions and a 40% uncertainty on the W+c+jet fraction is used on the prediction by ALPGEN in the 2-jet bin, from the studies reported in [139]. These uncertainties are fully correlated between W+bb+jets and W+cc+jets and uncorrelated with W+c+jet.

- The uncertainty on the scaling factors for the efficiency of b-tagging for b, c and light jets as listed in Section 3.2.3 is assumed. This translates approximately to the same uncertainties on the event tagging probabilities for W+bb+jets, W+cc+jets and W+c+jets, and W+light jets in the 2-jet and $\geq$4-jet bins. These uncertainties are fully correlated between W+bb+jets, W+cc+jets and W+c+jets and uncorrelated with W+light jets. The tag fractions are measured separately for the 2-jet and 4-jet bin and an additional 20%/100% uncertainty is assumed on the ratio of these fractions for the heavy flavor and light jet components, respectively.

- The uncertainty on the ratio of fractions of in the 2-jet bin and the $\geq$4-jet bin for W+bb+jets, W+cc+jets and W+c+jets, is estimated by the variation of several ALPGEN generator parameters that are known to influence this ratio, such as the scale factor for the CKKW α_s scale. The correlation between these sources of uncertainty has been taken from ALPGEN prediction. Conservatively, these uncertainties are increased by a factor of two and add up to 40%-60% per ratio.

The leading uncertainty on $f_{2\to4}^{\text{corr}}$ is due to the last effect, the uncertainty of the predicted ratios of flavour fractions in the 2-jet and 4-jet bin due to ALPGEN variations. The errors on the uncertainty of the flavour composition in the 2-jet bin, while large by itself, are small on $f_{2\to4}^{\text{corr}}$ due to effective cancellations in the ratio.

Applying Equations (4.6) and (3.9), the estimated yields for W+jets in the $\geq$4-jet tagged samples are

$$W_{\text{tagged}}^{\geq 4\text{jet}} = 12.2 \pm 4.0(\text{stat.}) \pm 3.6(\text{syst.}), \quad e \text{ channel},$$
$$W_{\text{tagged}}^{\geq 4\text{jet}} = 39.5 \pm 8.4(\text{stat.}) \pm 11.7(\text{syst.}), \quad \mu \text{ channel}.$$

3.5 Estimate of the other backgrounds

In this section the evaluation of the other background processes is discussed. In section 3.5.1 the data driven estimate of QCD background is presented, while in section 3.5.2 some details about the estimate of the other backgrounds and the related uncertainties are given.

3.5.1 Data Driven estimate of QCD background

As already discussed, multijet events are expected to contain neither isolated leptons nor $\not\!\!E_T$. However, they are present in the selected samples due to the imperfect reconstruction in the detector. Non-isolated leptons coming from the semi-leptonic decay of a b-jet, or from the decay-in-flight of a $\pi^{\pm}$ or K meson can in few cases pass isolation cuts. As a consequence they can simulate an isolated electron or muon coming from a W boson. In addition fake electrons can come from photon conversions and hadrons. In the following prompt isolated leptons from W and Z decays are referred to as "real leptons", while those where the leptons are either non-isolated or result from misidentification of photons/jets are referred to as "fake leptons".

The μ+jets channel

This background is estimated with the matrix method (MM) extensively used at the Tevatron. This technique exploits differences in lepton identification-related properties between real and fake leptons. For this purpose, two samples are defined after requiring the final kinematic selection criteria, differing only in the lepton identification cuts: a "tight" sample and a "loose" sample, the former being a subset of the latter. The tight selection typically employs the final lepton identification criteria used in the analysis. 'Loose' muons are selected applying all standard muon identification cuts except for calorimeter and track isolation requirements.

The method assumes that the number of selected events in each sample (N^{loose} and N^{tight}) can be expressed as a linear combination of the numbers of events with real and fake leptons, in such a way that the following system of equations can be defined:

$$\begin{aligned} N^{\text{loose}} &= N^{\text{loose}}_{\text{real}} + N^{\text{loose}}_{\text{fake}}, \\ N^{\text{tight}} &= \epsilon_{\text{real}} N^{\text{loose}}_{\text{real}} + \epsilon_{\text{fake}} N^{\text{loose}}_{\text{fake}}, \end{aligned} \tag{3.12}$$

where $\epsilon_{\text{real}}(\epsilon_{\text{fake}})$ represents the probability for a real(fake) lepton that satisfies the loose criteria, to also satisfy the tight ones.

Efficiencies ϵ_{real} and ϵ_{fake} have been estimated in control samples. Real lepton efficiency has been evaluated using tag and probe method in $Z \to \mu^+\mu^-$events in data. Fake lepton efficiency has been measured in two control regions, dominated by background contribution. The first one is selected by requiring low transverse mass $m_{\text{T}}(W) < 20$ GeV and reversed triangular cut $\not\!\!E_T + m_{\text{T}}(W) < 60$ GeV. The second one is obtained by requiring low missing transverse energy. Contribution of real leptons is subtracted using SM prediction in the former case and an iterative process in the latter case. For what concern the selection that uses b-tagging requirement, the control region used for ϵ_{fake} estimation is selected asking that at least one jet in the event satisfies b-tagging criteria and matrix method is applied on the tagged sample.

The system of equations in Eq. 4.2 can be solved yielding the estimated number of events with a fake lepton in the tight sample:

$$N^{\text{tight}}_{\text{fake}} = \frac{\epsilon_{\text{fake}}}{\epsilon_{\text{real}} - \epsilon_{\text{fake}}} (N^{\text{loose}} \epsilon_{\text{real}} - N^{\text{tight}}) \tag{3.13}$$

The predictions obtained using the two different control regions for fake rate measurement shows an excellent agreement between each other.

Table 3.13 summarizes yields of multijet events in the pretag and tagged samples in the μ+jets channel. A conservative systematic uncertainty of 30% has been assigned to the estimations, from closure tests done on Monte Carlo QCD samples.

channel	selection	nj=1	nj=2	nj=3	nj ≥ 4
μ+jets	pretag	521.6±156.5	287.4±86.1	121.4±36.3	51.3±15.4
μ+jets	tagged	33.1±9.9	41.4±12.3	24.2±7.2	13.0±3.9

Table 3.13: Number of multijet events predicted by the matrix method in the μ+jets channel as a function of jet multiplicity.

The e+jets channel

In the electron channel the multijet background has comparable contributions from heavy flavour decays, photon conversions and jets with high electromagnetic fraction.

This makes the use of a matrix method more difficult than in the muon channel. Instead, the hadronic leakage cut used in the electron identification is inverted to obtain a model of the multijet background shape. The most sensitive distribution to fake electrons contribution is the $\not\!\!E_T$ one. The background coming from fake leptons is determined in each multiplicity bin by performing a fit in the low $\not\!\!E_T$ region ($\not\!\!E_T < 35$ GeV), which is not used for the analysis. QCD background estimate after b-tagging is obtained by applying the same procedure to the tagged selected sample.

Tab. 3.14 summarizes yields of multijet events in the pretag and tagged samples in the e+jets channel. For $nj = 3$ and $nj \geq 4$ tagged samples, uncertainty is dominated by the limited statistics, which is applied as systematic uncertainty in the analysis. For all other bins a systematic uncertainty of 50% has been assigned coming from the comparison of the estimated QCD fraction with the predictions of alternative models. These models are constructed by inverting other selection cuts, instead of the hadronic leakage. All these models suffer from limited statistics, but they provide consistent results with the default model within 50%.

channel	selection	nj=1	nj=2	nj=3	nj ≥ 4
e+jets	pretag	287±143	123±62	62±31	22±11
e+jets	tagged	14.4±7.7	15.2±7.6	10.8±8.6	8.6±9.4

Table 3.14: Number of predicted multijet events as a function of jet multiplicity.

3.5.2 Other backgrounds

All the other background processes have been estimated from Monte Carlo simulation. Some details about the samples used are reported in Section 3.1.2. The uncertainty is obtained by summing up in quadrature the contribution coming from 3 main sources:

- uncertainty on the measured integrated luminosity, which is 3.2 %,
- theoretical uncertainty on the cross section of each process,
- uncertainty coming from detector effects, dominated by the JES uncertainty.

Figure 3.4 shows W transverse mass distribution for 2-jet pretag sample and figure 3.5 shows hadronic top mass in signal sample. Data are well described by Monte Carlo predictions summed up with data driven QCD.

3.6 Signal acceptance

The total efficiency for signal events to pass the event selection criteria (the acceptance) is estimated from simulation and used together with the value of the

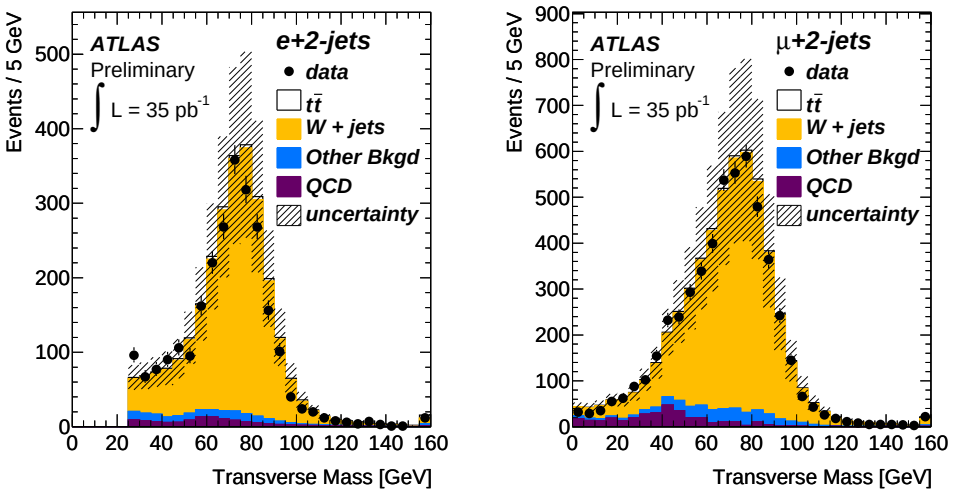

(a) (b)

Figure 3.4: *Transverse mass of the W boson in events with exactly two jets for the electron (a) and muon (b) channel. The QCD multijet background is obtained from the data driven methods described in the text, while all the other backgrounds and ttbar are obtained from Monte Carlo simulation. The uncertainty on the Monte Carlo and data driven predictions are shown.*

integrated luminosity to extract the total cross section. Table 3.15 shows a detailed list of the sources of systematic uncertainty affecting the signal acceptance. Uncertainties coming from detector reconstruction effects have been already discussed in Section 3.2.3, while in Section 3.1.2 the Monte Carlo samples used to evaluate the uncertainty coming from ISR/FSR, the choice of NLO and PS generator and PDF set have been presented.

3.7 Cross section results

The $t\bar{t}$ cross section is extracted using the formula:

$$\sigma(t\bar{t}) = \frac{N_{sig}}{L \times \epsilon} = \frac{N_{obs} - N_{bkg}}{L \times \epsilon} \tag{3.14}$$

where N_{obs} is the number of events in data that pass all selection cuts, N_{bkg} is estimated background contribution, L represents data integrated luminosity and ϵ is signal acceptance discussed in the previous section.

rel.uncertainty(%)	e+jets	μ+jets
lepton trigger, reconstruction and selection	±3.6	±0.9
JES	+9.0/-9.1	+7.8/-8.7
jet energy resolution	±0.2	±0.2
jet reconstruction efficiency	±2	±2
electron energy scale	+0.2/-0.6	0
electron energy resolution	±0.2	0
muon momentum scale	0	±0.3
muon momentum resolution	0	±0.1
ISR/FSR	+7.0/-9.6	+4.8/-9.3
NLO generator (MC@NLO *v.s.* POWHEG)	±6.6	±5.0
Parton Shower generator (HERWIG *v.s.* PYTHIA)	±4.6	±3.8
PDFs	±1.7	±1.4
Pile up	-1.2	-1.2
TOT	+19.2 -15.3	+15.0 -15.3

(a) pretag

rel.uncertainty(%)	e+jets	μ+jets
b/c-tagging efficiency	+9.1/-10.4	+9.2/-10.5
light jets tagging efficiency	±0.2	±0.2
lepton trigger, reconstruction and selection	±3.6	±0.9
JES	+8.9/-9.0	+7.6/-8.5
jet energy resolution	±0.4	±0.4
jet reconstruction efficiency	±3	±3
electron energy scale	+0.2/-0.6	0
electron energy resolution	±0.2	0
muon momentum scale	0	±0.3
muon momentum resolution	0	±0.1
ISR/FSR	+7.2/-8.2	+6.3/-7.7
NLO generator (MC@NLO *v.s.* POWHEG)	±6.5	±2.7
Parton Shower generator (HERWIG *v.s.* PYTHIA)	±4.6	±3.8
PDFs	±1.9	±1.6
Pile up	-0.6	-0.8
TOT	+14.4 -19.9	+16.1 -15.5

(b) tagged

Table 3.15: Contributions to the uncertainty on the estimated $t\bar{t}$ signal acceptance ϵ, for electron and muon channels separately, before (a) and after (b) b-tagging, expressed as relative percent uncertainty.

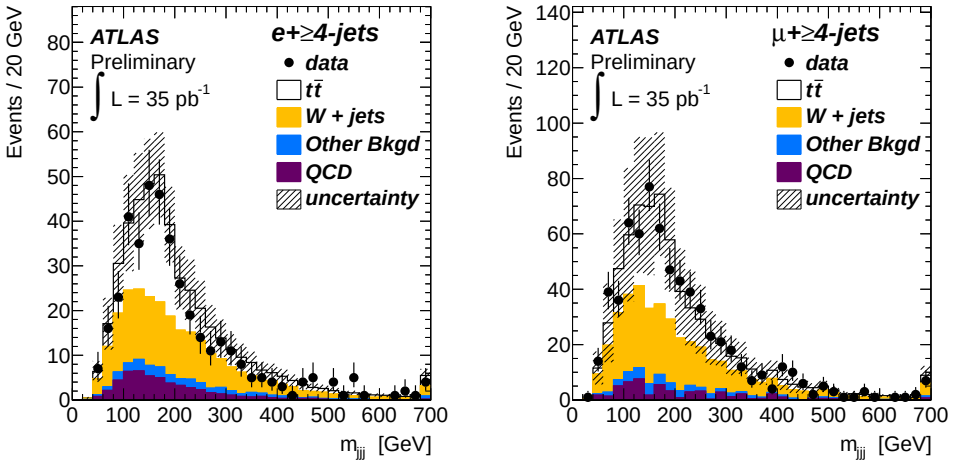

(a) (b)

Figure 3.5: *Distribution of the invariant mass m_{jjj} of the three jets with the highest vector sum p_{T} for the events passing the baseline event selection in the electron (a) and muon (b) channel. The QCD multijet background is obtained from the data driven methods described in the text, while all the other backgrounds and ttbar are obtained from Monte Carlo simulation. The uncertainty on the Monte Carlo and data driven predictions are shown.*

For the multijet and the W+jets backgrounds the data driven estimates described in Sections 3.5.1, 3.3 and 3.4 are used. For the expected background coming from Z+jets, single top and diboson production simulation estimates are used.

The resulting yields for N_{bkg} and $N_{sig} = N_{obs} - N_{bkg}$ are listed in table 3.16. W+jets contamination is also quoted separately, since it is the dominant background and it is a significant contribution to cross section uncertainty, the dominant one in the pretag sample.

The quoted uncertainty for N_{bkg} is the total uncertainty; the uncertainty on N_{sig} is the sum in quadrature of the background uncertainty and the statistical uncertainty on N_{obs}.

The measured values for the cross section for electron and muon channels for both pretag and tagged samples, including the statistical and all the systematic uncertainties, are shown in table 3.17. The list of uncertainties is reported in Table 3.18.

A Bayesian approach has been used to extract top quark pair cross section and relative uncertainty for each channel, since it allows a straightforward treatment of the systematic uncertainties.

Component	pretag	tagged
$e - N_{sig}$	189.7 ± 45.9	126.8 ± 16.6
$e - N_{bkg}$	210.3 ± 41.3	29.2 ± 10.9
$e - N_{bkg}$ (W+jets only)	156.7 ± 38.1	12.2 ± 5.3
$\mu - N_{sig}$	247.8 ± 69.9	182.0 ± 21.8
$\mu - N_{bkg}$	405.2 ± 65.1	64.0 ± 15.2
$\mu - N_{bkg}$ (W+jets only)	309.6 ± 61.1	39.5 ± 14.4

Table 3.16: Estimated yield of $t\bar{t}$ signal events and background events in the pretag and b-tagged 4-jet inclusive bin for electrons and muons.

Channel	XS [pb]
e - pretag	$159 \pm 17\ ^{+50}_{-44} \pm 5$
μ - pretag	$148 \pm 16\ ^{+47}_{-47} \pm 5$
e - tagged	$153 \pm 16\ ^{+41}_{-27} \pm 6$
μ - tagged	$159 \pm 14\ ^{+35}_{-27} \pm 6$

Table 3.17: Estimated inclusive $t\bar{t}$ cross sections. The errors represent the statistic, and combined systematic and luminosity uncertainty respectively.

Bayesian statistics is based on the Bayes' theorem:

$$P(theory|data) \simeq P(data|theory) \cdot P(theory) \tag{3.15}$$

where $P(theory)$ is the "prior" probability, which reflects the experimenter's degree of belief that the theory is correct before carrying the measurement; $P(data|theory)$ is the probability to have gotten the data actually obtained, given the theory (also called "likelihood"); $P(theory|data)$ is the "posterior" probability, which represents the probability that the theory is true after the measurement. Equation 3.15 is stated as proportionality, since the probability must be normalised by summing (or integrating) over all possible hypothesis.

In this particular case, a joint likelihood is constructed including the dependence of the cross section from the uncertainties. The joint probability density function (*pdf*) is the product of this likelihood times the prior. A flat prior is used for the signal cross section, while Gamma functions are used for the systematics. To find the pdf for the cross section parameter only, the joint pdf is integrated (marginalisation) over all the other parameters. The posterior pdf of the cross section is then obtained by solving the Bayes formula:

Source	$\Delta\sigma(e)/\sigma$[%] pretag	$\Delta\sigma(\mu)/\sigma$[%] pretag	$\Delta\sigma(e)/\sigma$[%] tagged	$\Delta\sigma(\mu)/\sigma$[%] tagged
Statistical error	10.4	10.2	9.9	8.6
Object selection				
Lepton Reco,ID,Trigger	+3.8/-3.5	+1.0/-0.9	+3.8/-3.5	+1.0/-0.9
Jet energy Reco	+14.1/-11.8	+14.5/-12.3	+11.4/-9.6	+9.9/-8.5
b-tagging	-	-	+11.7/-8.4	+11.7/-8.4
Background rate				
QCD norm	4.4	6.1	6.2	0.7
W+jets norm	19.5	23.4	4.1	7.7
Other bkg norm	5.7	6.1	0.7	0.7
Signal simulation				
ISR/FSR	+10.6/-6.5	+10.3/-4.6	+8.9/-6.7	+8.3/-5.9
PDF	1.7	1.4	1.9	1.6
Parton Shower	+4.8/-4.4	+4.0/-3.7	+4.8/-4.4	+4.0/-3.7
NLO generator	+7.1/-6.2	+5.3/-4.8	+7.0/-6.1	+2.8/-2.6
Pile-up	1.2	1.2	0.6	0.8
Integrated Luminosity	+3.8/-3.6	+3.8/-3.6	+3.5/-3.3	+3.5/-3.3

Table 3.18: Summary of individual systematic uncertainties contribution to the cross section determination using the counting method. All numbers are relative errors expressed as percentage.

$$f(\sigma|N_{obs}) = \frac{P(N_{obs}|\sigma)f_0(\sigma)}{\int_0^\infty P(N_{obs}|\sigma)f_0(\sigma)d\sigma} \tag{3.16}$$

$$P(N_{obs}|\sigma) = \frac{\mu^{N_{obs}}e^{-\mu}}{N_{obs}!} \tag{3.17}$$

$$\mu = N_{sig} + N_{bg}$$

$$N_{sig} = \sigma L \epsilon \mathcal{B}$$

where a Poissonian likelihood has been considered and N_{obs} is the number of events surviving the analysis selection, N_{sig} and N_{bg} are the number of signal events and the expected SM background, L is the integrated luminosity, ϵ the signal efficiency and $\mathcal{B}$ the BR of the channel under consideration.

For each channel, the most probable value of the posterior has been taken as a representative value for the cross section and its uncertainty.

The results obtained in the four channels are fully compatible within the uncertainty, which is already dominated by systematics. The largest systematic for the pretag samples comes from the W+jets background normalisation. This systematic

is less important for the tagged sample, since b-tagging request significantly reduce the W+jets contamination. The use of the b-tagging information introduce however an additional 12% uncertainty. Other important contributions for all the channels come from ISR/FSR and JES.

The combination of two different channels (electron and muon in our case) is performed by replacing the previous likelihood with the joint one that depends on the *common* systematics and the systematics specific of each channel. The posterior pdf for the signal cross section obtained in this way fully includes the sources of systematic uncertainties and their correlations.

The most probable values of the posterior have been taken as a representative value for the combined cross sections and their uncertainty and they are reported in Table 3.19

The final result turns out to be:

$$\sigma_{t\bar{t}} = 154^{+49}_{-45}\text{pb}.$$

for the selection without b-tagging, and

$$\sigma_{t\bar{t}} = 156^{+36}_{-30}\text{pb}.$$

for the selection with b-tagging. The error accounts for statistical, systematic and luminosity related uncertainties.

Channel	XS [pb]
pretag combined	$154 \pm 11\ ^{+48}_{-43} \pm 5$
tagged combined	$156 \pm 10\ ^{+34}_{-28} \pm 6$

Table 3.19: Estimated inclusive $t\bar{t}$ cross sections. The errors represent the statistic, and combined systematic and luminosity uncertainty respectively.

Chapter 4

Measurement of top quark charge asymmetry

This chapter is dedicated to the description of the measurement of the top quark charge asymmetry, which has been introduced in Section 1.4.2. The results presented in the following have been documented in a conference note of the ATLAS experiment [141], in an internal report [142] and presented in several conferences (e.g. [143]). Furthermore a paper is in preparation.

The analysis has been performed in the semileptonic channel, since it enjoys a good branching ratio, 34.3%, and a clear signature. These events are characterized by the presence of one isolated lepton (electron or muon[1]), missing transverse energy and jets, some with b flavour.

As already explained in Chapter 1, the charge asymmetry would show up at the LHC in the fact that the top quark rapidity distribution is broader than the antitop quark one. A sensible variable is therefore the difference between absolute values of top and antitop quark rapidities and the observable that has been used is defined as:

$$A_C(\Delta|y|) = \frac{N(\Delta|y| > 0) - N(\Delta|y| < 0)}{N(\Delta|y| > 0) + N(\Delta|y| < 0)} \tag{4.1}$$

where $\Delta|y| = |y_t| - |y_{\bar{t}}|$, y_t ($y_{\bar{t}}$) is the top (antitop) rapidity and $N(\Delta|y| > 0)$ is the number of events in which $\Delta|y|$ is positive, while $N(\Delta|y| < 0)$ is the number of events in which $\Delta|y|$ is negative.

The QCD NLO prediction for this asymmetry obtained using the Standard Model (SM) $t\bar{t}$ signal sample (generated with MC@NLO) is $A_C^{pp} = (0.60 \pm 0.03)\%$ at the parton level; the uncertainty reported comes from available Monte Carlo (MC) statistics.

[1]As already explained in Chapter 3, small contributions to $W \to \ell$ from $W \to \tau \to \ell$ are included. Events in which one W decays hadronically and the other one in an hadronically decaying $\tau + \nu$ have been not considered, since τ-jets are significantly different from electrons and muons.

Significant enhancements are foreseen by some Beyond the Standard Model (BSM) theories as already explained in Section 1.4.2. Deviations from the SM predictions can be therefore a hint of new physics.

Within this analysis I have contributed to the choice of the selection cuts and of the observable used for this measurement. Then I have studied the impact of acceptance and detector resolution effects on the asymmetry and finally I have focused on the evaluation of the systematic, mainly the contribution of the signal modelling uncertainty.

This chapter is organized as follows. After the description of the data and the Monte Carlo samples used for this analysis, in Section 4.2 the object and the event selection cuts are presented. Section 4.3 is dedicated to the description of background estimation techniques. The reconstruction of top and antitop quark directions is then detailed in Section 4.4 and the use of an unfolding technique to correct for detector resolution and acceptance effects is discussed in Section 4.5. After that, the most important systematic uncertainties affecting this measurement are detailed in Section 4.6 and the final results and the future prospects for this analysis are reported in Section 4.7.

4.1 Data samples

4.1.1 Data

Data used for this analysis have been collected by the ATLAS detector in the period from March 2011 to June 2011. As explained in section 2.4.2 only data satisfying specific quality requirements are considered. The ATLAS Top Working Group selects events with stable beams and in which green flags are set for all the objects involved in the top quark pair events selection: trigger, electrons, muons, missing energy, jets and b-tagging. The data used for this analysis correspond to an integrated luminosity of $(0.70 \pm 3.7\%)$ fb^{-1} [144].

Since the selected events are characterized by the presence of an energetic muon or an energetic electron, the so called "Egamma" and "Muon" streams have been considered. The triggers used in the analysis are described in detail in Section 4.2.2 for both electron and muon channel.

The Pile-up conditions have varied during data taking. The Monte Carlo samples have been reweighted in order to reproduce the distribution of the number of extra vertexes in data.

4.1.2 Monte Carlo

The list of the Monte Carlo samples used in this analysis is almost identical to the one presented in Section 3.1.2. With respect to the samples used to model 2010 data, the statistics at generator level have been increased (in the majority of cases) and changes in pile-up simulation have been done. A single pile-up configuration

corresponding to the LHC running with 50 ns bunch separation has been used. The average number of extra vertexes is 8.

4.2 Selection of signal events

4.2.1 Object selection cuts

The object selection cuts are almost identical to the ones applied for the top cross section analysis and described in the Chapter 3. Different cuts have been implemented for electron selection: p_{T} threshold have been raised from 20 to 25 GeV, because of an increase in 2011 of the trigger threshold. In addition, the electron isolation energy has been corrected not only for lateral leakage, but also for pile-up contribution. The leakage and pile-up corrected isolation energy is then required to be lower than 3.5 GeV and not 4 GeV.

The 30^{th} of April, six of the front end boards (FEBs) of the Liquid Argon (LAr) calorimeter became inoperative due to a problem with a Controller Board. They were then repaired at the beginning of July 2011. A significant fraction of data is affected by this problem ($\sim$ 530 pb^{-1}). The most affected physics objects are electrons and jets. If an electron falls in the region of the dead FEBs it will be probably not identified or selected, while jets energy will be mismeasured. To avoid the presence of mismeasured objects in data and to model the problem in Monte Carlo, events with a jet with $p_{\mathrm{T}} > 20$ GeV within $\Delta R = 0.1$ from the LAr hole have been discarded and electrons that fall into the hole have been removed from the event[2]. These cuts have been applied on the data runs affected by the LAr problem and on a fraction of Monte Carlo corresponding to the integrated luminosity of influenced data.

4.2.2 Event selection cuts

Signal events have been selected using cuts very similar to the ones applied for the top quark pair cross section measurement. The list is very briefly reported below.

- Events have been selected online asking an electron or muon trigger to have fired. The muon trigger selects at Level1 regions of interest in the Muon Spectrometer with at least 10 GeV of estimated transverse momentum. The Level2 and event filter then require a muon with $p_{\mathrm{T}} > 18$ GeV, combining both Muon Spectrometer and Inner Detector information. Electron trigger is seeded by a Level1 item, that asks the presence of an electromagnetic cluster of $E_T > 14$ GeV. High level triggers impose some cuts on shower shape of the candidate electron and the presence of an associated track. The E_T threshold

[2]For each event with an electron in the hole, $\not\!\!E_T$ has been recalculated dropping the electron energy contribution.

is raised to 20 GeV. The efficiency plateau for this trigger is reached at 25 GeV and so the offline p_{T} cut has been increased from 20 to 25 GeV.

- The presence of a primary vertex, with at least 4 tracks associated to it, has been required to improve the rejection of non-collision background.
- Events with a bad jet (see Section 3.2.2 for definition) with $p_{\mathrm{T}} > 20$ GeV, coming from out-of-time energy deposits or calorimeter noise have been discarded.
- Cuts to get rid of LAr calorimeter defects have been imposed.
- The event should have exactly one electron (muon) with $p_{\mathrm{T}} > 25$ GeV ($p_{\mathrm{T}} > 20$ GeV), that has a matching with the object of the fired trigger.
- The existence of a second lepton has been vetoed.
- Missing transverse energy has been required to be > 35 GeV (> 20 GeV) in the electron (muon) channel.
- It has been asked: $m_T(W) > 25$ GeV in the electron channel and $\not\!\!E_T + m_T(W) > 60$ GeV in the muon channel, where $m_T(W)$ is the transverse mass of the selected lepton and $\not\!\!E_T$.
- The presence of at least four identified jets with $p_{\mathrm{T}} > 25$ GeV has been required.
- In addition, at least one jet which is b-tagged using the SV0 algorithm with a weight corresponding to 50% efficiency ($w > 5.85$), has been required to further improve the signal to background ratio.

The final number of events for both expectation and measured data in both channels after the event selection can be found in Table 4.1. Pretag events have been selected applying all selection cuts apart from the request of a b-tagged jet. For tagged events selection, the identification of a b-jet has been asked. As can be seen from the table, this additional request enable to significantly reduce the two main backgrounds, coming from W+jets and QCD events.

Very good agreement between the data and the signal+background expectation has been observed for both electron and muon channel in pretag and tagged samples.

The number of events in the electron channel is significantly lower than in the muon channel due to the higher lepton p_{T} requirement and the more stringent $\not\!\!E_T$ and m_T cuts.

Channel	μ + jets pretag			μ + jets tagged			e + jets pretag			e + jets tagged		
$t\bar{t}$	4784	±	5	3247	±	4	3293	±	4	2218	±	4
Single top	306	±	2	171	±	2	219	±	2	124	±	2
Z+jets	632	±	7	43	±	2	535	±	7	35	±	1
Diboson	90	±	2	8	±	1	56	±	1	4.9	±	0.4
W+jets	5740	±	920	490	±	230	3440	±	630	310	±	140
QCD	1100	±	550	230	±	230	670	±	330	84	±	84
Total background	7900	±	1100	940	±	330	4910	±	710	560	±	170
Signal + background	12700	±	1100	4190	±	330	8200	±	710	2780	±	170
Observed			12705			4392			8193			2997

Table 4.1: Observed number of data events compared to the expected number of Monte Carlo signal events and different background contributions for pretag and tag samples. Both QCD and W+jets have been estimated using data driven methods (see Section 4.3). The quoted uncertainties are statistical only except for W+jets and QCD backgrounds, where the systematic uncertainty on the normalisation is included.

4.2.3 Systematic uncertainty related to selection cuts

Monte Carlo predictions have been used to estimate some of the background contributions and to correct the asymmetry measurement for detector resolution and acceptance effects. In order to reproduce in Monte Carlo object selection efficiencies, scales and resolutions of real data, scale factors and smearings have been applied to the simulated samples, as already explained in Section 3.2.3.

The impact on the final uncertainty has been obtained varying the various scale factors and object energy scales within their uncertainties. In the following a brief recall of the most important contributions is given.

Lepton systematics

Electron and muon scale factors for trigger, reconstruction and identification[3] have been studied comparing $Z \to e^+e^-(\mu^+\mu^-)$ candidate events in data with simulated samples.

For what concerns electrons, the trigger scale factor (SF_{trig}) has been measured in 18 bins of electron $|\eta|$: it has been found $SF_{trig}(\eta) \simeq 1$ within 2% for all but the very forward ($|\eta| > 2$) region. The electron reconstruction efficiency, including track quality cuts, has been measured in three $|\eta|$ regions and the scale factor has been found to be consistent with 1 except for $|\eta| > 2.37$, where it is $\simeq 0.97$. The electron identification efficiencies and scale factors have been measured in 18 η bins (plus 2 for the calorimeter gaps) and 6 E_T bins.

[3]Reconstruction efficiency refers to standard object selection cuts proposed by performance groups, while identification efficiency refers to top-analysis specific selection cuts.

For what concern muons, a bug affecting trigger simulation in Monte Carlo has been found. The misconfiguration is not present in the data. Due to this, no trigger request has been applied on the simulated events, but the total number of selected events has been rescaled for the trigger efficiency measured in the data with tag and probe techniques. The reconstruction scale factors have been calculated as a function of muon p_{T}, while the identification efficiency has been found to be constant and equal to 1.0008 ± 0.0003 (stat) ± 0.0003 (syst).

The uncertainty on these quantities include statistical and systematic uncertainties. The most important contributions to systematic uncertainty come from the dependence on the Z mass window cut, background subtraction procedure to Z sample in data and the dependence on the choice of lepton quality cuts.

The accuracy of lepton momentum scale and resolution in simulation has been checked using the reconstructed distributions of the Z mass, as reported in [95] and [136]. Small discrepancies have been found in data and Monte Carlo resolution. As a results of these studies, functions for smearing the lepton p_{T}, as a function of its p_{T} and η have been provided. The effect of the lepton energy scales has been evaluated taking also into account the repercussion on the missing transverse energy. Since $\not\!\!E_T$ is obtained as the negative sum of all energy deposits in the detector, a change in the energy of a reconstructed object will directly translate in a variation of $\not\!\!E_T$ value. For each event, $\not\!\!E_T$ has been then re-calculated using the rescaled lepton energy instead of the original one.

Furthermore electron energy scale is corrected in the data at analysis level, in order to reproduce Z boson mass peak.

Jet systematics

The calorimeter jet reconstruction efficiency [145][146] has been derived using a tag and probe technique, starting from the jets built from charged tracks in the Inner Detector system. The reconstruction efficiency has been defined as the fraction of probe track-jets matched to a calorimeter jet. The uncertainty on the observed difference between data and Monte Carlo is about 2%. The jet energy resolution has been measured with the di-jet balance [147] and it has shown to agree between data and Monte Carlo within 2%. The uncertainty has been propagated to Monte Carlo by smearing the jet transverse momentum.

The jet energy scale (JES) uncertainty is based on the estimate performed in 2010 data [148] except for the pile-up contribution which has been re-evaluated with 2011 collisions. For jets within the acceptance, the JES uncertainty varies from 4% to 8%. The pile-up uncertainty in the central region $0 < \eta < 2.1$ accounts for 5% for jets within $20 < p_T < 50$ GeV and 2% in the range $50 < p_T < 100$ GeV. For forwards jets within $2.1 < \eta < 4.5$ the estimated pile-up uncertainty is 7% for jets within $20 < p_T < 50$ GeV and 3% in the range $50 < p_T < 100$ GeV. An additional uncertainty of 2.5% has been considered for b-tagged jets of p_T above 25 GeV. The total JES uncertainty has been obtained as the sum in quadrature of all

p_{T} range $[GeV]$	SF	uncert
20 - 30	0.831	0.091
30 - 60	0.906	0.061
60 - 90	0.934	0.145
90 - 140	0.848	0.104
140 - 200	0.848	0.163

Table 4.2: b-tagging efficiency scale factor (SF) and the total uncertainties including statistical and systematical contributions. The scale factor for c-jets has been assumed to be the same as for the b-jets but with the uncertainty doubled.

these contributions.

$\not\!\!E_T$ systematic

The most significant sources of uncertainty related to the $\not\!\!E_T$ come from the scale and resolution of the objects, the description of the pile-up events and the impact of hardware failures.

Each of the objects in the $\not\!\!E_T$ calculation has an uncertainty related to the scale and the resolution of its energy or p_T. For the electrons, high p_{T} jets and muons, the uncertainties on their scale and resolution have been propagated into the $\not\!\!E_T$: after a change in their energy or p_T, $\not\!\!E_T$ has been recalculated subtracting the old object $p_{x(y)}$ and adding the new one.

Preliminary studies at low energies have also indicated that there discrepancies between data and Monte Carlo in the low $\not\!\!E_T$ that are consistent with coming from pile-up. These effects are observed in the jet and `CellOut` (which includes all contributions not associated to reconstructed objects) terms. For the jets, the effect of pile-up is already included in the JES uncertainty. For `CellOut` term, both the x and y components of the $\not\!\!E_T$ are shifted by $\pm 10\%$ to account for this discrepancy.

b-tagging systematics

Tagging and mistag efficiency scale factors have been determined comparing b-tagging performance in various data samples to the one in the corresponding Monte Carlo samples. The obtained scale factors and their uncertainties are given as a function of jet η and p_{T} in Table 4.2 for tagging efficiencies and in Table 4.3 for mistag.

LAr hole systematics

As already mentioned at the beginning of the chapter, a large fraction of data is affected by the LAr hole problem. To avoid the presence of mismeasured objects in data and to model the problem in Monte Carlo, events with a jet with $p_{\mathrm{T}} > 20$

p_{T} range $[GeV]$	SF	uncert	SF	uncert
	$\|\eta\| < 1.2$		$1.2 < \|\eta\| < 2.5$	
20 - 25	1.023	0.206	1.340	0.450
25 - 40	0.891	0.185	0.877	0.274
40 - 60	0.935	0.182	1.200	0.275
60 - 90	0.864	0.196	0.914	0.287
90 - 140	0.866	0.140	1.024	0.257
140 - 200	0.757	0.142	0.984	0.244
200 - 300	0.917	0.126	0.686	0.114
300 - 500	0.888	0.120	1.044	0.168

Table 4.3: The light jet mistag rate scale factor (SF) and the total uncertainties including statistical and systematic contributions. The scale factors are given separately for the central region $|\eta| < 1.2$ and in the forward region $1.2 < |\eta| < 2.5$.

GeV within $\Delta R = 0.1$ from the LAr hole have been discarded and electrons that fall into the hole have been removed from the event. A systematic uncertainty has been evaluated by varying the p_{T}-threshold for the jet veto by $\pm$ 4 GeV.

4.3 Background estimates

The main background processes are W+jets, QCD, Z+jets, single top and dibosons events, as already described in Chapter 3. In the case of this analysis however it's important not only to predict their normalisation, but also the shapes of kinematic variables.

For what concerns Z+jets, single top and dibosons backgrounds that have a minor impact, both normalisations and shapes have been evaluated from Monte Carlo, while the dominant W+jets and QCD backgrounds have been estimated using data driven techniques as will be described in the following.

4.3.1 Data driven estimate of QCD background

In both electron and muon channel QCD background has been estimated using a matrix method, as already discussed in Section 3.5.1 for μ+jets events. This technique is based on selecting two categories of events, using loose and tight lepton selection requirements. QCD background is then estimated solving this system of two equations:

$$\begin{aligned} N^{\mathrm{loose}} &= N^{\mathrm{loose}}_{\mathrm{real}} + N^{\mathrm{loose}}_{\mathrm{fake}}, \\ N^{\mathrm{tight}} &= \epsilon_{\mathrm{real}} N^{\mathrm{loose}}_{\mathrm{real}} + \epsilon_{\mathrm{fake}} N^{\mathrm{loose}}_{\mathrm{fake}}, \end{aligned} \tag{4.2}$$

where N^{loose} (N^{tight}) is the number of selected events with one loose (tight) lepton, $N^{\text{loose}}_{\text{real}}$ and $N^{\text{loose}}_{\text{fake}}$ are the contributions to loose sample coming from signal and background respectively and $\epsilon_{\text{real}}(\epsilon_{\text{fake}})$ represents the probability for a real(fake) lepton that satisfies the loose criteria, to also satisfy the tight ones.

The number of selected events with a loose or a tight lepton, as well as ϵ_{real} and ϵ_{fake} have been measured in data, as explained in the following.

Muon channel:
Tight muons have been selected applying all cuts described in Section 4.2.1. The loose selection is identical to the default one, except for the fact that muon isolation requirement has been dropped.

The signal efficiency ϵ_{real} has been determined using tag and probe method in $Z \to \mu^+\mu^-$events. The fake efficiencies have been determined using a low $m_T(W)$ control region with an additional inverted triangular cut:

$$m_T(W) < 20 \text{ GeV} \quad \& \quad \not{E}_T + m_T(W) < 60 \text{ GeV} \tag{4.3}$$

The real muon contribution from W+jets and Z+jets in the control region has been obtained from Monte Carlo and subtracted to obtain a more pure QCD estimation. The efficiencies have been obtained separately for the pretag and tagged selection. They have been also parametrized in muon pseudorapidity η, to reflect the dependency on muon detector acceptance, and in the leading jet transverse momentum p_T^{j1}, since hadronic activity can have an impact on the muon isolation. The dependence of efficiencies on instantaneous luminosity and different pile-up conditions has been checked as well. No significance dependence has been found.

The shape is obtained by applying the matrix method in different bins of the kinematic distributions.

The following sources of uncertainty have been taken into account in the estimate and combined into a joint normalisation and shape uncertainty:

- the statistical uncertainty from control samples used to measure real and fake lepton efficiencies have been calculated;
- the effect of using an alternative control ragion for fake leptons efficiency evaluation asking a high impact parameter significance has been explored;
- the effect of the choice of the control region cuts has been studied by varying up and down the low transverse W mass control region cut by 5 GeV;
- the impact of the uncertainties on W/Z+jets Monte Carlo normalisation in the low $m_T(W)$ control region has been explored for the 1 jet inclusive bin, by shifting W/Z+jets contributions by their normalisation uncertainty ($\sim 25\%$).

For each of these variations, the estimate has been redone and the difference within the default one has been taken as uncertainty.

The final result obtained is 1110 ± 40 in the pretag sample and 230 ± 50 after applying the request of one b-tagged jet.

Since both shape and normalisation have been verified only to a limited extent, a more conservative uncertainty has been used for the final result: the QCD background normalisation has been shifted up and down by 50% for the pretag sample and 100% for the tagged one. Work is ongoing in order to further validate this technique and to avoid the use of overestimated uncertainties.

Electron channel:
As for muons, tight electron selection matches exactly the default electron selection, described in 4.2.1. For what concerns loose selection, some identification cuts have been removed and the isolation request has been relaxed: the electron has been required to satisfy medium selection identification cuts with the additional request of one hit in the b-layer and isolation energy has been asked to be less than 6 instead of 3.5 GeV.

The signal efficiency ϵ_{real} has been determined using tag-probe method in $Z \to e^+e^-$ events. The fake efficiency (ϵ_{fake}) is measured from data in a control region at low missing energy: 5 GeV $< \not{E}_T <$ 20 GeV. To obtain a more pure QCD sample, EW processes contributions have been subtracted using the Monte Carlo predictions. Both efficiencies have been parametrized as a function of the electron η and have been evaluated independently for the pretag and the b-tag selection.

To evaluate the systematic uncertainty of the method, different variations have been tried:

- an alternative control region for ϵ_{fake} has been used: $m_T(W) <$ 20 GeV & $\not{E}_T >$ 5 GeV;
- the upper cut on $\not{E}_T$ for control region definition has been shifted by ±5 GeV;
- the impact of real lepton contribution subtraction has been checked by scaling the Monte Carlo contribution by ±25% (equivalent to the W/Z+jets cross section uncertainty for the ≥ 1 jet selection);
- ϵ_{fake} has been parametrized as a function of different variables;
- ϵ_{real} has been taken from Monte Carlo instead of from data.

For each of these variations, the estimate has been redone, and the difference with the default estimate has been taken as uncertainty. The statistical uncertainty on the determination of both ϵ_{fake} and ϵ_{real} has been found to be negligible: smaller than 1%.

The final result obtained is 640 ± 140 in the pretag sample and 57 ± 30 after applying the request of one b-tagged jet. As for muon channel, more conservative uncertainties have been used: 50% and 100% for pretag and tagged samples respectively.

4.3.2 Data Driven estimate of W+jets background

Background normalisation estimate

The expected rate of the W+jets background has been evaluated before the request of b-tagging using the charge asymmetry technique. This result has been then multiplied by the tagging probability to obtain the final estimate.

As already mentioned in Chapter 3, W boson production at a pp collider is charge asymmetric. Positively charged W bosons can be produced from parton level processes like $u\bar{d} \rightarrow W^+$, where u is a valence quark. On the other hand, the production of W^- bosons involves valence d quarks ($d\bar{u} \rightarrow W^-$). Since Parton Density Functions (PDFs) of up and down valence quarks are different in a proton, there is a charge asymmetry. The $W^+ to W^-$ cross sections ratio $r \equiv \frac{\sigma(pp\rightarrow W^+)}{\sigma(pp\rightarrow W^-)}$ is, theoretically, relatively well understood [149]: at LHC energies it is predicted with an uncertainty of some percents. One can therefore use the theoretical prediction for r to measure the W+jets background.

The W+jets background (before the b-tagging requirement) in the signal region (≥ 4 jets) has been extracted from the following formula:

$$N_{W^+} + N_{W^-} = \left(\frac{r_{MC}+1}{r_{MC}-1}\right)(N_{W^+} - N_{W^-}) \tag{4.4}$$

where $r_{MC} \equiv \frac{\sigma(pp\rightarrow W^+)}{\sigma(pp\rightarrow W^-)}$ has been evaluated from Monte Carlo simulation applying signal selection cuts.

The difference between N_{W^+} and N_{W^-} can be substituted with the difference between the total number of events selected in data with a positively charged lepton (D^+) and the number of selected events with a negatively charged lepton (D^-). To a very good approximation, $N_{W^+} - N_{W^-} \approx D^+ - D^-$, since the other processes are charge symmetric, apart from a small bias expected from single top quark and $t\bar{t}$ productions.

As already mentioned in Chapter 1, an asymmetry occurs in single top production in s and t channels. Due to PDF effects, the number of events with t^+ (and as a consequence with a positive lepton) is higher than the one with t^- (and as a consequence with a negative lepton). These contributions have been estimated from Monte Carlo simulation and subtracted appropriately from Eq.4.4. Also $t\bar{t}$ events can have an impact on this assumption. Because of the charge asymmetry, antitop quarks will be more central than top quarks. Due to limited η coverage of the detector, the number of the selected $t\bar{t}$ events with a negative lepton will be higher than the one with a positive lepton. The impact of $t\bar{t}$ asymmetry has been studied using MC@NLO predictions and the effect has been found to be negligible. To check the effect of a possible BSM contribution, MC@NLO signal sample has been reweighted to create an artificial asymmetry compatible with the excess measured at the Tevatron (see Section 4.5 for the details about the reweighting technique). Even with this higher asymmetry, no impact has been seen on the W+jets evaluation.

Table 4.4 shows the values of r_{MC} computed from W+jets Monte Carlo simulation for different jet multiplicities. The increase of r_{MC} with the number of jets is due to the fact that higher jet multiplicities probe larger values of the parton momentum fraction x, where the difference between the up and down valence quark PDFs is larger.

Channel NJets	**Electron** pretag	**Muon** pretag
1 jet	1.482 ± 0.047	1.506 ± 0.021
2 jet	1.507 ± 0.031	1.518 ± 0.048
3 jet	1.522 ± 0.079	1.547 ± 0.066
≥ 4 jet	1.564 ± 0.079	1.655 ± 0.088

Table 4.4: Monte Carlo values for r_{MC} ratio, as a function of jet multiplicity and for the selection without b-tagging. The uncertainty shown is the sum in quadrature of the statistical and systematic contributions. The PDF systematic uncertainty is included only in the ≥ 4 jet bins.

The obtained number of W+jets events is finally 3440 ± 410(stat) ± 470 (syst) in the electron channel and 5740 ± 460 (stat) ± 790 (syst) in the muon channel.

The application of this method directly to the tagged samples is affected by a large uncertainty coming from available statistics and the present knowledge of W+jets heavy flavour (HF) content. The number of W+jets events after the request of a b-tagged jet has been therefore obtained by multiplying the pretag estimate by the tagging fraction:

$$W^{\geq 4\text{jet}}_{\text{tagged}} = W^{\geq 4\text{jet}}_{\text{pretag}} \cdot f^{\geq 4-\text{jet}}_{\text{tagged}} \tag{4.5}$$

where $W^{\geq 4\text{jet}}_{\text{pretag}}$ is the estimate in the pretag region obtained using Eq.4.4 and $f^{\geq 4-\text{jet}}_{\text{tagged}}$ is the tagging fraction determined from Monte Carlo.

In order to extract $f^{\geq 4-\text{jet}}_{\text{tagged}}$, the heavy flavour content of W+jets Monte Carlo sample has been rescaled to match the measured one in data. The heavy flavour fractions and their uncertainties have been directly measured in data in the 1-jet and 2-jet bins. The obtained fractions have been then compared to the Monte Carlo predictions and the scale factors and the respective uncertainties have been calculated: 1.63 ± 0.76 for Wcc and Wbb events, 1.11 ± 0.35 for Wc events. An additional uncertainty of 25% must be added in non-2jet bins to take into account of the propagation of the heavy flavour fractions from the 2-jet bin into another.

The number of background events has been estimated to be 310 ± 140 and 490 ± 230 in electron and muon channel respectively.

The discussion on systematics evaluation is reported in the following.

Systematics affecting the normalisation

Various systematic uncertainties on the measurement of r_{MC} have been calculated and propagated to W+jets background estimate. These include the uncertainty due to the Monte Carlo generator choice, charge misidentification, HF fraction, JES, b-tagging and light-tagging efficiencies and PDF variations.

To investigate the effects of Monte Carlo modelling on the value of r_{MC}, the predictions of two different Monte Carlo generators, Sherpa and Alpgen, have been compared for both electron and muon channel. The values of r_{MC} have been found to agree within MC statistical uncertainties in the $\geq$ 4-jet bin.

Since the detector momentum resolution is finite, and the lepton charge is identified by taking into account the bending radius of the particle track, there is a certain probability of misidentifying the lepton charge, especially for high transverse momentum leptons due to the almost straight tracks. The effect on the W+jets estimate has been investigated. This has been done by considering the number of events with two leptons passing the default object identification cuts and whose invariant mass satisfies $|m_{ll} - m_Z| < 10$ GeV. The selected sample is almost entirely composed by events in which a Z boson decays into two opposite-charge leptons. The presence of same sign pairs is therefore a consequence of charge misidentification. The charge misidentification probability has then been estimated as the fraction of events with same-sign leptons. This probability has been found to be negligible, varying from 0 to 0.003% for muons and between 0.2% and 3% for electrons depending on the lepton p_{T} and η. In addition good agreement with the Monte Carlo simulation has been observed.

Channel	**Electron**	**Muon**
PDF	6.3	6.2
MC generator	4.8	6.4
HF Fraction	42.6	44.7
Charge misID	2.1	0.0
JES	1.3	1.1
Total Systematics	46.6	47.3
Statistical	13.2	9.0

Table 4.5: Relative uncertainties (expressed as percentages) in the estimate of the W+jets background for events with at least four jets after where at least one jet is tagged as a b-jet.

The uncertainty coming from PDF has been evaluated using three different PDF sets with their respective error sets: CTEQ66 (default), MSTW2008nlo68cl [150] and NNPDF20 [151]. Instead of generating different samples for each PDF set, the effect of using different PDFs has been evaluated by reweighting events accordingly to the different predictions. Pseudosamples have been built from W+jets ALPGEN Monte

Carlo: each event passing the selection cuts has been reweighted according to its value for the partons momentum fraction x_i, the flavour of the interacting partons and the momentum scale Q^2 of the event. The analysis has been redone for each pseudosample and the ratio $r_{MC} = N(l^+)/N(l^-)$ has been recomputed.

Half of the difference between the maximum and the minimum values has been taken as the final uncertainty on r_{MC} and then propagated to the final W+jet estimate.

In addition, the HF fractions have been varied within the quoted uncertainties. Then r_{MC} and $f_{\text{tagged}}^{\geq 4-\text{jet}}$ have been computed and the estimates in the $\geq$ 4jet bin pretag and after b-tagging have been consequently redone. The largest difference between the central values of r_{MC} and $f_{\text{tagged}}^{\geq 4-\text{jet}}$ and the values computed after the HF variation have been quoted as systematics on each number. The correlation between r_{MC} and $f_{\text{tagged}}^{\geq 4-\text{jet}}$ has been taken into account to provide the final W+jets estimate.

The systematic uncertainties are shown in Table 4.5. The total uncertainty on this estimate after b-tagging request is 47% in both electron and muon channels. The HF uncertainty is by far the largest contribution.

For the analysis described in the Chapter 3 (see Section 3.4) a different approach was used since no HF measurements were available. The tag estimate was obtained from the pretag one, as:

$$W_{\text{tagged}}^{\geq 4\text{jet}} = W_{\text{pretag}}^{\geq 4\text{jet}} \cdot f_{\text{tagged}}^{2-\text{jet}} \cdot f_{2\to\geq 4}^{\text{corr}} \tag{4.6}$$

where $W_{\text{pretag}}^{\geq 4\text{jet}}$ is W+jets event count in the pretag $\geq$4-jet sample, f_{tagged}^{2-jet} is a measurement of the W+jets tag fraction in the 2-jet sample and $f_{2\to\geq 4}^{corr}$ is a correction factor that scales the fraction of tagged events in the 2-jet sample to the fraction of tagged events in the $\geq$4-jet sample, accounting for the differences in flavor composition and the corresponding event tagging probabilities. The $f_{\text{tagged}}^{2-\text{jet}}$ term was measured in data, while $f_{2\to\geq 4}^{\text{corr}}$ was estimated from Monte Carlo simulation.

In this analysis the measured HF fractions have been used. Measurements are ongoing to reduce their uncertainty and therefore the impact on W+jets estimate. Additional improvements are foreseen including more statistics. It will be possible to use data driven techniques, such as W/Z ratio and charge asymmetry, to estimate W+jets background after the b-tagging request without relying on Monte Carlo simulation

Shape determination and main systematics

W+jets background shape has been taken from Monte Carlo. In order to evaluate the systematic uncertainty Sherpa and Alpgen predictions have been compared. The effect of changing Alpgen Monte Carlo parameters have been included as well.

4.3.3 Other backgrounds

The Z+jets background normalisation and its uncertainty have been taken from Monte Carlo predictions (48% on the cross section for the 4 jets sample). The shape uncertainty has been quantified comparing ALPGEN and SHERPA MC distributions. The variation has been symmetrized.

For the small backgrounds from single top and diboson production, only overall normalisation uncertainties have been considered. A 5% has been taken for dibosons cross section, while a 10% has been used for single top.

In the calculation of the final uncertainty on background normalisation the contributions coming from object systematics, such as JES uncertainty, and luminosity have been taken into account.

4.4 Reconstruction of the event kinematics

In order to measure the top quark charge asymmetry, a precise reconstruction of top and antitop quarks rapidity is needed. A mismeasurement of their directions can cause a dilution of the asymmetry. This can be achieved using their decay products: the hadronically decaying top (antitop) can be reconstructed from three of the selected jets, while the leptonically decaying top (antitop) from one of the jets, the lepton and $\not\!\!E_T$, which provides a measurement of neutrino variables. It is necessary however to correctly assign the jets to the decay leg. The scenario is furthermore complicated by the fact that extra jets can be produced by initial and final state radiation (ISR/FSR) emissions and pile-up and so the number of possible permutations increases.

The kinematics of each event has been reconstructed using a package based on a likelihood approach, called *KLFitter*. This algorithm takes as an input a fixed value for top quark and W boson pole masses and decay widths. Event by event all possible permutations are considered including the most energetic selected jets in the event up to five, to increase the probability of identifying the proper combination in the presence of additional jets. In addition, the resolution of reconstructed objects with respect to the *true* ones is taken into account through the use of object specific transfer functions. The final likelihood is reported below:

$$\begin{aligned} \mathrm{L} \;=\; & \mathcal{B}(\widetilde{E}_{\mathrm{p,1}}, \widetilde{E}_{\mathrm{p,2}} | m_W, \Gamma_W) \cdot \mathcal{B}(\widetilde{E}_{\mathrm{l}}, \widetilde{E}_{\nu} | m_W, \Gamma_W) \cdot \\ & \mathcal{B}(\widetilde{E}_{\mathrm{p,1}}, \widetilde{E}_{\mathrm{p,2}}, \widetilde{E}_{\mathrm{p,3}} | m_t, \Gamma_t) \cdot \mathcal{B}(\widetilde{E}_{\mathrm{l}}, \widetilde{E}_{\nu}, \widetilde{E}_{\mathrm{p,4}} | m_t, \Gamma_t) \cdot \\ & \mathcal{W}(\widetilde{E}_x^{miss} | \hat{p}_{x,\nu}) \cdot \mathcal{W}(\widetilde{E}_y^{miss} | \hat{p}_{y,\nu}) \cdot \mathcal{W}(\widetilde{E}_{\mathrm{lep}} | \hat{E}_{\mathrm{lep}}) \cdot \\ & \prod_{\mathrm{i}=1}^{4} \mathcal{W}(\widetilde{E}_{\mathrm{p,i}} | \hat{E}_{\mathrm{jet,i}}) \cdot \prod_{\mathrm{i}=1}^{4} \mathcal{W}(\widetilde{\eta}_{\mathrm{p,i}} | \hat{\eta}_{\mathrm{jet,i}}) \cdot \prod_{\mathrm{i}=1}^{4} \mathcal{W}(\widetilde{\phi}_{\mathrm{p,i}} | \hat{\phi}_{\mathrm{jet,i}}) \cdot \\ & P(b\text{-tag} \mid \text{quark}), \end{aligned} \tag{4.7}$$

where:

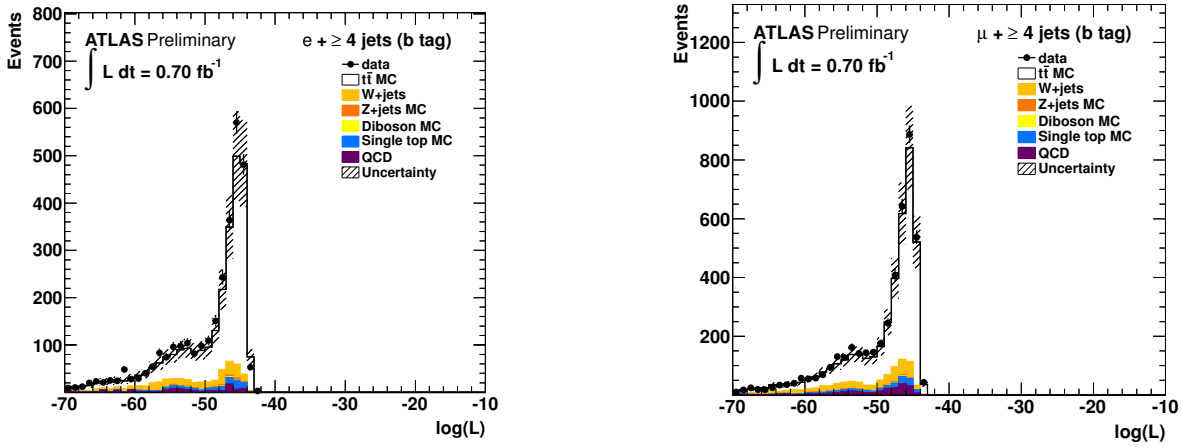

(a) (b)

Figure 4.1: *Expected and observed distributions for the likelihood used to reconstruct the $t\bar{t}$ final state for the electron (a) and the muon (b) channel. The data is compared to the sum of the $t\bar{t}$ signal contribution and backgrounds. The background contributions from W+jets and QCD multijet production have been estimated from data, while the other backgrounds are estimated from simulation. Uncertainties include statistical contributions, systematic uncertainties on W+jets and QCD normalisation and also the uncertainties on luminosity, JES, b-tag scale factors and $t\bar{t}$ cross section.*

- The m_t and Γ_t are the top quark mass and its decay width, respectively.
- The m_W and Γ_W are the W boson mass and its decay width, respectively.
- The $\widetilde{X}$ are the partonic object quantities and $\hat{X}$ their corresponding reconstructed values.
- The $\mathcal{B}$ represent the Breit-Wigner parametrization of the parton (from which the associated jets originated) energies $\widetilde{E}_{\mathrm{p,i}}$ and lepton energies $\widetilde{E}_{\mathrm{lep}}$ with respect to the fitted ones, respectively.
- The $\mathcal{W}$ are the transfer functions associating the reconstructed quantities to the partonic object properties.
- $P(b\text{-tag} \mid \text{quark})$ is a b-tag probability or rejection efficiency, depending on the quark flavour. It has been used to take into account the tagging efficiency and rejection rate of the used b-tagging algorithm.

The most likely event topology is chosen by minimising the $ln(\mathrm{L})$. For each event, the permutation with the highest probability is used for all further studies.

The reconstruction performance has been evaluated using MC@NLO signal sample and comparing top (antitop) *true* direction at production level with the reconstructed one. For this purpose, we have considered only events where the four reconstructed jets and the lepton have been successfully matched to corresponding truth level objects. In order to perform this association, a simple ΔR matching has been applied using cone sizes of 0.3 for jets and 0.1 for leptons. An event is considered matched if all truth partons originating from the hard scattering process can successfully be identified with reconstructed jets and the truth lepton is matched to the reconstructed one.

The overall efficiencies for the reconstruction of the correct event topology ("All Correct") has been found to be 74% for both electron and muon channel.

The expected likelihood distributions and the observed ones in data are shown in Figure 4.1. The agreement between the data and the predictions is very good.

In Figure 4.2 top and antitop rapidities distributions are shown for both electron and muon channel, while in Figure 4.3 the difference between top and antitop rapidities are represented for both channels. Very good agreement between data and signal+background expectation has been observed for all distributions in both electron and muon channel.

4.5 Unfolding

4.5.1 Motivation

Detector resolution and the applied event selection can alter the distribution of any observable.

The impact on charge asymmetry has been studied on Monte Carlo using MC@NLO signal sample (*SM scenario* in the following). In order to check the effect on a non-zero asymmetry, $t\bar{t}$ events have been reweighted in order to simulate an asymmetry compatible with the excess seen by CDF experiment at high $t\bar{t}$ invariant mass (*BSM scenario* in the following). For this scope, a parametrization proposed by B. Webber [152] has been considered, which consists in assigning a weight to each event coming from $q\bar{q}$ initial state depending on top quark pair invariant mass ($m_{t\bar{t}}$) and the difference between top and antitop rapidities (Δy):

$$1 + f(m_{t\bar{t}}) \tanh(\Delta y/2), \tag{4.8}$$

where

$$f(m_{t\bar{t}}) = m_{t\bar{t}}/(200\,\mathrm{GeV}) - 2 \tag{4.9}$$

It is important to remark that this is not a model, but only an empirical parametrization introduced to reproduce the asymmetry measured in the CDF data simulating a fictitious asymmetry contribution instead of a specific BSM model.

In order to quantify acceptance and detector resolution effects, the asymmetry at partonic level, before any selection cuts, has been compared to the one measured

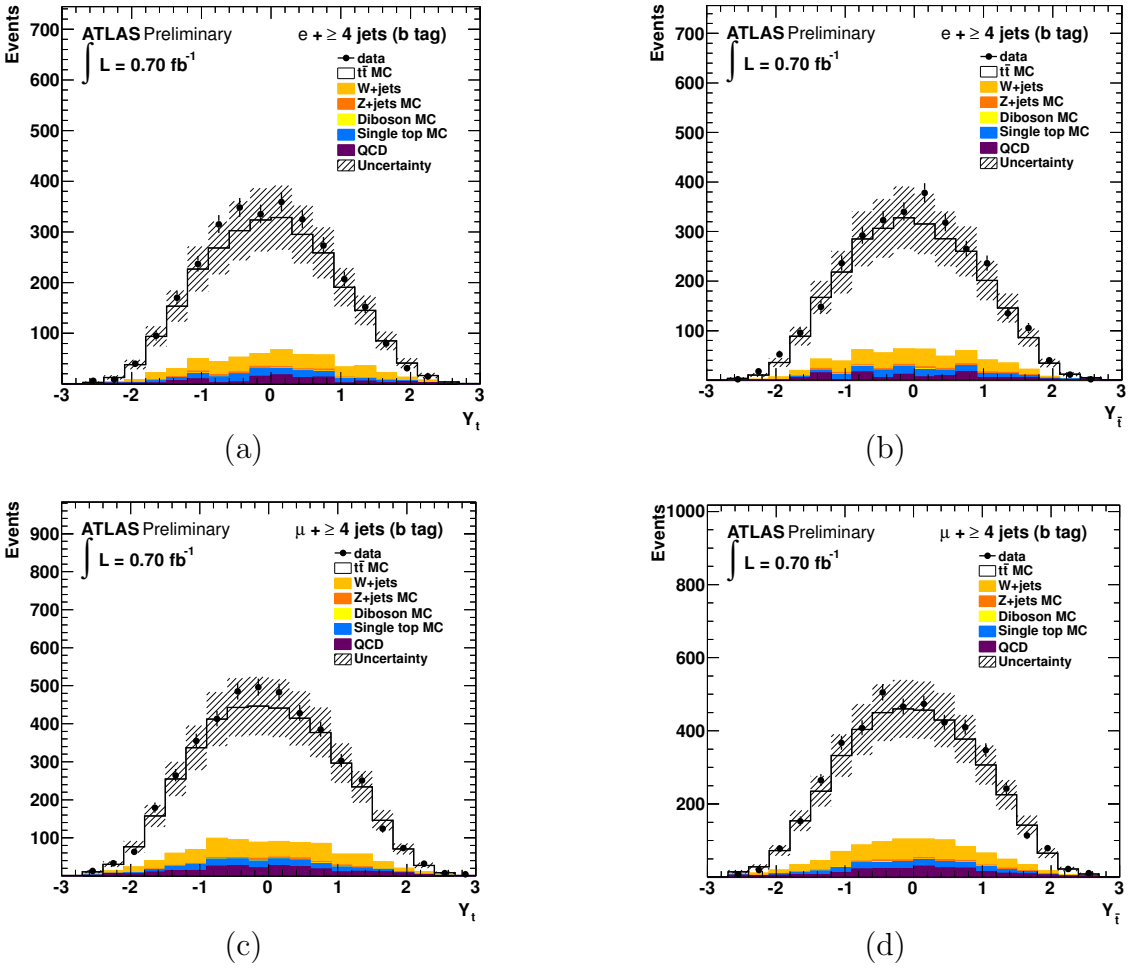

Figure 4.2: *Top and antitop rapidities in the electron (upper row) and muon (lower row) channel after b-tagging. Left plots show the top rapidity, right plots the antitop rapidity. Data (points) and Monte Carlo estimates (solid lines) are represented. QCD and W+jets backgrounds have been obtained from data with the methods explained in Section 4.3. Uncertainties include statistical contributions, systematic uncertainties on W+jets and QCD normalisation and also the uncertainties on luminosity, JES, b-tag scale factors and $t\bar{t}$ cross section.*

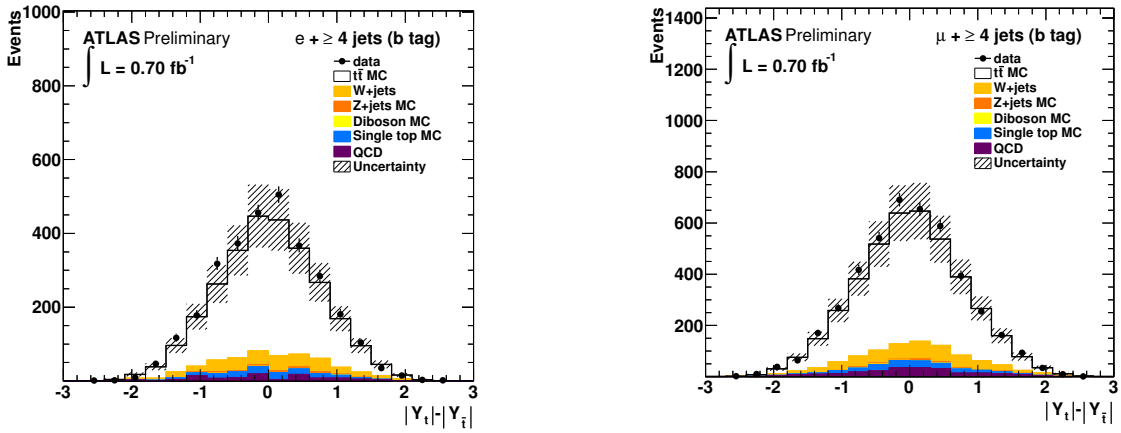

Figure 4.3: $\Delta|y|$ *distribution for electron (a) and muon (b) channel after b-tagging. Data (points) and Monte Carlo estimates (solid lines) are represented. QCD and W+jets backgrounds have been obtained from data with the methods explained in Section 4.3. Uncertainties include statistical contributions, systematic uncertainties on W+jets and QCD normalisation and also the uncertainties on luminosity, JES, b-tag scale factors and* $t\bar{t}$ *cross section.*

after selection cuts on Monte Carlo truth decay products and the one after selection cuts on reconstructed decay products.

Figure 4.4 shows the charge asymmetry, defined in Equation 4.1, as a function of $m_{t\bar{t}}$ for both the SM (left) and BSM (right) scenario. The three rows represent the set of cuts described above: no selection, selection on Monte Carlo objects and selection on reconstructed objects. The top and antitop variables used are taken from Monte Carlo truth information: no kinematic reconstruction has been performed at this level. The asymmetry is computed for all the events (black box) and only for on $q\bar{q}$ events (red dots). The uncertainties quoted in the plots are both MC@NLO statistical uncertainty and systematics added in quadrature. Systematic uncertainty has been obtained as the sum in quadrature of different contributions:

- the effect of using different Monte Carlo generators, which has been studied comparing the predictions of MC@NLO and POWHEG samples;
- the effect of using different parton showers: POWHEG +HERWIG prediction has been compared with the one of POWHEG +PYTHIA ;
- the impact of changing the tune of ISR and FSR, which has been estimated using ACERMC samples.

The asymmetry is diluted in SM and BSM cases by the application of the selection cuts both on the parton and on the reconstructed objects. In order to be able

to compare the measured asymmetry with theoretical predictions, it is therefore important to correct the $\Delta|y|$ distribution for acceptance and detector resolution effects. This is obtained using unfolding techniques as described in the following.

4.5.2 Unfolding technique

The truth $\Delta|y|$ distribution, represented by a histogram T_j, is distorted into the reconstructed distribution S_i after detector acceptance, resolution effects and event selection via the response matrix R_{ij}:

$$S_i = \sum_j R_{ij} T_j, \tag{4.10}$$

$$R_{ij} = P(\text{ observed in bin } i \mid \text{expected in bin } j\ ). \tag{4.11}$$

where the response matrix has been derived from MC@NLO signal sample.

An additional acceptance correction has been performed in order to take into account events which did not pass the object and event selection. This effect has been quantified by a correction at the truth level for selected events to the truth level before selection.

In order to recover the distribution of $\Delta|y|$ observable at parton level from the one obtained after reconstruction, the response matrix has to be inverted. However, as in most situations where unfolding is applied, there is no exact inverse response matrix R_{ij}^{-1}, such that

$$R_{ij} \cdot R_{ij}^{-1} = I, \tag{4.12}$$

where I is the unity matrix. Hence, approximations are needed to perform the matrix inversion to acceptable accuracy.

As part of the inversion process, a regularisation has to be applied in order to avoid statistical fluctuations in the used distributions being identified as actual shape of the "true" distribution.

Several procedures have been developed to perform the inversion and the necessary regularisation. For this analysis, a Bayesian iterative unfolding [153] implemented in the RooUnfold package [154] has been applied.

Bayes' theorem is applied iteratively in order to invert the response matrix. The first step is defining the posterior probability of having the true distribution T_j given the measured distribution S_i according to Bayes' theorem:

$$P(T_j|S_i) = \frac{P(S_i|T_j)P_0(T_j)}{\sum_j P(S_i|T_j)P_0(T_j)}, \tag{4.13}$$

where $P(S_i|T_j)$ carries the same information of R_{ij} and $P_0(T_j)$ represents our prior assumption about T_j, taken from the MC@NLO Monte Carlo prediction. The posterior probability density function is then used as the prior for the next step of iteration:

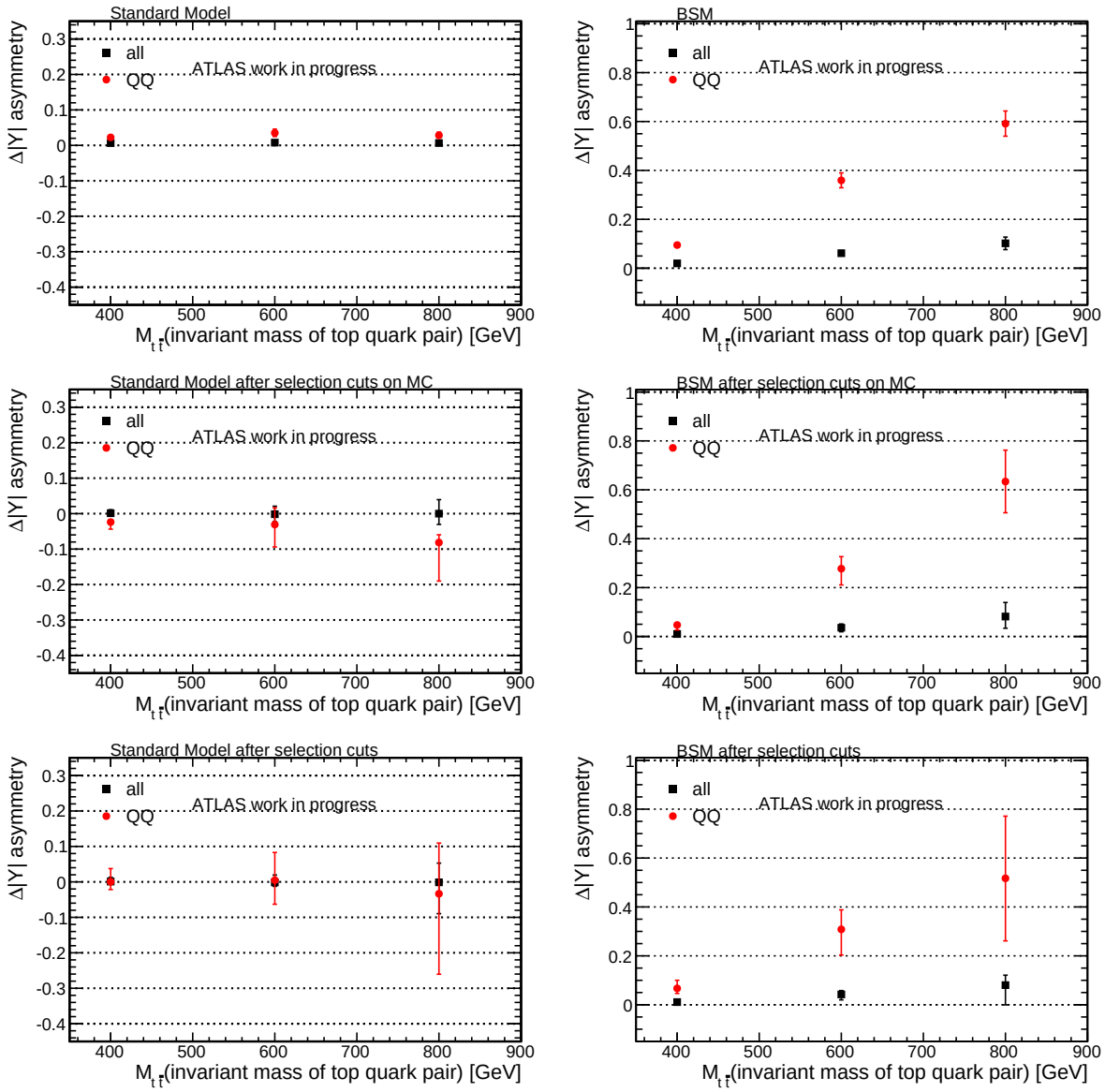

Figure 4.4: $\Delta|y|$ *asymmetry as a function of* $m_{t\bar{t}}$*. The three rows correspond respectively to: no selection cuts applied; selection cuts applied on Monte Carlo objects; selection cuts applied on reconstructed objects. The left plots correspond to the SM scenario, while the right plots correspond to the BSM scenario with the parametrization in Equation 4.8. The black boxes represent the value of the asymmetry for all the events passing the various cuts, while the red dots the asymmetry computed only for* $q\bar{q}$ *events. Statistical and systematics uncertainties as explained in the text are both included and summed up in quadrature.*

$$
\begin{aligned}
P_1(T_j) &\propto \sum_i P(T_j|S_i)\cdot S_i \propto \sum_i P(S_i|T_j)\cdot P_0(T_j)\cdot S_i \\
P_2(T_j) &\propto \sum_i P(T_j|S_i)\cdot S_i \propto \sum_i P(S_i|T_j)\cdot P_1(T_j)\cdot S_i \\
&\vdots
\end{aligned}
$$

The regularisation of the resulting distribution is obtained automatically using a small number of iterations: four in the analysis presented in this thesis. The main systematic uncertainties are due to the chosen Monte Carlo generator and the prior distribution.

This procedure has been validated with a closure test performed on Monte Carlo. To check if the tool was able to actually reproduce an arbitrary asymmetry in the distribution at truth level, the MC@NLO signal Monte Carlo has been split in two statistically independent samples. The first one has been used for the creation of the response matrix, while the second as pseudo data for the unfolding process by creating ensembles of subset of the sample. The respective sample fraction has been then reweighted to different asymmetry values. The unfolded asymmetry value has been finally compared to the truth input one: good performance has been observed.

4.6 Systematic uncertainty

There is a multitude of systematic effects that can have an impact on the charge asymmetry measurement. These need to be understood and modelled to assign a systematic uncertainty on the final result. The systematics that have been considered and evaluated for this analysis are discussed in the following.

- $t\bar{t}$ **modelling** - The effect of using different Monte Carlo generators has been analysed: the POWHEG generator has been used in addition to the MC@NLO sample for comparison.

- **Parton shower and fragmentation** - In addition to the matrix element level Monte Carlo generator, the effect of different showering models has been taken into account by comparing the results for the POWHEG generator with showering performed by PYTHIA and by HERWIG .

- **ISR and FSR** - In order to take into account initial and final state radiation, which can introduce additional jets in the observed events, different Monte Carlo samples with varying ISR and FSR contributions have been used. The systematic uncertainty has been quoted as the maximum discrepancy observed from these variations.

- **PDF Uncertainty** - The signal Monte Carlo uses CTEQ66 PDFs to model the incoming partons. These PDFs have been measured from data (e.g. in deep inelastic scattering experiments) and have been assigned an uncertainty, which can be calculated using a tool called LHPDF. Pseudosamples have been built by reweighting the events according to the tool output. For each pseudo sample a different response matrix has been built and the unfolded asymmetry has been calculated. The systematic uncertainty has been evaluated comparing these different values.

- **Top mass** - Since the top mass parameter has been considered as fixed, the uncertainty on the measurement of the mass has been taken into account. Different Monte Carlo samples generated with different mass parameters (scaled up and down to 175 GeV and 170 GeV, respectively) have been used and the observed deviations have been linearly interpolated according to the actual uncertainty of the top mass parameter.

- **Backgrounds** - The uncertainties on the background normalisations and shapes have been already discussed in Section 4.3. Each background has been varied within the uncertainty and the full analysis chain has been redone. The difference with respect to the default asymmetry values has been taken as systematic. As already mentioned, a conservative uncertainty of 100% has been used for the QCD background.

- **Monte Carlo generator statistics** - Since the signal Monte Carlo sample enters directly into the response matrix and statistical fluctuations in the bins of this matrix can have an impact on the unfolding process, an ensemble test has been performed by fluctuating the obtained nominal response matrix on a bin to bin basis following a Poissonian model (taking into account weighted events).

- **Lepton efficiencies** - In order to account for leptons trigger, reconstruction and identification efficiencies, global and object based scale factors have been assigned to each event, as discussed in Section 4.2.3. These scale factors have been varied within their uncertainty and the asymmetry values have been recalculated. The final systematics has been obtained as the difference with the default asymmetry values.

- **Lepton scales and resolution** - The lepton momentum has been scaled up and down and smeared within $1\,\sigma$ uncertainty. In addition, the missing energy has been re-calculated with the modified four-vectors. The event selection and reconstruction has been then re-run for the different scales and smearings. The systematic uncertainty has been assessed by comparing the result of each run and the default one.

- **Charge misidentification** - Lepton charge misidentification affects both background evaluation and response matrix. The impact on the analysis has

been evaluated by randomly flipping the sign of lepton charge (and so the sign of $\Delta|y|$) according to its charge misidentification probability.

- **JES** - The JES uncertainty effect has been estimated by scaling up and down the energy of all selected jets by one standard deviation, calculated as reported in Section 4.2.3. In addition the missing energy had to be re-evaluated, taking into account the scaled contributions of the jets in both p_x and p_y components. The complete event selection and KLFitter reconstruction has been then re-run with the scaled jets. The deviation with respect to the nominal value has been symmetrized and taken as systematic uncertainty. This has been done separately for the three contributions to the JES: jet energy calibration, pile-up impact and the JES uncertainty associated to b-jets. The total uncertainty is reported in the Table 4.6.

- **Jet energy resolution** - A smearing of the jet transverse momentum has been applied as systematic to reflect the resolution for the jet energy observed in the data. The effect has then been propagated to $\not{E}_T$. The full analysis chain has been redone and the output has been compared with the default value. The resulting discrepancies have been symmetrised and quoted as systematic uncertainty.

- **Jet reconstruction efficiency** - The jet reconstruction efficiency (JRE) impact has been evaluated by randomly dropping jets from events with a probability of about 2%. The resulting difference with respect to the nominal case has been symmetrised and quoted as systematic uncertainty from the JRE.

- **b-tag scale factors** -The b-tagging scale factors contain uncertainties which result in small shape variations. In order to determine the deviation from the nominal case, the resulting samples have been shifted up and down by their respective provided uncertainties. The full analysis has been then re-run. The systematic uncertainty has been assigned from the comparison with the nominal asymmetry values.

- **b-tag charge** - The final result has been obtained assuming identical b-tagging efficiencies for b and $\bar{b}$. A dependency of the b-tagging efficiencies on the b-quark charge could lead however to a bias in the measured and unfolded asymmetries in the b-tagged sample. Hence, a simple study on truth level has been performed by simulating a difference in b-tagging efficiency of 5% between b- and $\bar{b}$-quarks. The resulting impact on the charge asymmetry on truth level has been studied and the difference to the nominal case has been quoted as systematic uncertainty.

- **LAr hole uncertainty** - The jet p_{T} threshold to reject jets falling into the LAr hole has been varied of $\pm$ 4 GeV. The asymmetry values have been re-calculated. The final systematics has been obtained as the difference with the default asymmetry values.

A summarized list of all systematics and their contribution to the overall uncertainties can be found in Table 4.6.

The most important contribution to the total uncertainty comes from signal modelling: the choice of signal Monte Carlo generator, parton shower modelling and finally the impact of ISR/FSR uncertainty. The first two contributions, in particular, are different between electron and muon channel. Both of them are however consistent with the uncertainty due to the available Monte Carlo statistics of POWHEG samples. The observed effect can be therefore only due to a statistical fluctuation.

Another large effect is due to jet energy scale resolution. Also in this case the uncertainty in electron channel is higher than the one in muon channel. This discrepancy is not however statistically significant.

Important contributions come finally from W+jets and QCD background uncertainties. Possible improvements on these estimates have been already discussed in Section 4.3.

4.7 Conclusions and outlooks

The obtained distributions after unfolding can be found in Figure 4.5, while the measured values of the asymmetry, after applying the unfolding, are reported in Table 4.7 for both electron and muon channels.

Using the analytic best linear unbiased estimator (BLUE) method [155] [156] to combine these two measurements taking the relevant systematic correlations into account, a combined value of:

$$A_C = -0.024 \pm 0.016\,(\text{stat.}) \pm 0.023\,(\text{syst.})$$

has been obtained.

This result is compatible with the SM prediction (from the MC@NLO Monte Carlo generator) of $A_C = 0.006$, showing no evidence for an enhancement from BSM physics.

Even if this is the first measurement performed by the ATLAS collaboration, it gives already the possibility to discriminate between new physics models. As can be seen from Figure 4.6, the measured value disfavours Z' and W' models. The other two models are still compatible with both the ATLAS and the CDF measurement at high invariant mass, which implies $0.17 < A_{FB}^{new}$ at 95% confidence level.

Outlooks

In the future some work will be done in order to lower systematics as much as possible. Detector commissioning ongoing will enable to reduce the contributions coming from object reconstruction. Comparison between data and Monte Carlo predictions will also give the possibility to tune different generators and therefore to reduce the uncertainty coming from signal modelling.

	Electron channel	Muon channel
Source of systematic uncertainty	ΔA_C	
Signal and background modelling		
$t\bar{t}$ generator	0.0243	0.0100
Parton shower/fragmentation	0.0108	0.0079
ISR/FSR	0.0074	0.0074
PDF uncertainty	0.0008	0.0008
Top mass	0.0059	0.0059
QCD normalisation	0.0062	0.0059
W+jets normalisation	0.0054	0.0097
W+jets shape	0.0043	0.0043
Z+jets normalisation	0.0002	0.0002
Z+jets shape	0.0010	0.0010
Single Top normalisation	0.0002	0.0002
Diboson normalisation	0.00001	0.00001
MC sample sizes	0.0043	0.0029
Detector modelling		
Muon efficiencies	(n.a.)	0.0002
Muon momentum scale and resolution	0.0004	0.0004
Electron efficiencies	0.0004	(n.a.)
Electron energy scale and resolution	0.0004	0.0004
Lepton charge misidentification	0.0002	0.0002
JES	0.0041	0.0046
Jet energy resolution	0.0105	0.0040
Jet reconstruction efficiency	0.0003	0.0003
b-tagging scale factors	0.0038	0.0038
Charge asymmetry in b-tagging efficiency	0.0007	0.0007
Calorimeter readout	0.0015	0.0029
Combined uncertainty	0.032	0.022

Table 4.6: List of sources of systematic uncertainty and their impact on the measured asymmetry in the electron and muon channel. In cases where asymmetric uncertainties were obtained, a symmetrisation of the uncertainties was performed.

Asymmetry	detector unfolded	detector and acceptance unfolded
A_C (electron)	-0.012 ± 0.026 (stat.) ± 0.030 (syst.)	-0.009 ± 0.023 (stat.) ± 0.032 (syst.)
A_C (muon)	-0.030 ± 0.021 (stat.) ± 0.020 (syst.)	-0.028 ± 0.019 (stat.) ± 0.022 (syst.)

Table 4.7: The measured charge asymmetry values for the electron and muon channels for different levels of unfolding. The quoted uncertainties are statistical and systematic, respectively.

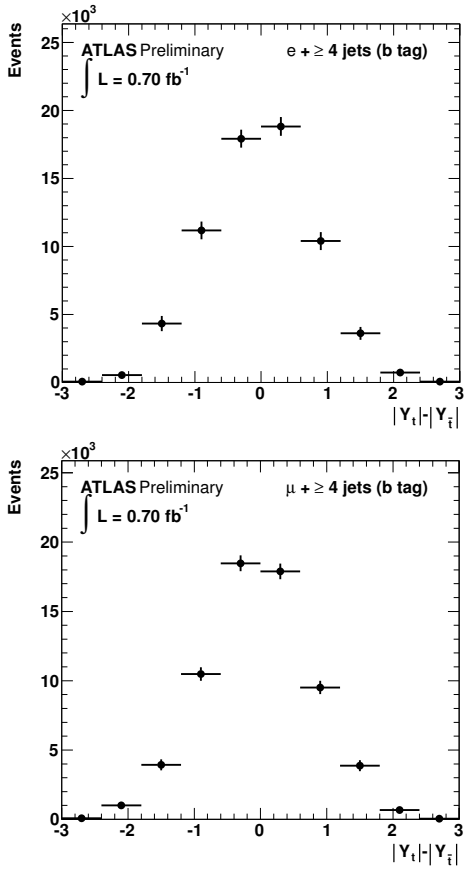

Figure 4.5: *Inclusive unfolded charge asymmetry distribution, for electron (up) and muon channel (down). The uncertainties are statistical only.*

Furthermore, with more integrated luminosity, measurements of differential asymmetries will be done. As already mentioned in Section 1.4.2, the sensitivity to new physics increases looking at differential distributions. The most promising variable to look at is the asymmetry as a function of top quark pair invariant mass ($m_{t\bar{t}}$). Apart from this, other kinematic variables will be considered, as for example the longitudinal momentum of the top quark pair system.

Furthermore the study of different observables, also using directly leptons variables, will be performed.

A limitation to this analysis is the fact that the asymmetry is diluted by the contribution of the symmetric gg fusion precess. The present selection is even reducing the $q\bar{q}$ contribution with respect to the total, as can be seen from Table 4.8. This table shows gg fusion and $q\bar{q}$ annihilation contribution to the number of $t\bar{t}$ selected events after each individual selection cut for muon channel. The selection cuts seem to slightly enhance the gg fraction with respect to the $q\bar{q}$ fraction. In fact, the $q\bar{q}/gg$ ratio lowers form 0.24 to 0.18 at the end of the cut-flow.

The dependence of the $q\bar{q}$ fraction on the invariant mass of the top-antitop pair

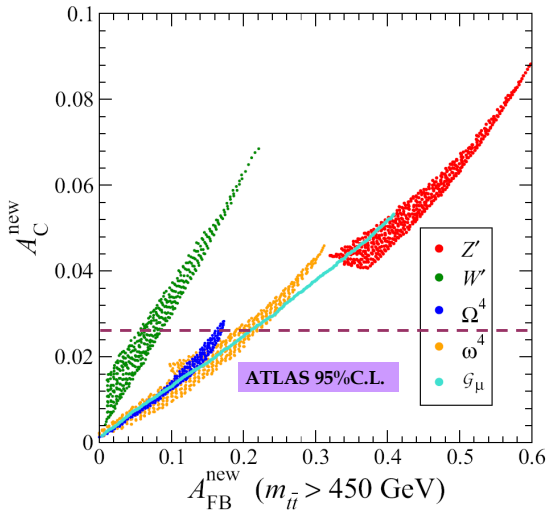

Figure 4.6: *Allowed regions for the new physics contributions to the FB asymmetry at the Tevatron and the inclusive charge asymmetry at the LHC [27]. BSM predictions are compared with the ATLAS measured asymmetry.*

Cut-flow efficiency, muon channel				
cut	ε_{tot}	$\varepsilon_{q\bar{q}}$	ε_{gg}	$q\bar{q}/gg$
All events	1.00	0.19	0.79	0.24
Trigger	1.00	0.19	0.79	0.24
Good Vertex	1.00	0.19	0.79	0.24
$\#\mu > 0$	0.23	0.04	0.18	0.24
$\#\mu = 1$	0.22	0.04	0.17	0.24
$\#e = 0$	0.20	0.04	0.16	0.24
Trigger match	0.20	0.04	0.16	0.24
e/μ overlap removal	0.20	0.04	0.16	0.24
Jet cleaning	0.20	0.04	0.16	0.24
$\not{E}_T > 20$ GeV	0.18	0.04	0.15	0.24
$\not{E}_T + M_{T_W} > 65$ GeV	0.17	0.03	0.14	0.24
at least 2 jets $p_T > 25$ GeV, $\|\eta\| < 2.5$	0.17	0.03	0.13	0.24
at least 3 jets $p_T > 25$ GeV, $\|\eta\| < 2.5$	0.14	0.03	0.11	0.22
at least 4 jets $p_T > 25$ GeV, $\|\eta\| < 2.5$	0.09	0.01	0.08	0.18
1 b-tag	0.06	0.01	0.05	0.18

Table 4.8: Muon selection cutflow. The efficiencies ε are calculated as the ratio between the number of events passing a specific cut over the total number of events before any cut (the second row). The first column describes efficiency of the various cuts, the second and the third one respectively the $q\bar{q}$ and the gg fraction in the events passing a specific cut while the fourth column shows the relative ratio between $q\bar{q}$ and gg events.

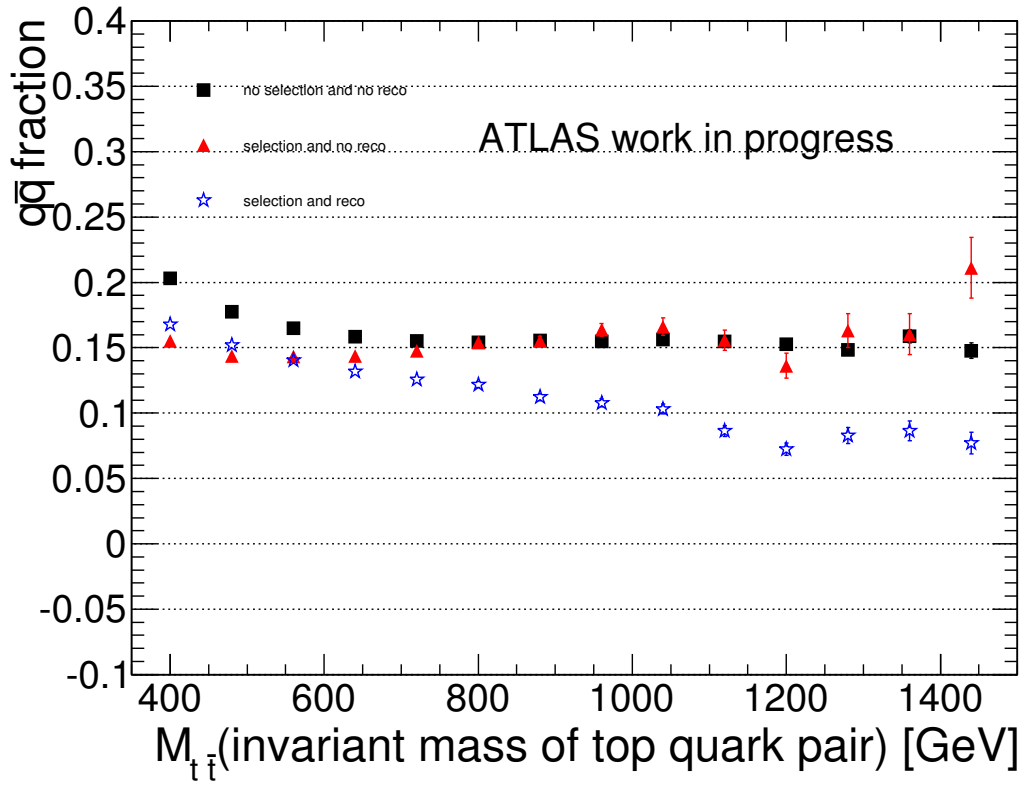

Figure 4.7: *$q\bar{q}$ fraction as a function of true $m_{t\bar{t}}$ for all the events (black dots),$q\bar{q}$ fraction as a function of true $m_{t\bar{t}}$ only for the events passing all the selection cuts applied to reconstructed objects (red triangles) and $q\bar{q}$ fraction as a function of reconstructed $m_{t\bar{t}}$ for events passing the same cuts on reconstructed objects (blue stars).*

$m_{t\bar{t}}$ has been also studied, as shown in Figure 4.7. In order to quantify the effects of the reconstruction algorithms and of detector acceptance, $q\bar{q}$ fraction has been studied at three levels separately: all the events have been considered without applying any selection cuts and calculating $m_{t\bar{t}}$ from true t and $\bar{t}$ kinematic variables (black dots); the events passing all the selection cuts applied at top decay products after reconstruction, but still calculating $m_{t\bar{t}}$ from true t and $\bar{t}$ (red triangles) and the events passing selection cuts as a function of $m_{t\bar{t}}$ calculated from t and $\bar{t}$ kinematic variables, obtained with the KL fitter algorithm (blue stars). The $q\bar{q}$ fraction is lower in the high mass region, independently on the selection cuts, suggesting a physical effect related to the PDF contributions. Furthermore, in the low $m_{t\bar{t}}$ region, the $q\bar{q}$ fraction lowers after the selection cuts, suggesting an acceptance effect.

Some studies are already ongoing in order to enhance $q\bar{q}$ contribution. A recent proposal [157] consists in putting a cut on $t\bar{t}$ boost along z-axis. Since in $q\bar{q}$ events one of the incoming partons comes from the sea, while other one is a valence quark, the boost along the z-axis will be higher than in events generated by gg fusions, where both partons come from the sea.

Acknowledgements

The work described in this thesis would not have been possible without the help and support of many people.

First of all, I want to thank my supervisor Prof. Francesco Ragusa for the passion and the accuracy that he put in his job. Despite all his duties, he has always found some time to discuss with me. Thanks a lot for all the precious suggestions!

A huge thanks to Dott. Tommaso Lari for his immense and contagious passion for physics and for all the time he has dedicated to me. You have taught me to be curious and to look deeply into things, you have answered all my questions, taken into account all my proposals and corrected all my mistakes.

I want to thank also Prof. Marina Cobal for accepting to review my thesis and for the very useful discussions about my work.

I am very grateful also to Dott. Clara Troncon for the attention she has always paid to me and to my work, for all the reviews to my slides, proceedings, CVs, etc. and for all her suggestions.

I want to thank also Prof. Attilio Andreazza for the very instructive discussions about Pixel Detector and top quark physics.

I want also to thank the ATLAS colleagues that have contributed to the top cross section and charge asymmetry measurements. In particular I want to thank Michele and Kerim for the time spent working together, discussing and helping each other. Your support and your passion for physics have been very important for me!

Thanks a lot to the whole Milano ATLAS group, in particular to Dott. Chiara Meroni, Dott. Donatella Cavalli and Dott. Silvia Resconi, for the attention to me and to my work.

Thanks to Lidia, Sofia and Caterina for their friendship and support, to Iro, Rosa, Federico and Ruggero. Finally I want to thank Andrea, my top quark companion. Thanks for all the time spent working together, for all your help with the code and for the support that you gave me when I was in Protvino without my bag.

I want now to thank my parents, my sister and all the friends that have come along with me in these years: your love and your esteem have always accompanied me and helped to look at the reality in front of me without be afraid.

Finally I want to thank my husband Martino, who has always supported and encouraged me to follow my desires and aspirations. Your immense attention to me, your patience and your tenderness fill me with wonder and gratitude.

Bibliography

[1] S. W. Herb et al., *Observation of a Dimuon Resonance at 9.5 GeV in 400 GeV Proton-Nucleus Collisions*, Phys. Rev. Lett. **39**, 252 (1977).

[2] G. 't Hooft and M. Veltman, *Regularization and Renormalization of Gauge Fields*, Nucl. Phys. B **44**, 189 (1972).

[3] ALEPH Collaboration, DELPHI Collaboration, L3 Collaboration, OPAL Collaboration, and SLD Collaboration, LEP Electroweak Working Group and SLD electroweak and Heavy Flavour Group, *Precision Electroweak Measurements on the Z Resonance*, Phys. Rep. **427**, 257 (2006).

[4] CDF Collaboration, *Observation of Top Quark Production in $\bar{P}$-P Collisions*, Phys. Rev. Lett. **74**, 2626 (1995).

[5] D0 collaboration, *Observation of the Top Quark*, Phys. Rev. Lett. **74**, 2632 (1995).

[6] N. Kidonakis, *NNLL resummation for s-channel single top quark production*, Phys. Rev. D **81**, 054028 (2010).

[7] N. Kidonakis, *Single top quark production at the Fermilab Tevatron: Threshold resummation and finite-order soft gluon corrections*, Phys. Rev. D **74**, 114012 (2006). The cross sections for the single top quark processes ($m_t = 172.5$ GeV) are 1.04 ± 0.04 pb (s-channel) and 2.26 ± 0.12 pb (t-channel).

[8] N. Kidonakis, *Next-to-next-to-leading-order collinear and soft gluon corrections for t-channel single top quark production*, Phys. Rev. D **83**, 091503 (2011).

[9] N. Kidonakis, *Two-loop soft anomalous dimensions for single top quark associated production with a W- or H-*, Phys. Rev. D **82**, 054018 (2010).

[10] N. Kidonakis, *Next-to-next-to-leading soft-gluon corrections for the top quark cross section and transverse momentum distribution*, Phys. Rev. D **82**, 114030 (2010).

[11] K. Nakamura (Particle Data Group), *Review of Particle Physics*, J. Phys. G: Nucl. Part. Phys. **37**, 075021 (2010).

[12] S. Moch and P. Uwer, *Theoretical status and prospects for top-quark pair production at hadron colliders*, Phys. Rev. D **78**, 034003 (2008);
U. Langenfeld, S. Moch, and P. Uwer, *New results for ttbar production at hadron colliders*, arXiv:0907.2527;
M. Aliev, H. Lacker, U. Langenfeld, S. Moch, P. Uwer, and M. Wiedermann, – *HATHOR – HAdronic Top and Heavy quarks crOss section calculatoR*, arXiv:1007.1327.

[13] S. Moch and P. Uwer, Nucl. Phys. B, Proc. Suppl. **183**, 75 (2008).

[14] CDF Collaboration, *Measurement of the Ratio $\sigma_{t\bar{t}}/\sigma_{Z/\gamma^* \to ll}$ and Precise Extraction of the $t\bar{t}$ Cross Section*, PRL **105**, 012001 (2010).

[15] CDF Collaboration, *Combination of CDF top quark pair production cross section measurements with up to 4.6 fb^{-1}*, Conf. Note 9913.

[16] D0 collaboration, *Measurement of the top quark pair production cross section in the lepton+jets channel in proton-antiproton collisions at $\sqrt{s}$=1.96 TeV*, Phys. Rev. D **84**, 012008 (2011).

[17] D0 collaboration, *Measurement of the $t\bar{t}$ production cross section using dilepton events in $p\bar{p}$ collisions*, Phys. Lett. B **704**, 403-410 (2011).

[18] ATLAS Collaboration, *Measurement of the $t\bar{t}$ production cross-section in pp collisions at $\sqrt{s}$ = 7 TeV using kinematic information of lepton+jets events*, ATLAS-CONF-2011-121.

[19] CMS Collaboration, *Measurement of ttbar Pair Production Cross Section at $\sqrt{s}$=7 TeV using b-quark Jet Identification Techniques in Lepton + Jet Events*, CMS-PAS-TOP-11-003.

[20] Paola Ferrario and German Rodrigo, *Charge asymmetry of top quarks.*, PoS DIS2010:191 (2010).

[21] Biplob Bhattacherjee and Sudhansu S. Biswal and Diptimoy Ghosh, *Top quark forward-backward asymmetry at Tevatron and its implications at the LHC*, Phys. Rev. D **83**, 091501(R) (2011).

[22] L. G. Almeida, G. F. Sterman and W. Vogelsang, *Threshold Resummation for the Top Quark Charge Asymmetry*, Phys. Rev. D **78**, 014008 (2008).

[23] O. Antunano, J. H. Kuhn, and G. V. Rodrigo,*Top Quarks, Axigluons and Charge Asymmetries at Hadron Colliders*, Phys. Rev. D **77**, 014003 (2008).

[24] M. T. Bowen, S. D. Ellis, and D. Rainwater, *Standard model top quark asymmetry at the Fermilab Tevatron*, Phys. Rev. D **73**, 014008 (2006).

[25] Johann H. Kuhn and German Rodrigo, *Charge asymmetries of top quarks at hadron colliders revisited*, arXiv:1109.6830.

[26] J. A. Aguilar-Saavedra and M. Pérez-Victoria, *Probing the Tevatron t tbar asymmetry at LHC*, JHEP **1105**, 034 (2011).

[27] J. A. Aguilar-Saavedra, M. Pérez-Victoria, *Asymmetries in t tbar production: LHC versus Tevatron*, arXiv:1107.0841.

[28] J.F. Arguin, M. Freytsis, Z. Ligeti, *Comment on measuring the t-tbar forward-backward asymmetry at ATLAS and CMS*, arXiv:1107.4090.

[29] CDF Collaboration, *Evidence for a Mass Dependent Forward-Backward Asymmetry in Top Quark Pair Production*, Phys. Rev. D **83**, 112003 (2011).

[30] D0 collaboration, *Forward-backward asymmetry in top quark-antiquark production*, Phys. Rev. D. **84**, 112005 (2011).

[31] A. Harel, A_{FB} *at the Tevatron*, slides presented at the 4^{th} International Workshop on Top Quark Physics, Sant Feliu de Guixols, Spain, September 2011.

[32] CDF Collaboration, *Measurement of the Forward Backward Asymmetry in Top Quark Pair Production in the Dilepton Decay Channel using 5.1* fb^{-1}, Conf. Note 10436.

[33] CMS Collaboration, *Measurement of the Charge Asymmetry in Top Quark Pair Production*, CMS-PAS-TOP-11-007.

[34] L. Evans and P. Bryant, *LHC Machine*, JINST **3**, S08001 (2008).

[35] ATLAS Collaboration, *The ATLAS Experiment at the CERN Large Hadron Collider*, JINST **3**, S08003 (2008).

[36] CMS Collaboration, *The CMS experiment at the CERN LHC*, JINST **3**, S08004 (2008).

[37] LHCb Collaboration, *The LHCb Detector at the LHC*, JINST **3**, S08005 (2008).

[38] ALICE Collaboration, *The ALICE experiment at the CERN LHC*, JINST **3**, S08002 (2008).

[39] https://twiki.cern.ch/twiki/bin/view/AtlasPublic/LuminosityPublicResults.

[40] ALEPH Collaboration, DELPHI Collaboration, L3 Collaboration, OPAL Collaboration and LEP Working Group for Higgs Boson Searches, *Search for the Standard Model Higgs boson at LEP*, Phys. Lett. B **565**, 61-75 (2003).

[41] CDF and D0 Collaborations, *Combined CDF and D0 Upper Limits on Standard Model Higgs Boson Production with up to 8.6* fb^{-1} *of Data*, arXiv:1107.5518v1.

[42] ATLAS Collaboration, *Search for the Standard Model Higgs boson in the two photon decay channel with the ATLAS detector at the LHC*, arXiv:1108.5895v1.

[43] ATLAS Collaboration, *Search for the Standard Model Higgs boson produced in association with a vector boson and decaying to a b-quark pair with the ATLAS detector at the LHC*, ATLAS-CONF-2011-103.

[44] ATLAS Collaboration, *Search for the Standard Model Higgs Boson in the Decay Mode $H \to \tau^+\tau^- \to ll + 4$ Neutrinos in Association with Jets in Proton-Proton Collisions at$\sqrt{s} = 7$ TeV with the ATLAS Detector*, ATLAS-CONF-2011-133.

[45] ATLAS Collaboration, *Search for the Standard Model Higgs boson in the $H \to WW(*) \to l\nu l\nu$ decay mode using 1.7 fb^{-1} of data collected with the ATLAS detector at $\sqrt{s} = 7$ TeV*, ATLAS-CONF-2011-134.

[46] ATLAS Collaboration, *Search for a heavy Standard Model Higgs boson in the channel $H \to ZZ \to llqq$ using the ATLAS detector*, arXiv:1108.5064v1.

[47] ATLAS Collaboration, *Search for the Standard Model Higgs boson in the decay channel $H \to ZZ^* \to 4l$ with the ATLAS detector*, ATLAS-CONF-2011-131.

[48] ATLAS Collaboration, *Update of the Combination of Higgs Boson Searches in 1.0 to 2.3fb^{-1} ofpp Collisions Data Taken at $\sqrt{s} = 7$ TeV with the ATLAS Experiment at the LHC*, ATLAS-CONF-2011-135.

[49] ATLAS Collaboration, *Measurement of $W\gamma$ and $Z\gamma$ production in proton-proton collisions at $\sqrt{s}$=7 TeV with the ATLAS Detector*, arXiv:1106.1592v2.

[50] ATLAS Collaboration, *Measurement of the W^+W^- production cross section in proton-proton collisions at $\sqrt{s} = 7$ with the ATLAS detector*, ATLAS-CONF-2011-110.

[51] ATLAS Collaboration, *Invariant mass distribution of jet pairs produced in association with a leptonically decaying W boson using 1.02 fb^{-1} of ATLAS data*, ATLAS-CONF-2011-097.

[52] ATLAS Collaboration, *Measurement of the WZ Production Cross-Section in Proton-Proton Collisions at $\sqrt{s} = 7$ TeV with the ATLAS Detector*, ATLAS-CONF-2011-099.

[53] ATLAS Collaboration, *Measurement of the ZZ Production Cross Section in Proton-Proton Collisions at $\sqrt{s} = 7$ TeV with the ATLAS Detector*, ATLAS-CONF-2011-107.

[54] ATLAS Collaboration, *Measurement of the transverse momentum distribution of Z/γ^* bosons in proton-proton collisions at $\sqrt{s} = 7$ TeV with the ATLAS detector*, arXiv:1107.2381v1.

[55] ATLAS Collaboration, *Measurement of the Transverse Momentum Distribution of W Bosons in pp Collisions at* $\sqrt{s} = 7$ *TeV with the ATLAS Detector*, arXiv:1108.6308v1.

[56] ATLAS Collaboration, *An extrapolation to a larger fiducial volume of the measurement of the W charge asymmetry in proton-proton collisions at* $\sqrt{s} = 7$ *TeV with the ATLAS detector: Graphical comparison between ATLAS, CMS and LHCb*, ATLAS-CONF-2011-129.

[57] Richard D. Ball, Valerio Bertone, Francesco Cerutti, Luigi Del Debbio, Stefano Forte, Alberto Guffanti, Nathan P. Hartland, Jose I. Latorre, Juan Rojo, Maria Ubiali, *Reweighting and Unweighting of Parton Distributions and the LHC W lepton asymmetry data*, arXiv:1108.1758v1.

[58] ATLAS Collaboration, *Measurement of inclusive jet and dijet cross sections in proton-proton collision data at 7 TeV centre-of-mass energy using the ATLAS detector*, ATLAS-CONF-2011-047.

[59] ATLAS Collaboration, *Measurement of the inclusive and dijet cross sections of b-jets in pp collisions at* $\sqrt{s} = 7$ *TeV with the ATLAS detector*, ATLAS-CONF-2011-056.

[60] ATLAS Collaboration, *Measurement of the b-jet production cross section using muons in jets with ATLAS in pp Collisions at* $\sqrt{s} = 7$ *TeV*, ATLAS-CONF-2011-057.

[61] ATLAS Collaboration, *Measurement of multi-jet cross sections in proton-proton collisions at a 7 TeV center-of-mass energy*, Eur. Phys. J. C **71**, 1763 (2011).

[62] ATLAS Collaboration, *Measurement of the production cross section for W-bosons in association with jets in pp collisions using 33* pb^{-1} *at* $\sqrt{s} = 7$ *TeV with the ATLAS detector*, ATLAS-CONF-2011-060.

[63] ATLAS Collaboration, *Measurement of the production cross section for* Z/γ^* *in association with jets in pp collisions at* $\sqrt{s} = 7$ *TeV with the ATLAS Detector*, ATLAS-CONF-2011-042.

[64] ATLAS Collaboration, *A measurement of the ratio of the W and Z cross sections with exactly one associated jet in pp collisions at* $\sqrt{s} = 7$ *TeV with ATLAS*, arXiv:1108.4908v1.

[65] ATLAS Collaboration, *Measurement of the cross section for the production of a W boson in association with b-jets in pp collisions at*$\sqrt{s} = 7$ *TeV with the ATLAS detector*, arXiv:1109.1470v1.

[66] ATLAS Collaboration, *Measurement of the cross-section for b-jets produced in association with a Z boson at* $\sqrt{s} = 7$ *TeV with the ATLAS detector*, arXiv:1109.1403v.

[67] ATLAS Collaboration, *Measurement of the t-channel Single Top-Quark Production Cross Section in 0.70* fb^{-1} *of pp Collisions at* $\sqrt{s} = 7$ *TeV collected with the ATLAS detector*, ATLAS-CONF-2011-101.

[68] ATLAS Collaboration, *Search for s-channel single top-quark production in pp collisions at* $\sqrt{s} = 7$ *TeV*, ATLAS-CONF-2011-118.

[69] ATLAS Collaboration, *Search for Wt associated production in dilepton final states with 0.70* fb^{-1} *of* $\sqrt{s} = 7$ *TeV pp collision data in ATLAS*, ATLAS-CONF-2011-104.

[70] ATLAS Collaboration, *Measurement of the Top-Quark Mass from 2011 ATLAS Data using the Template Method*, ATLAS-CONF-2011-120.

[71] ATLAS Collaboration, *Measurement of the W boson polarisation in top quark decays in 0.70* fb^{-1} *of pp collisions at sqrts* $= 7$ *TeV with the ATLAS detector*, ATLAS-CONF-2011-122.

[72] ATLAS Collaboration, *A search for Flavour Changing Neutral Currents in Top Quark Decays* $t \to qZ$ *at* $\sqrt{s} = 7$ *TeV in 0.70* fb^{-1} *of pp collision data collected with the ATLAS Detector*, ATLAS-CONF-2011-154.

[73] ATLAS Collaboration, *Search for FCNC top quark processes at 7 TeV with the ATLAS detector*, ATLAS-CONF-2011-061.

[74] ATLAS Collaboration, *Measurement of spin correlation in* $t\bar{t}$ *production from pp collisions at* $\sqrt{s} = 7$ *TeV using the ATLAS detector*, ATLAS-CONF-2011-117.

[75] ATLAS Collaboration, *Measurement of the top quark charge in pp collisions at* $\sqrt{s} = 7$ *TeV in the ATLAS experiment*, ATLAS-CONF-2011-141.

[76] ATLAS Collaboration, *Search for squarks and gluinos using final states with jets and missing transverse momentum with the ATLAS detector in* $\sqrt{s} = 7$ *TeV proton-proton collisions*, ATLAS-CONF-2011-086.

[77] ATLAS Collaboration, *Search for supersymmetry with jets, missing transverse momentum and one lepton at* $\sqrt{s} = 7$ *TeV*, ATLAS-CONF-2011-090.

[78] ATLAS Collaboration, *Search for supersymmetric particles in events with lepton pairs and large missing transverse momentum in* $\sqrt{s} = 7$ *TeV proton-proton collisions with the ATLAS experiment*, Eur. Phys. J. C **71**, 1682, (2011).

[79] ATLAS Collaboration, *Search for supersymmetry in pp collisions at* $\sqrt{s} = 7$ *TeV in final states with missing transverse momentum, b-jets and no leptons with the ATLAS detector*, ATLAS-CONF-2011-098.

[80] ATLAS Collaboration, *Search for supersymmetry in pp 1 collisions at* $\sqrt{s} = 7$ *TeV in final states with missing transverse momentum, b-jets and one lepton with the ATLAS detector*, ATLAS-CONF-2011-130.

[81] ATLAS Collaboration, *Observation of a centrality-dependent dijet asymmetry in lead-lead collisions at psNN = 2.76 TeV with the ATLAS detector at the LHC*, Phys. Rev. Lett. **105**, 252303 (2010).

[82] https://twiki.cern.ch/twiki/bin/view/AtlasPublic/InDetTrackingPerformance ApprovedPlots#Figures.

[83] T. Cornelissen, M. Elsing, I. Gavrilenko, W. Liebig, E. Moyse and A. Salzburger, *The New Atlas Track Reconstruction (Newt)*, J. Phys. Conf. Ser. **119**, 032014 (2008).

[84] ATLAS Collaboration, *Readiness of the ATLAS Liquid Argon Calorimeter for LHC Collisions*, Eur. Phys. J. C **70**, 723-753 (2010).

[85] ATLAS Collaboration, *Readiness of the ATLAS Tile Calorimeter for LHC collisions*, Eur. Phys. J. C **70**, 1193-1236 (2010).

[86] ATLAS Collaboration, *Commissioning of the ATLAS Muon Spectrometer with Cosmic Rays*, Eur. Phys. J. C **70**, 875-916 (2010).

[87] ATLAS Collaboration, *Luminosity Determination Using the ATLAS Detector*, ATLAS-CONF-2010-060.

[88] A. Sbrizzi, *A Cherenkov Detector for Monitoring ATLAS Luminosity*, ATL-LUM-PROC-2010-004.

[89] P. Ruzicka, *Forward physics at the ATLAS experiment*, ATL-LUM-PROC-2010-001.

[90] ATLAS Collaboration, *The Trigger for Early Running, ch. in Expected performance of the ATLAS experiment: detector, trigger and physics*, pp. 550-564, CERN-OPEN-2008-020.

[91] W. Lampl et al., *Calorimeter Clustering Algorithms: Description and Performance*, ATL-LARG-PUB-2008-002.

[92] ATLAS Collaboration, *Electron and photon reconstruction and identification in ATLAS: expected performance at high energy and results at 900 GeV*, ATLAS-CONF-2010-005.

[93] D. Banfi, L. Carminati, L. Mandelli, *Calibration of the ATLAS electromagnetic calorimeter using calibration hits*, ATL-LARG-PUB-2007-012.

[94] https://atlas.web.cern.ch/Atlas/GROUPS/PHYSICS/EGAMMA/PublicPlots/20110303/CalibratedJPsi/ATL-COM-PHYS-2011-160/ATL-COM-PHYS-2011-160.pdf.

[95] ATLAS Collaboration, *A measurement of the total $W^{\pm}$ and Z/γ^{*} cross sections in the e and μ decay channels and of their ratios in pp collisions at $\sqrt(s)$ = 7 TeV with the ATLAS detector*, ATLAS-CONF-2011-041.

[96] S. Hassani, L. Chevalier, E. Lancon, J. F. Laporte, R. Nicolaidou and A. Ouraou, *A muon identification and combined reconstruction procedure for the ATLAS detector at the LHC using the (MUONBOY, STACO, MuTag) reconstruction packages*, Nucl. Instrum. Meth. A **572**, 77 (2007).

[97] T. Lagouri et al., *A muon identification and combined reconstruction procedure for the ATLAS detector at the LHC at CERN*, IEEE Trans. Nucl. Sci. **51**, 3030-3033 (2004).

[98] ATLAS Collaboration, *Muon Performance in Minimum Bias pp Collision Data at vs = 7 TeV with ATLAS*, ATLAS-CONF-2010-036.

[99] https://twiki.cern.ch/twiki/bin/view/Atlas/MuonPerformancePublicPlots.

[100] M. Cacciari, G. P. Salam and G. Soyez, *The anti-kt jet clustering algorithm*, JHEP **0804**, 063 (2008).

[101] G.P. Salam, *Towards Jetography*, arXiv-0906.1833v1.

[102] ATLAS Collaboration, *Calibrating the b-Tag Efficiency and Mistag Rate in 35 pb^{-1} of Data with the ATLAS Detector*, ATLAS-CONF-2011-089.

[103] ATLAS Collaboration, *Performance of the Missing Transverse Energy Reconstruction and Calibration in Proton-Proton Collisions at a Center-of-Mass Energy of 7 TeV with the ATLAS Detector*, ATLAS-CONF-2010-057.

[104] ATLAS Collaboration, *Performance of the missing transverse energy reconstruction in minimum bias events at $\sqrt{s}$ of 900 GeV and 2.36 TeV with the ATLAS detector*, ATLAS-CONF-2010-008.

[105] ATLAS Collaboration, *Performance of the missing transverse energy reconstruction in proton-proton collisions at center-of-mass energy of $\sqrt{s}$ = 7 TeV with the ATLAS detector*, ATLAS-CONF-2010-039.

[106] ATLAS Collaboration, *Reconstruction and Calibration of Missing Transverse Energy and Performance in Z and W events in ATLAS Proton-Proton Collisions at $\sqrt{s}$=7 TeV*, ATLAS-CONF-2011-080.

[107] ATLAS Collaboration *ATLAS computing: Technical Design Report*, CERN-LHCC-2005-022.

[108] *ROOT*, http://root.cern.ch/.

[109] https://twiki.cern.ch/twiki/bin/view/AtlasPublic/RunStatsPublicResults2010.

[110] ATLAS Collaboration, *Prospects for the top pair pair production cross-section at $\sqrt{s}$=10 TeV in the single lepton channel in ATLAS*, ATL-PHYS-PUB-2009-087.

[111] Acharya B. et al. (Besana M.I.), *Prospects for measuring the Top Quark Pair Production Cross-section in the Single Lepton Channel at ATLAS in 10 TeV p-p Collisions*, ATL-PHYS-INT-2009-071.

[112] ATLAS Collaboration, *Measurement of the top quark-pair production cross section with ATLAS in pp collisions at $\sqrt{s}$ =7 TeV*, Eur. Phys. J. C **71**, 1577 (2011).

[113] ATLAS Collaboration, *Top Quark Pair Production Cross-section Measurements in ATLAS in the Single Lepton+Jets Channel without b-tagging*, ATLAS-COM-CONF-2011-031.

[114] ATLAS Collaboration, *Measurement of the top quark-pair cross-section with ATLAS in pp collisions at sqrt(s) = 7 TeV in the single-lepton channel using b-tagging*, ATLAS-COM-CONF-2011-028.

[115] Acharya, B et al.(Besana, M I), *Cut-and-count measurement of the top quark pair production in the semileptonic decay channel at sqrt(s)=7 TeV with the ATLAS detector*, ATL-PHYS-INT-2011-048.

[116] ATLAS Collaboration, *Measurement of the top quark pair production cross section in pp collisions at $\sqrt{s}$ = 7 TeV in $\mu + \tau$ final states with ATLAS*, ATLAS-CONF-2011-119.

[117] J. Campbell et al., *Hard interactions of quarks and gluons: a primer for LHC physics*, arXiv:hep-ph/0611148.

[118] Besana M.I., *Study of W+jets background to top quark pair production cross section in ATLAS at the LHC*, published in *Second Young Researchers Workshop "Physics Challenges in the LHC Era"*, Frascati Physics Series Volume LI, Ed. E. Nardi Frascati, ISBN 978-88-86409-60-5.

[119] S. Agostinelli et al., *Geant4 – a simulation toolkit*, Nucl. Instr Meth. A **506**, 250 (2003);
J. Allison et al., *Geant4 developments and applications*, IEEE Transactions on Nuclear Science **53(1)**, 270–278 (2006).

[120] ATLAS Collaboration, *The ATLAS Simulation Infrastructure*, arXiv:1005.4568.

[121] S. Frixione and B.R. Webber, *Matching NLO QCD computations and parton shower simulations*, JHEP **0206**, 029 (2002);
S. Frixione, P. Nason and B.R. Webber, *Matching NLO QCD and parton showers in heavy flavour production*, JHEP **0308**, 007 (2003);
S. Frixione, E. Laenen and P. Motylinski, *Single-top production in MC@NLO*, JHEP **0603**, 092 (2006).

[122] P.M. Nadolsky et al., *Implications of CTEQ global analysis for collider observables*, Phys. Rev. D **78**, 013004 (2008).

[123] M. Aliev, H. Lacker, U. Langenfeld, S. Moch, and P. Uwer, *HATHOR*, http://www.physik.hu-berlin.de/pep/tools.

[124] S. Frixione, E. Laenen, P. Motylinski, B.R. Webber and C.D. White, *Single-top hadroproduction in association with a W boson*, JHEP **0807**, 029 (2008).

[125] M. L. Mangano, M. Moretti, F. Piccinini, R. Pittau and A.D. Polosa, *ALPGEN, a generator for hard multiparton processes in hadronic collisions*, JHEP **0307**, 001 (2003).

[126] J. Pumplin et al., *New generation of parton distributions with uncertainties from global QCD analysis*, JHEP **0207**, 012 (2002).

[127] G. Corcella et al., *HERWIG 6.5: an event generator for Hadron Emission Reactions With Interfering Gluons (including supersymmetric processes)*, JHEP **0101**, 010 (2001);
G. Corcella et al., *HERWIG 6.5 release notes*, arXiv:hep-ph/0210213.

[128] J.M. Butterworth et al., *Multiparton interactions in photoproduction at HERA*, Z. Phys. C **72**, 637 (1996).

[129] J. M. Campbell and R. K. Ellis, *An update on vector boson pair production at hadron colliders*, Phys. Rev. D **60**, 113006 (1999).

[130] P. Nason, *A new method for combining NLO QCD with shower Monte Carlo algorithms*, JHEP **11546**, 040 (2004).

[131] B. P. Kersevan and E. Richter-Was, *The Monte Carlo event generator AcerMC version 2.0 with561 interfaces to PYTHIA 6.2 and HERWIG 6.5*, arXiv:hep-ph/0405247.

[132] ATLAS Collaboration, *Top Quark Physics, ch. in Expected Performance of the ATLAS Experiment: Detector, Trigger and Physics*, pp 874–878, CERN-OPEN-2008-020.

[133] T. Gleisberg et al., *Event generation with SHERPA 1.1*, JHEP **0902**, 007 (2009).

[134] ATLAS Collaboration, *Meausurement of inclusive jet and dijet cross-sections in proton-proton collisions at 7 TeV centre-of-mass energy with the ATLAS detector*, Eur. Phys. J. C **71**, 1 (2011).

[135] ATLAS Collaboration, *Performance of the ATLAS Secondary Vertex b-tagging Algorithm in 7 TeV Collision Data*, ATLAS-CONF-2010-042.

[136] C. Amelung et al., *Muon Momentum Resolution in First Pass Reconstruction of pp Collision Data Recorded by ATLAS in 2010*, ATLAS-COM-CONF-2011-003.

[137] F. A. Berends, W. T. Giele, H. Kuijf, R. Kleiss, W. J. Stirling, Nucl. Phys. B **357**, 1 (1991).

[138] S.D. Ellis, R. Kleiss, W. J. Stirling, Phys. Lett. B **154**, 435 (1985).

[139] B. Alvarez et al., *b-jet tagging for top physics: performance studies, calibrations and heavy flavour fractions*, ATL-COM-PHYS-2011-124.

[140] D0 collaboration, *Extraction of the width of the W boson from measurements of* $\sigma(p\bar{p} \to W + X) \cdot BR(W \to e\nu)$ *and* $\sigma(p\bar{p} \to Z + X) \cdot BR(Z \to ee)$ *and their ratio*, Phys. Rev. D **61**, 072001 (2000).

[141] ATLAS Collaboration,*Measurement of the charge asymmetry in top quark pair production in pp collisions at* $\sqrt{s}$ *= 7 TeV using the ATLAS detector*, ATLAS-CONF-2011-106.

[142] Acharya B. et al. (Besana M.I.), *Measurement of the top quark charge asymmetry in pp collision data at* $\sqrt{s}$ *= 7 TeV using the ATLAS detector*, ATL-PHYS-INT-2011-063.

[143] Besana M.I., *Measurement of top quark charge asymmetry at the LHC using the ATLAS detector*, ATL-PHYS-PROC-2011-275.

[144] ATLAS Collaboration, *Luminosity Determination in pp Collisions at* $\sqrt{s} = 7$ *TeV using the ATLAS Detector in 2011*, ATLAS-CONF-2011-116.

[145] B. Butler and A. Schwartzman, *Track-Jet Reconstruction and Performance*, ATL-PHYS-INT-2010-040.

[146] ATLAS Collaboration, *Jet energy resolution and reconstruction efficiencies from in-situ techniques with the ATLAS Detector Using Proton-Proton Collisions at a Center of Mass Energy* $\sqrt{s} = 7$ *TeV*, ATLAS-CONF-2010-054.

[147] G. Romeo, A. Schwartzman, R. Piegaia, T. Carli, and R. Teuscher, *Jet Energy Resolution from In-situ Techniques with the ATLAS Detector Using Proton-Proton Collisions at a Center of Mass Energy* $\sqrt{s} = 7$ *TeV*, ATL-COM-PHYS-2011-240.

[148] ATLAS Collaboration, *Jet energy scale and its systematic uncertainty in proton-proton collisions at* $\sqrt{s} = 7$ *TeV in ATLAS 2010 data*, ATLAS-CONF-2011-032.

[149] C. H. Kom and W. J. Stirling, *Charge asymmetry in W + jets production at the LHC*, Eur. Phys. J. C **69**, 67 (2010).

[150] A.D. Martin, W.J. Stirling, R.S. Thorne and G. Watt, *Uncertainties on* α_S *in global PDF analysis*, arXiv:0905.3531.

[151] NNPDF Collaboration: R. Ball, L. Del Debbio, A. Guffanti, S. Forte, J.I. Latorre, J. Rojo and M. Ubiali, *NNPDF fit*, arXiv:1002.4407.

[152] Webber, http://www.hep.phy.cam.ac.uk/theory/webber/MCEGforLHC.pdf.

[153] G. D'Agostini, *Improved iterative Bayesian unfolding*, arXiv:1010.0632v1.

[154] T. Adye, *Unfolding algorithms and tests using RooUnfold*, arXiv:1105.1160v1.

[155] L. Lyons, D. Gibaut, and P. Clifford, *How to combine correlated estimates of a single physical quantity*, Nucl. Instrum. Meth. A **270**, 110 (1988).

[156] A. Valassi, *Combining correlated measurements of several different physical quantities*, Nucl. Instrum. Meth. A **500**, 391-405 (2003).

[157] J. A. Aguilar-Saavedra, A. Juste, F. Rubbo, *Boosting the t tbar charge asymmetry*, arXiv:1109.3710v2.